Exploiting aperiodic designs in nanophotonic devices

2012 Rep. Prog. Phys. 75 036502

(http://iopscience.iop.org/0034-4885/75/3/036502)

Rep. Prog. Phys. **75** (2012) 036502 (42pp) doi:10.1088/0034-4885/75/3/036502

Exploiting aperiodic designs in nanophotonic devices

Enrique Maciá

Departamento Física de Materiales, Facultad CC. Físicas, Universidad Complutense de Madrid, 28040, Madrid, Spain

E-mail: emaciaba@fis.ucm.es

Received 11 January 2011, in final form 26 September 2011
Published 15 February 2012
Online at stacks.iop.org/RoPP/75/036502

Abstract

In this work we consider the role of aperiodic order—order without periodicity—in the design of different optical devices in one, two and three dimensions. To this end, we will first study devices based on aperiodic multilayered structures. In many instances the recourse to Fibonacci, Thue–Morse or fractal arrangements of layers results in improved optical properties compared with their periodic counterparts. On this basis, the possibility of constructing optical devices based on a modular design of the multilayered structure, where periodic and quasiperiodic subunits are properly mixed, is analyzed, illustrating how this additional degree of freedom enhances the optical performance in some specific applications. This line of thought can be naturally extended to aperiodic arrangements of optical elements, such as nanospheres or dielectric rods in the plane, as well as to three-dimensional photonic quasicrystals based on polymer materials. In this way, plentiful possibilities for new tailored materials naturally appear, generally following suitable optimization algorithms. Then, we present a detailed discussion on the physical properties supporting the preferential use of aperiodic devices in a number of optical applications, opening new avenues for technological innovation. Finally we suggest some related emerging topics that deserve some attention in the years to come.

(Some figures may appear in colour only in the online journal)

Contents

1. Introduction 2
1.1. The rise of aperiodic thinking 2
1.2. Scalability in fractal multilayers 3
1.3. Quasiperiodicity blueprints 4
1.4. Critical nature of light waves 6
1.5. Why choose the aperiodic one? 6
1.6. Aperiodicity by design 7
2. Layered optical systems 8
2.1. Aperiodic dielectric multilayers 8
2.2. Hybrid order multilayers 13
2.3. Some potential applications 16
3. Optical devices in two dimensions 23
3.1. Inflation rules in two dimensions 24
3.2. Aperiodic tilings 26
3.3. Photonic quasicrystals in two dimensions 27
3.4. Optimized structures 31
4. Three-dimensional arrangements 32
4.1. Axial photonic quasicrystals 33
4.2. Icosahedral photonic quasicrystals 33
4.3. Spherical and cylindrical geometries 34
5. Conclusions 35
5.1. Aperiodicity versus periodicity 35
5.2. Outlook and perspectives 39
Acknowledgments 40
References 40

1. Introduction

1.1. The rise of aperiodic thinking

During the last decade we have come to realize that *ordered matter* domains can be suitably expanded to embrace not only periodic arrangements but aperiodic ones as well [1–11]. In this way, the very notion of aperiodic order, that is, *order without periodicity*, has been used to properly describe a growing number of physical systems, including quasiperiodic crystal (QC) alloys [12–15], semiconductor heterostructures, metallic and dielectric multilayers, or both synthetic and biological DNA macromolecules [16]. The gradual awakening of aperiodic thinking in condensed matter and materials science communities alike has naturally given rise to a novel approach in the quest for more efficient optical devices, focusing on the *design* of *aperiodic structures* able to achieve a better performance than periodic ones for certain specific optical applications. In doing so, well-known materials still remain in use, along with previously gained technological expertise, as attention is entirely devoted to the (relatively low-cost) aspects related to optimal device design [17].

Aperiodic arrangements of matter exhibit long-range order in space, just as periodic orderings do. This property clearly distinguishes aperiodic structures from amorphous matter, the latter displaying short-range correlations only. Accordingly, aperiodic order has nothing to do with disorder in any of its possible multiple forms, since aperiodic systems neatly feature order beyond mere periodicity. For the sake of illustration, let us consider a structure consisting of a large number of layers stacked according to a certain *deterministic rule*, usually specified in terms of the so-called *substitution sequences*. A substitution sequence is formally defined by its action on an alphabet $\mathcal{A} = \{A, B, C...\}$, which consists of a certain number of letters. In actual system, each letter will correspond to a different type of building block in the heterostructure. The substitution rule starts by replacing each letter by a finite word. The corresponding aperiodic sequence is then obtained by iterating the substitution rule starting from a given letter of the set $\mathcal{A}$ in order to obtain an aperiodic string of letters. A simple example of such a nanostructured material is a two-component Fibonacci multilayer, where layers of two different materials (metallic, semiconductor, dielectric, ferroelectric) are arranged according to the celebrated Fibonacci substitution rule $A \to AB$ and $B \to A$, the successive application of which generates the sequence of letters $A \to AB \to ABA \to ABAAB \to ABAABABA \to ABAABABAABAAB \to$ ... and so on (figure 1(*a*)) [18]. The number of letters in a sequence of order n is given by the *Fibonacci number* F_j, which is obtained from the recurrence relation $F_j = F_{j-1} + F_{j-2}$, $j \geqslant 2$, with $F_1 = F_0 \equiv 1$. A key feature of these man-made materials is the presence of *two kinds of order* in the same sample *at different length scales*: at the atomic level we have the usual crystalline order determined by the periodic arrangement of atoms in each layer, whereas at longer scales we have the aperiodic order determined by the sequential deposition of the different layers. This long-range aperiodic order is imposed during the growth process and can be precisely controlled. Since

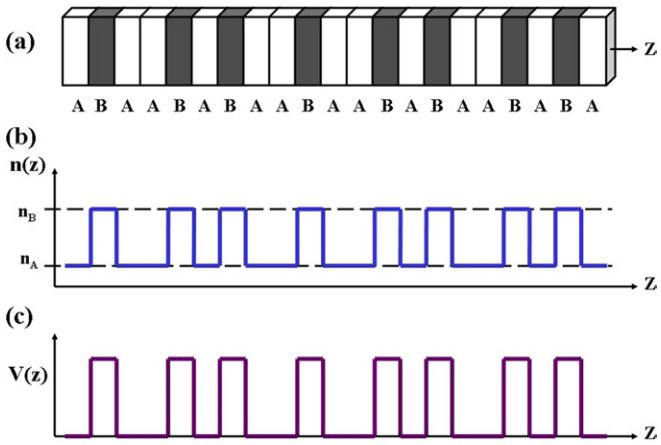

Figure 1. (*a*) Sketch of a Fibonacci dielectric multilayer grown along the z direction, (*b*) refractive index profile $n(z)$ for an electromagnetic wave propagating through the structure, (*c*) electronic potential profile $V(z)$ for an electron propagation along the growth direction.

different physical phenomena have their own relevant physical scales, by properly matching the characteristic length scales we can efficiently exploit the aperiodic order we have introduced in the system, hence opening new avenues for technological innovation [7].

Aperiodic systems can be classified according to different criteria. In this work we will split them into two broad categories, namely *self-similar* and non-self-similar ones. All systems based on aperiodic sequences derived from the application of a substitution rule belong to the self-similar class. Within this class we can further distinguish between those structures exhibiting long-range *quasiperiodic* order (like Fibonacci) and those which do not (like fractal Cantor sets). With the exception of the Fibonacci sequence (which can be found profusely in botanical arrangements or morphogenetic patterns) [7, 19], most earlier aperiodic designs, namely Thue–Morse, Rudin–Shapiro, or period-doubling sequences, on the one hand, and Penrose, Stampfli or Ammann–Beenker tiles, on the other hand, were originally introduced following mathematical motivations.

One of the most appealing motivations for the experimental study of these systems was the theoretical prediction that they should exhibit peculiar quantum states, associated with highly fragmented energy spectra displaying fractal self-similar patterns [1–4]. However, a number of severe limitations appeared in realistic setups due to structural imperfections [20], along with electron–phonon, electron–electron or spin–orbit interaction effects, which make it a very difficult task to efficiently exploit spectrum fractal features in actual electronic applications [21–23]. Quite interestingly, multiple scattering and interference of scattered waves can be found in classical as well as quantum physical processes. Therefore, in order to fully appreciate the fingerprints of long-range aperiodic order, the study of classical waves propagating through an aperiodic substrate offers a number of advantages over the study of quantum elementary excitations.

Consequently, light transmission through aperiodic media has deserved an ever increasing attention in order to understand

the interplay between optical properties and the underlying aperiodic order of the substrate. To this end, the mathematical analogy between Schrödinger's equation describing the motion of an electron with a wave function ψ, energy ε and effective mass m, under the action of a potential $V(z)$ in one dimension

$$\frac{\hbar^2}{2m}\frac{\mathrm{d}^2\psi}{\mathrm{d}z^2} + [\varepsilon - V(z)]\psi = 0, \tag{1}$$

and Helmholtz's equation describing a monochromatic electromagnetic wave of frequency ω propagating in a lossless, dispersionless medium with a variable refractive index profile $n(z)$

$$\frac{\mathrm{d}^2E}{\mathrm{d}z^2} + \left[\frac{\omega^2}{c^2}n^2(z) - k_\parallel^2\right]E = 0, \tag{2}$$

where E is the transversal component of the electric field, $k_\parallel$ is the wave vector in the XY plane (perpendicular to the propagation direction z), and c is the vacuum speed of light, provides a powerful tool to relate previous knowledge about electron motion in superlattices to electromagnetic waves propagating in multilayers (figure 1). We note that the refractive index of the different layers is the physical magnitude relating the aperiodic sequence describing the stacking order along the multilayer (figure 1(*a*)) and the resulting *aperiodic function* describing the multilayer's optical profile (figure 1(*b*)). Thus, the isomorphism of the Schrödinger and Helmholtz equations provides a helpful analogy involving basic concepts in modern optoelectronics [10].

In the case of periodic media, a general description, which borrows some basic notions like Bloch waves or Brillouin zones from condensed matter theory, has been developed and successfully applied to numerous optical devices, which are of common use nowadays in optoelectronics and optical communication applications. In this way, the so-called *photonic crystal* concept has been introduced to describe optical systems which exhibit large frequency stop bands due to interference effects, in close analogy with the presence of band structure in conventional atomic lattices, or the formation of energy minibands in superlattices [24–26]. Naturally, the very notion of photonic crystal can be extended to describe the properties of aperiodic photonic structures as well. To this end, one simply considers that the optical properties of the medium are given by a quasiperiodic refraction index function, $n(z)$, instead of a periodic one in (2). The resulting structure can be properly regarded as a one-dimensional (1D) *photonic quasicrystal* (PQC). Similarly, one could construct a *photonic fractal* by arranging the structure according to a certain self-similar refraction index profile [27]. As we will see in section 2.1.3, for any aperiodic function $n(z)$ in (2), a number of resonant modes exist describing the propagation of waves throughout the structure without reflection. These modes naturally appear as high transmission peaks (deeps) in their related transmittance (reflectance) spectra. In this way, by considering different kinds of refraction index profiles (i.e. periodic, quasiperiodic, self-similar, random) a characteristic spectral signature could be assigned to every structure.

In the following sections we will address the relationship between the aperiodic order present in the underlying substrate and their related optical properties by considering the following basic questions:

- Are there any fundamental differences in the optical properties among different classes of aperiodically arranged systems?
- Can the main novel optical features of aperiodic systems be experimentally observed?
- What can be said about possible technological applications of aperiodic nanophotonic devices?

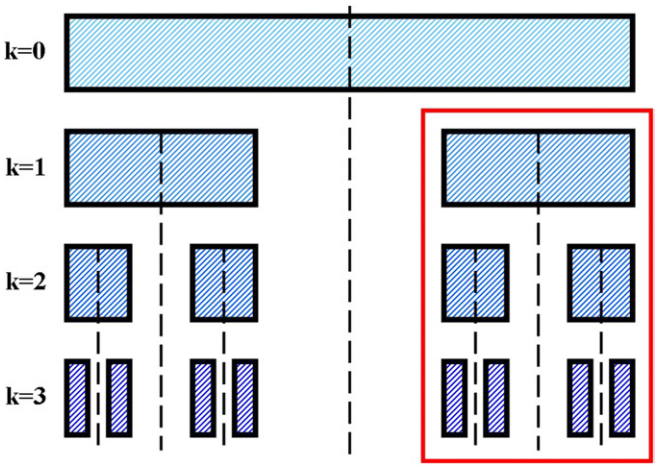

Figure 2. Successive stages defining the generation of a triadic Cantor set. A characteristic property of this set is its self-similarity, which is illustrated in the box. We note that the resulting segments and gaps are mutually commensurate by construction. In addition, due to the inflation symmetry characteristic of a Cantor set, the mirror symmetry axis present in the starting segment splits into a progressive series of local mirror symmetry axes whose number geometrically increase with the generation number k as 2^k.

1.2. Scalability in fractal multilayers

In general a Cantor set is defined as what is left from a finite segment after removing parts of it according to some iterative procedure. For instance, one may consider the triadic Cantor set, which is obtained through the repetition of a simple rule: divide any given segment into three equal parts, then eliminate the central one, and continue this process (figure 2). Although this is a usual way of obtaining a Cantor set, it is by no means the only one. More general Cantor sets can be generated by iterating the operation consisting of the division of a segment into $s = 2r - 1$ equal parts ($r \geqslant 2$) and the removal of $r - 1$ of its pieces. The value s is generally referred to as the generator number of the Cantor set. The resulting structures are self-similar and have a fractal dimension $D = \ln r / \ln s$. We note that Cantor sets can either exhibit mirror symmetry or not (figure 2). A Cantor structure can also be obtained by successively applying the substitution rule $A \rightarrow ABA...BA$ (containing r A's) and $B \rightarrow BBB...B$ (containing s B's). Thus, the triadic Cantor set is obtained from the inflation process $A \rightarrow ABA$ and $B \rightarrow BBB$. Making use of this procedure, different kinds of Cantor heterostructures have been grown by alternatively depositing two different materials

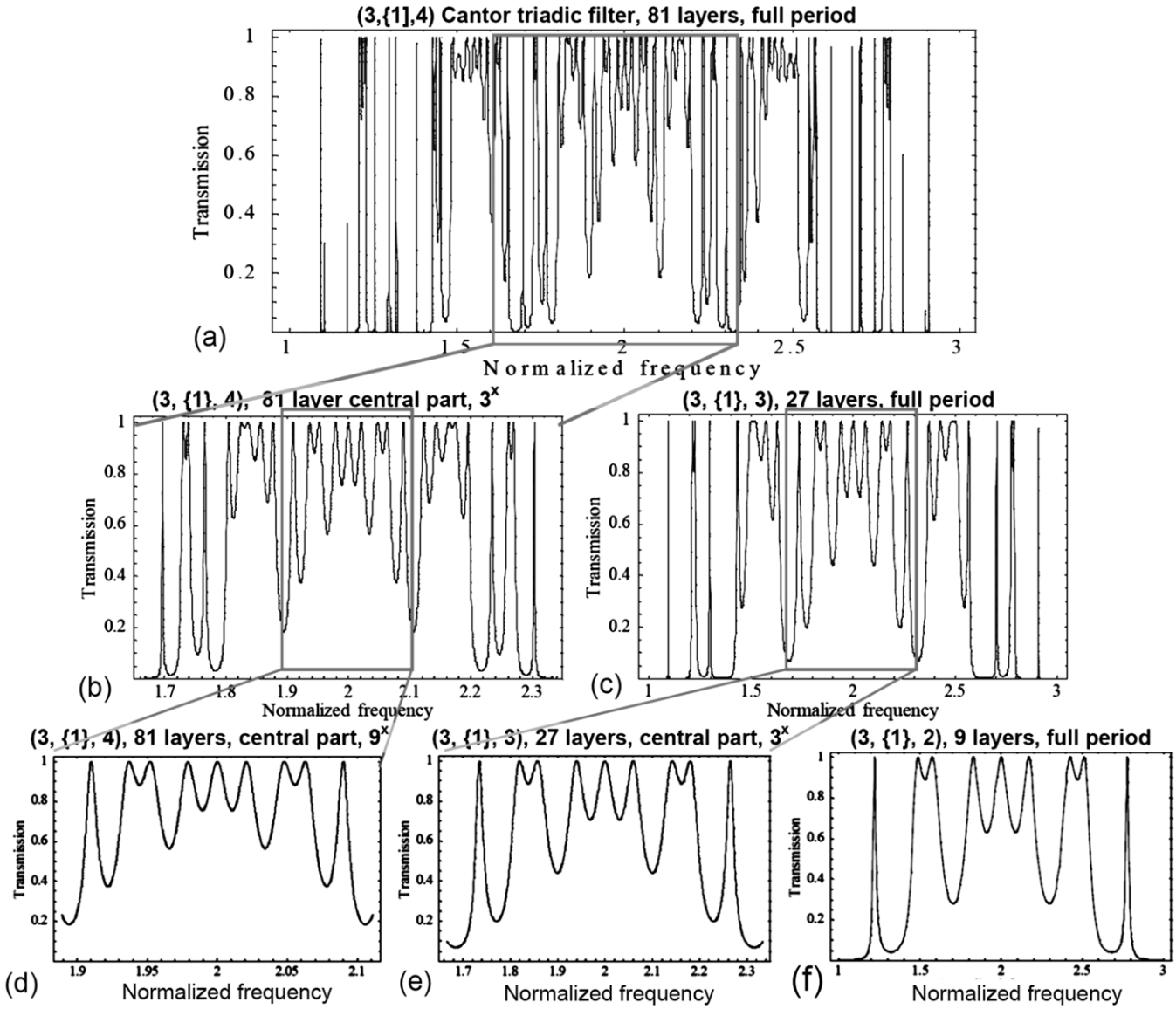

Figure 3. Scalability of optical spectra for triadic Cantor multilayers. (*a*) the full period for $n = 4$, (*b*) its central part magnified in the frequency scale by $s = 3$, (*c*) the full period for $n = 3$, (*d*) the central part for $n = 4$ magnified by $s^2 = 9$, (*e*) the central part for $n = 3$ magnified by $s = 3$, and (*f*) the full period for $n = 2$. Reprinted with permission from [10], Cambridge University Press. (Courtesy of Sergey Gaponenko.)

[28, 29]. The obtained structures can be regarded as finite order approximants of the mathematical Cantor sets.

The self-similarity of the underlying structure manifests itself in the transmittance spectra of aperiodic multilayers based on both Fibonacci and Cantor sequences, though it can be more clearly appreciated in the Cantor ones, since they lack the additional complexities related to the long-range quasiperiodic order present in Fibonacci's. Thus, it has been shown that for every type of fractal structure, the transmission spectrum of any given generation $k > 2$ contains embedded transmission spectra of all preceding generations $j = 1, 2, ...k - 1$, the spectrum of every preceding generation being squeezed along the frequency axis by a scale factor s^{k-j} [10, 30–32]. This characteristic property is illustrated in figure 3. We note that whereas the scalability factor takes on integer values in the case of Cantor fractal structures, we have irrational scale factor values in the case of quasiperiodic structures. Accordingly, self-similarity features can be more easily observed in the transmittance of Cantor multilayers. The progressive fragmentation of the frequency spectrum as n increases gives rise to narrower transmission bands, which in turn result from preferential localization of light-wave energy in certain resonant cavities present in the structure. In fact, one easily realizes that the triadic Cantor second generation structure can be regarded as a BBB cavity embedded by a pair of ABA mirrors. For higher generations, the number of existing cavities grows by a factor of r and the related transmission peaks split accordingly.

1.3. Quasiperiodicity blueprints

From a structural viewpoint, quasiperiodic and fractal systems belong to two different classes. In fact, quasiperiodic structures are composed of building blocks exhibiting two

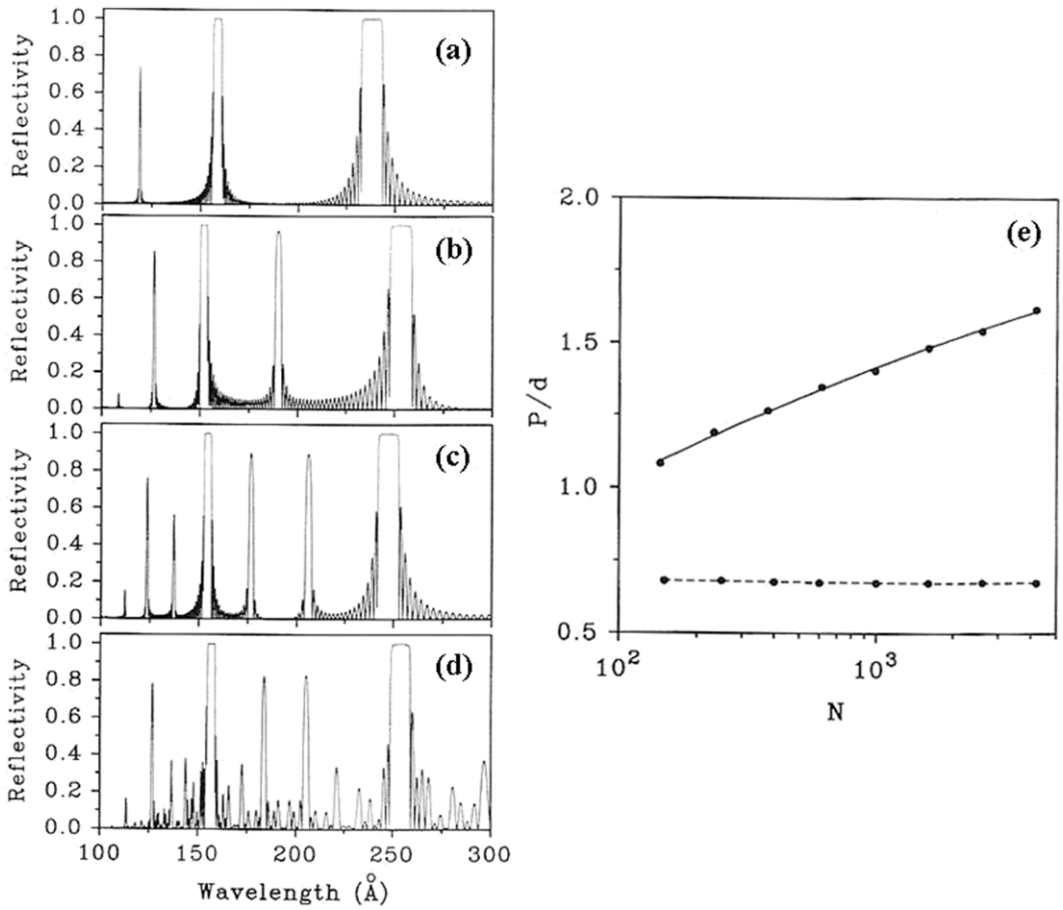

Figure 4. Numerically calculated x-ray reflectivity of multilayer structures with refractive indices $n_A = 0.9200$ and $n_B = 0.9995$, each layer thickness being $d = 5$ nm. Results for periodic approximants of the form (*a*) $(ABAAB)^m$ with $m = 47$ ($N = 235$), (*b*) $(ABAABABA)^m$ with $m = 29$ ($N = 232$), (*c*) $(ABAABABAABAAB)^m$ with $m = 18$ ($N = 234$), and (*d*) a Fibonacci multilayer with $N = F_{12} = 233$ are shown. (*e*) Overall reflectivity (in units of the layer thickness d) as a function of the number of layers N in periodic (dashed line) and Fibonacci approximant multilayers of similar size (solid line) as the number of layers progressively grows from $N = 144$ up to $N = 4181$. (Adapted from [33].)

(or more) incommensurate length scales, while the sizes of fractal lattices building blocks are mutually commensurate. Thus, in addition to the self-similarity related scale-invariance symmetry, which is shared by both of them, quasiperiodic structures are characterized by the presence of long-range quasiperiodic order as well. Accordingly, aperiodic multilayers arranged according to a quasiperiodic sequence can be properly regarded as 1D QCs [8, 9]. Nevertheless, specific properties typically related to long-range quasiperiodic order require a *threshold size* to properly manifest themselves. For instance, only in the limit $N \to \infty$ (where N is the number of layers) it can be properly said that the highly fragmented transmission spectrum of a Fibonacci multilayer consists of a self-similar Cantor set with zero Lebesgue measure. Now, actual devices are always finite in length whereas the mathematically derived results deal with ideal, arbitrarily long systems. Thus, in practical applications one must reach a balance between the unavoidable presence of energy losses and dispersion effects (demanding relatively small systems) and beneficial aspects stemming from self-similarity and quasiperiodicity related effects (requiring large enough systems). Therefore, to experimentally check most theoretical results one must follow a *systematic study* looking for the possible presence (or not) of certain physical trends as the size of the considered system is progressively increased. To this end, the recourse to aperiodic structures generated from the application of substitution rules or iterative tilings is very useful, since each successive term in the growing series provides the so-called kth order *unit-cell approximant* to the asymptotic, full-fledged quasiperiodic system. For the sake of illustration, in figure 4 we show the x-ray reflectivity spectra for a series of *periodic approximants* of the Fibonacci multilayer, which are obtained by assembling together m copies of a given nth order approximant. In all cases, two main reflection peaks are observed at about $\lambda = 150$ Å and $\lambda = 250$ Å, along with a set of subsidiary peaks whose number increases as the order of the approximant increases. These peaks appear at certain wavelengths whose values can be described in terms of regular splitting schemes, displaying a *hierarchical* reflectivity spectrum. Thus, all peaks can be properly labeled according to the multilayer generation order at which they first appeared, since every peak remains at very similar locations in the spectra of the subsequent multilayer periodic approximants. This hierarchical structure clearly manifests the quasiperiodic order of the underlying structure. On the other hand, the ever increasing number of peaks

with the generation order n guarantees one can obtain better reflectivity properties (as compared with those corresponding to the periodic counterparts) by considering relatively low order generations. In terms of the reflectivity spectrum, $R_N(\lambda)$, this property can be quantified by means of the expression

$$P_N = \frac{\left[\int_{\lambda_{\min}}^{\lambda_{\max}} R_N(\lambda)\,\mathrm{d}\lambda\right]^2}{\int_{\lambda_{\min}}^{\lambda_{\max}} R_N^2(\lambda)\,\mathrm{d}\lambda}, \qquad (3)$$

which gives an estimation of the overall reflectivity of the sample as a function of the number of layers for a given spectral window $[\lambda_{\min}, \lambda_{\max}]$. The overall contribution due to different reflectivity peaks can be characterized by the scaling of P_N with the number of layers, the higher its value the higher the whole reflectivity. Figure 4(*e*) shows the results obtained for both periodic and Fibonacci approximant multilayers as a function of N. Periodic multilayers present an almost constant value of P_N for different numbers of layers. In contrast, the value of P_N for Fibonacci approximant multilayers monotonically increases with N and it is always larger than the corresponding value for periodic multilayers of the same size. In fact, whereas the number of high reflectance peaks in periodic multilayers changes only slightly on increasing the number of layers, the fragmentation process characteristic of the frequency spectrum in quasiperiodic multilayers gives rise to the occurrence of many more additional reflectivity peaks, leading to an overall increase of the reflectivity. This property clearly favours their possible use as x-ray mirrors. At the same time, the sharpness of these peaks allows for a fine tuning of different narrow lines in aperiodic multilayers. In this way, aperiodic multilayers based on high-Z/low-Z metallic layers, like those grown by alternating deposition of V/Mo, W/Ti or Ta/Al thin films, may be efficiently used as selective filters of soft x-rays [34].

What is the physical reason for the presence of such a great number of narrow reflectivity peaks in quasiperiodic systems? In essence these peaks stem from resonant interference effects as it occurs in usual periodic systems. Now, the structural self-similarity of Fibonacci multilayers along with their characteristic quasiperiodic order guarantee the existence of suitable resonance conditions *at any scale.* In the mathematical literature this important feature is referred to as *local isomorphism* and its significant role in interference processes can be described in terms of the so-called Conway's theorem (figure 5) [35].

1.4. Critical nature of light waves

Along with highly fragmented frequency spectra another typical property of most quasiperiodic systems is the presence of the so-called *critical states*. Generally speaking, critical states exhibit a rather involved oscillatory behavior, displaying strong spatial fluctuations which show distinctive self-similar features in several instances (figure 6). As we can see, the intensity distribution of the electromagnetic field inside the multilayer structure shows very high peaks in certain layers and rapidly decays to progressively reappear far away on layers

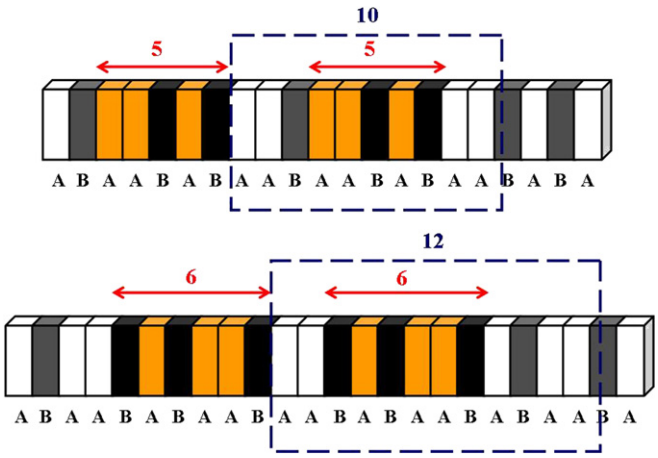

Figure 5. Illustration of the so-called Conway's theorem in a Fibonacci dielectric multilayer (FDM): given an arbitrary sequence of layers (highlighted in the picture) one will always find a replica of it at a distance smaller than twice its length (dashed boxes).

showing a similar local order. Accordingly, the notion of an envelope function, which has been most fruitful in the study of both extended and localized states, is mathematically ill-defined in the case of critical states. Note also that critically localized states require a relatively large number of layers ($N > 100$) to manifest themselves in aperiodic structures. In practice, however, the N value is limited by layer thickness control, stress relaxation and cracking. critical state 性质和实验

The existence of critical states leads to the formation of resonant standing wave patterns for those frequencies close to the band edge. These peculiar light intensity distributions can temporarily store a substantial amount of energy which is consistent with a large group velocity reduction and strong pulse stretching observed in several experiments [36]. Calculations show that the optical path drift occurring naturally during the growth of the Fibonacci multilayer triggers the localization of the first few band-edge modes, preserving their characteristic self-similar pattern [37]. Critical states were also shown to play a significant role in the luminescence properties of a Fibonacci dielectric multilayer (FDM) with an embedded organic dye, where time-resolved luminescence measurements showed a faster spontaneous emission rate arising from the large photon densities available at the band edge due to the presence of critically localized photonic states [38].

1.5. Why choose the aperiodic one?

Clear experimental indications on certain advantages of quasiperiodic systems over periodic ones were originally reported in the nonlinear optics field, where it was shown that second harmonic generation processes were more efficient in FDMs in virtue of their richer Fourier spectrum structure. In fact, as we will describe in section 2, due to their higher space-group symmetry, quasiperiodic multilayers can provide *more* reciprocal vectors to the so-called quasi-phase-matching optical process, and this ultimately results in a more plentiful spectrum structure than that of a periodic multilayer [39, 40]. The importance of the role played by the quasiperiodicity of

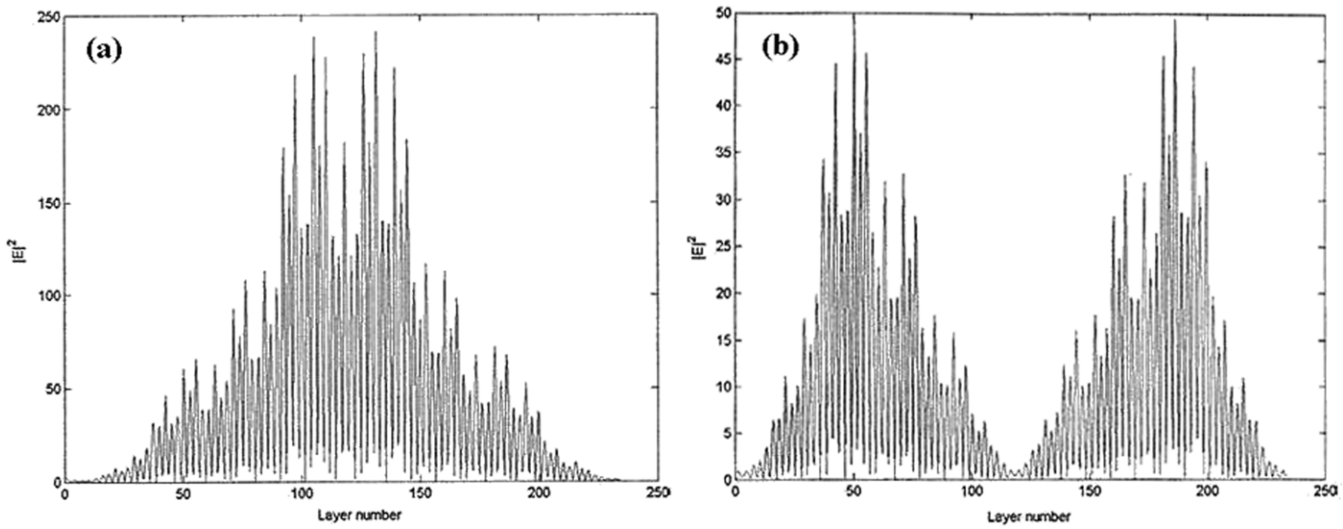

Figure 6. Calculated intensity distribution of the light inside a twelveth order Fibonacci multilayer ($N = 233$) corresponding to two representative band-edge critical states. The global mirror symmetry stems from their transient standing wave character. A closer inspection via wavelet analysis shows that the intensity distribution is self-similar [5]. (Courtesy of Diederik S Wiersma.)

the substrate is further highlighted when considering third-harmonic generation processes, where it has been shown that the conversion efficiency in a quasiperiodic multilayer is increased by a factor of eight in comparison with the two-step process required for a usual third-harmonic generator based on periodic systems [41, 42]. In a similar way, emission enhancement effects occurring at wavelengths corresponding to resonance states in light-emitting SiN/SiO_2 multilayered structures arranged according to the so-called Thue–Morse sequence (see sections 2.1 and 2.3) have been demonstrated as well [43].

The nonlinear properties of optical heterostructures can also be used to fabricate a compact-sized compressor for laser pulses. This compression is physically determined by the group velocity dispersion in the material, so one can expect that by adding more layers to a periodic multilayer one should obtain narrower optical bands and the compression effect will be increased. However, this is inevitably accompanied by an increase of the total thickness of the structure, which is undesirable. In this context, the recourse to aperiodic structures, exhibiting a significantly larger fragmentation of their optical spectrum for similar system sizes, appears as a natural choice. Inspired by this principle, the laser compression performance of both periodic and FDMs made of high-index ZnS and low-index Na_3AlF_6 layers has been experimentally compared. As expected from theoretical considerations, the Fibonacci based structure exhibits a compression enhancement due to its larger group velocity dispersion [44].

The possible use of different kinds of photonic multilayers based on porous silicon nanotechnology is currently being tested for the detection of gases, liquids and biological molecules. The sensing mechanism is based on the refractive index changes of porous silicon due to the partial substitution of the air in the pores on exposure to biochemical substances. The refraction index change is transduced, in turn, in a characteristic shift of the reflectivity spectrum. In a recent study the sensitivities of resonant optical biochemical sensors based on both periodic and Thue–Morse porous silicon multilayers were compared. The measurements clearly indicated that the aperiodic multilayer is more sensitive than the periodic one [45]. The physical reason for the observed improvement was traced back to the following properties: (i) for a given system size aperiodic multilayers have less interfaces than the periodic ones, hence exhibiting a higher filling capability, and (ii) multiple interference effects give rise to a greater number of narrower resonance transmittance peaks in the aperiodic multilayers, hence increasing their spectral resolution. These few examples nicely illustrate the main point we will address through this review, namely that carefully designed aperiodic structures can satisfactorily cope with certain physical requirements necessary for the fabrication of improved devices of technological interest. We will come back to this important issue in more detail in section 5.1.

1.6. Aperiodicity by design

So far we have considered aperiodic multilayers based on the application of certain substitution sequences in order to determine the stacking arrangements of layers through the structure. As the field of aperiodic condensed matter is coming to maturity, a logical extension naturally appears: systems whose building blocks are intentionally arranged according to purposely defined aperiodic designs able to tailor their physical properties to fit some specified requirement [7]. In this case, the guiding principle is not the previous knowledge about a sequence or a tiling with some well-known mathematical properties, but a purely technological one. In doing so, appealing aperiodic orderings are created by hand, generally following suitable optimization algorithms. Such a procedure essentially differs from the recursion methods previously considered, thereby substantially enriching the variety of aperiodic orders of interest in both fundamental and applied science domains. We will refer to the systems obtained in this way as *aperiodic systems by design*.

A first example of aperiodic system by design was derived by means of suitable optimization algorithms when searching for quasiperiodic structures able to simultaneously phase match any two nonlinear interactions in ferroelectric devices [46–48]. This procedure is an example of what is generally known as a reverse engineering problem. In such cases, the optimized structures are found by numerically solving an optimization problem where a number of optimization parameters (e.g. the layer thicknesses or the assignment of positive and negative domains in a ferroelectric multilayer) are treated as independent variables under certain physical constraints (e.g. the existence of a thickness small limit for the layers). Then, a merit function to be optimized is defined in terms of the physical magnitude of interest in the considered device. For instance, if one is interested in optimizing the reflectance $R(\lambda)$ of a coating over a given spectral range one may use a function of the form

设计 $$f = \frac{1}{N}\sum_{j=1}^{N}\left[R_0 - R(\lambda_j)\right]^2, \qquad (4)$$

where N is the total number of layers, R_0 is a reflectivity reference value, and λ is the radiation wavelength. Following this approach, a number of Mo/Si aperiodic multilayers were designed and grown in order to attain a maximum reflectivity over a specified range of wavelengths or angles of incidence for their use as XUV radiation mirrors [49], or analyzers [50]. Similar approaches have been used to design efficient aperiodic W/Si multilayer mirrors for x-ray plasma diagnostic [51], narrowband optical filters able to simultaneously tune multiple wavelengths [52], organic light-emitting diodes with improved brightness output [53], enhanced frequency converters for continuous-wave tunable lasers [54] and intensity-dependent polarization switches based on an aperiodic modulation of the nonlinear coefficient [55]. More elaborated procedures, based on the application of the so-called genetic algorithm [56], have been successfully applied in order to design omnidirectional reflectors [57].

2. Layered optical systems

2.1. Aperiodic dielectric multilayers

2.1.1. Experimental realizations. The first fabrication of a semiconductor-based quasiperiodic Fibonacci superlattice was reported on 21 October 1985 [18]. In the related patent application, the possible use of materials other than semiconductors for the constituent layers, including dielectrics, was claimed. Shortly afterward, the appealing possibility of probing the degree of localization of electromagnetic waves propagating through an optical multilayer constructed following the Fibonacci sequence was originally proposed [58]. This theoretical proposal spurred the interest for possible optical applications [59], as well as for new theoretical aspects of light transmission in aperiodic media [60, 61]. In subsequent works, the optical transmission of an FDM composed of stacks of SiO_2 and TiO_2 thin films was reported [62, 63]. Relative film thicknesses were chosen such that the phase shift for normally incident light was the same, i.e. $n_A d_A = n_B d_B$. Furthermore, the individual layers were taken as quarter-wave layers, since previous theoretical results indicated that quasiperiodicity effects are enhanced in this case. The rapid progress achieved in growth technologies, like molecular beam epitaxy, magnetron sputtering, or vacuum deposition, made it possible to grow artificial structures with different aperiodic modulations of chemical composition along the growth direction. For the sake of illustration in table 1 we list some representative aperiodic multilayers considered for optical applications during the last two decades.

Table 1. Some representative aperiodic multilayers grown to date arranged in chronological order. Most metallic multilayers have been grown by magnetron sputtering (MS) and molecular beam epitaxy (MBE), whereas dielectric multilayers have been grown by vacuum deposition (VD), lithographic techniques (L), electric poling (EP) or electrochemical etching (EE).

Layer material	Sequence	N	Growth technique	Year/Ref
Nb/Cu	Fibonacci	377	MS	1986 [64]
Nb/Ta	Fibonacci	89	MBE	1988 [65]
$LiNbO_3$	Fibonacci	34	L	1989 [66]
Mo/V	Precious means	144	MS	1990 [67]
Ta/Al	Ternary Fibonacci	189	MS	1992 [68]
SiO_2/TiO_2	Fibonacci	55	VD	1994 [63]
W/Ti	Fibonacci	—	MS	1996 [34]
$LiTaO_3$	Fibonacci	377	EP	1997 [39]
PbS/CdS	Fibonacci	—	VD	1997 [69]
PbS/CdS	Thue–Morse	—	VD	1997 [69]
Na_3AlF_6/ZnS	Cantor	27	VD	2002 [32]
Si/SiO_2	Thue–Morse	32	MS	2004 [70]
porous Si	Thue–Morse	64	EE	2007 [45]
porous Si	Period-doubling	128	EE	2009 [71]
porous Si	Rudin–Shapiro	128	EE	2009 [71]

As we can see, FDMs were intensively studied during the 1980s and 1990s, since they provide a canonical example of quasiperiodic structures for optical applications, but interest has progressively moved on toward other classes of aperiodic structures which also exhibit interesting photonic properties. The optical properties of multilayers based on the *Thue–Morse* sequence have also received a considerable attention during the last two decades [60, 72–74]. This popular sequence has been extensively studied in the mathematical literature as the prototype of a sequence generated by the substitution rule $A \to AB$ and $B \to BA$. In this case the continued process reads $A \to AB \to ABBA \to ABBABAAB \to ABBABAABBAABABBA \to \ldots$. The number of letters in this sequence increases geometrically, $N = 2^k$, where k indicates the iteration order. In the infinite limit the relative frequency of both kinds of letters in the sequence takes on the same value, i.e. $\upsilon_A = \upsilon_B = 1/2$. This result contrasts with that corresponding to the Fibonacci sequence, where $\upsilon_A = \tau^{-1}$, and $\upsilon_B = \tau^{-2}$, where τ is the so-called *golden mean* value $\tau \equiv (1+\sqrt{5})/2 \simeq 1.618\ldots$ [7, 19]. Another important difference is that in the Fibonacci sequence B letters always appear isolated, whereas in Thue–Morse sequence both dimers AA and BB appear alike.

The introduction of the so-called *period-doubling* sequence originated in the theory of dynamical systems. For

this sequence the substitution rule reads $A \to AB$ and $B \to AA$, and the continued process gives $A \to AB \to ABAA \to ABAAABAB \to \ldots$ The number of letters in this sequence increases as $N = 2^k$ (like the Thue–Morse sequence) but letters B appear always isolated (like the Fibonacci sequence) and their relative frequency in the infinite limit is $\upsilon_A = 2/3$, and $\upsilon_B = 1/3$, respectively.

The so-called *precious mean* sequences are defined by the substitution rule $A \to A^n B$, $B \to A$ (alternatively, $A \to ABA^{n-1}$, $B \to A$), whereas the so-called *metallic mean* sequences are defined by the substitution rule $A \to AB^n$, $B \to A$. Among the members of the former family we find the golden mean (Fibonacci, $n = 1$), silver mean ($n = 2$) or bronze mean ($n = 3$), whereas we find copper ($n = 2$) and nickel ($n = 3$) means as representative members of the latter. The silver mean sequence is also referred to as the *Octonacci* sequence, named after 'octo' for octagonal and '-acci' after Fibonacci, and describes the sequence of spacing of the Ammann–Beenker tiling (see section 3.3.1). It can be generated in analogy to the Fibonacci sequence by the substitution rule $A \to AAB$, $B \to A$. The number of layers at a given generation order is given by the Pell numbers, which are obtained from the recursion relation $F_{j+1} = 2F_j + F_{j-1}$, with $F_0 = 0$, $F_1 = 1$ [14]. The optical transmission spectra of multilayers based on the metallic mean sequences (which are self-similar *but not* quasiperiodic) were numerically compared with those of multilayered structures based on the precious means (which are both self-similar and quasiperiodic). The observed differences nicely illustrate the fact that both kinds of aperiodic systems belong to different aperiodic order classes [60, 75]. In contrast, the main features of the transmission spectra corresponding to different representatives of multilayers based on quasiperiodic precious mean sequences are essentially the same [76].

Different generalizations of the Fibonacci sequence, preserving both the inflation self-similarity and the long-range quasiperiodic order characteristic of the original Fibonacci sequence, have been considered in the literature for optical applications. A representative example is provided by the so-called *Fibonacci-class* sequence family, generated from the substitution rule $A \to B^{n-1}AB$, $B \to B^{n-1}A$, which has the same algebraic structure as that of precious means [77–80]. It was analytically shown that, under quarter wave condition at normal incidence geometry, the transmission coefficient of Fibonacci-class dielectric multilayers with even n displays a switch-like property for those wavelengths satisfying the condition $\lambda_l = 2n_i d_i (l \pm \frac{1}{2})$. This means that, depending on the parity of the generation order, the transmission coefficient alternatively takes on either a constant value (determined by the refraction index contrast) or an ever decreasing value which completely vanishes in the quasiperiodic limit $N \to \infty$ [78]. Thus, for even (odd) values of the generation order we, respectively, have the on (off) transmission behavior. We note that in order to fully appreciate the 'off' switch property one must consider long enough multilayers.

Alternative generalization routes consider concatenation rather than substitution rules. Thus, both precious and metallic mean sequences can be described in a unified way in terms of the general concatenation rule $S_{j+1} = S_j^n S_{j-1}^m$ ($j \geqslant 1$) starting with $S_0 = B$ and $S_1 = A$. When $m = 1$ we obtain quasiperiodic sequences, whereas for $m \geqslant 2$ one obtains non-quasiperiodic sequences [81]. On the other hand, the Octonacci sequence can be obtained from the concatenation rule $S_{j+1} = S_j S_j S_{j-1}$ ($j \geqslant 1$) starting with $S_0 = B$ and $S_1 = A$. Within this context the so-called *Tribonacci* multilayer is defined in terms of a layer sequence given by the concatenation rule $S_{j+1} = S_j S_{j-1} S_{j-2}$ ($j \geqslant 2$) starting with $S_0 = B$, $S_1 = AB$ and $S_2 = ABAB$. The number of layers at a given generation order is given by the Tribonacci numbers, which are obtained from the recursion relation $F_{j+1} = F_j + F_{j-1} + F_{j-2}$, with $F_0 = 0$, $F_1 = F_2 = 1$, and m-bonacci multilayers can be introduced in an analogous way [82].

Certainly, there exist many possible ways of arranging a series of different layers in an ordered aperiodic way without recurring to substitution sequences. For instance, a very interesting alternative based on tessellations of the hyperbolic plane by regular polygons has recently been reported [83]. As another example, one may consider a binary multilayer where each layer is labeled by a natural number in such a way that, say, A layers correspond to prime numbers [84]. Since the number of primes progressively decays as one goes to larger integers the relative frequency of A layers vanishes as the system grows longer. Therefore, A layers can be regarded as some sort of diluted impurity layers. Nevertheless, an interesting property of primes is that they do not come infrequently in pairs (called twin primes) like the couples (11,13) or (17,19), for instance. In this way, twin primes introduce a short-range correlated disorder among the A layers, and one expects that the presence of these correlations will give rise to the emergence of certain resonance effects in such multilayers [85, 86].

Up to now, we have considered multilayers composed of two different kinds of material layers. However, it has been experimentally confirmed that ternary Fibonacci multilayers composed of three kinds of Ta/Al bilayer building blocks also diffract, which is a characteristic property of the long-range order present in quasiperiodic systems [68]. On the other hand, optical transmission through multicomponent Thue–Morse multilayers has recently been reported [87].

2.1.2. Transfer matrix techniques. In order to properly compare the optical responses of periodic and quasiperiodic 1D multilayered systems, the transfer matrix technique is particularly well suited, since it describes the light behavior in contiguous layers. The simplest approach focuses on aperiodic multilayers composed of linear, homogeneous, lossless materials with no optical activity, embedded in a medium of refractive index n_M. The transfer matrix describing the light propagation from the ith layer to the $(i+1)$th layer is [24, 88, 89]

$$\boldsymbol{K}_{i,i+1} = \begin{pmatrix} \cos\delta_i & -q_{i,i+1}\sin\delta_i \\ q_{i,i+1}^{-1}\sin\delta_i & \cos\delta_i \end{pmatrix}, \qquad (5)$$

where $\delta_i \equiv n_i d_i k \cos\theta_i$ is the layer phase thickness, n_i is the layer refractive index, d_i is the layer width, $k = 2\pi/\lambda$ is the wave vector of the incident radiation in vacuum, and θ_i is the refraction angle determined by Snell's law. The parameter

$q_{i,i+1}$ describes the propagation across the interface separating two neighboring layers and can be written as

$$q_{i,i+1}(s) = \frac{n_i \cos\theta_i}{n_{i+1}\cos\theta_{i+1}}, \qquad q_{i,i+1}(p) = \frac{n_{i+1}\cos\theta_i}{n_i \cos\theta_{i+1}} \quad (6)$$

for each basic polarization s (TE) or p (TM), respectively. We note that $q_{i+1,i} = q_{i,i+1}^{-1}$. The transmission of light through a binary multilayer composed of two different materials, labeled A and B, can be properly described in terms of a product involving the matrices $\boldsymbol{K}_{AA}$, $\boldsymbol{K}_{BB}$, $\boldsymbol{K}_{AB}$ and $\boldsymbol{K}_{BA}$, along with the boundary matrices $\boldsymbol{K}_{LA}$, $\boldsymbol{K}_{AL}$, $\boldsymbol{K}_{LB}$ and $\boldsymbol{K}_{BL}$, where $L = \{0, N+1\}$. The transmittance can then be obtained from the standard expression [90]

$$T_N = \frac{4(\det \mathcal{M}_N)^2}{||\mathcal{M}_N|| + 2\det \mathcal{M}_N}, \quad (7)$$

where $\mathcal{M}_N \equiv \prod_{i=N}^{0} \boldsymbol{K}_{i,i+1}$ is the multilayer transfer matrix, and the norm $||\mathcal{M}_N||$ denotes the sum of the squares of the four elements of $\mathcal{M}_N$. We note that the $\boldsymbol{K}_{i,i+1}$ matrices are all of them unimodular (i.e. their determinant is unity) so that $\det \mathcal{M}_N = 1$ and (7) can be simplified accordingly.

To start with, let us consider a multilayer made of a certain number, ν, of bilayers AB which repeat periodically. In this case, assuming periodic boundary conditions for the sake of simplicity, the multilayer transfer matrix can be straightforwardly expressed in the form $\mathcal{M}_N = (\boldsymbol{K}_{BA}\boldsymbol{K}_{AB})^{\nu} \equiv \boldsymbol{Q}^{\nu}$, where $N = 2\nu$ is the total number of layers and

$$\boldsymbol{Q} = \begin{pmatrix} \cos\delta_A\cos\delta_B - q^{-2}\sin\delta_A\sin\delta_B & \\ q\cos\delta_A\sin\delta_B + q^{-1}\sin\delta_A\cos\delta_B & \\ -(q^{-1}\cos\delta_A\sin\delta_B + q\sin\delta_A\cos\delta_B) & \\ \cos\delta_A\cos\delta_B - q^{2}\sin\delta_A\sin\delta_B & \end{pmatrix}, \quad (8)$$

where $q \equiv q_{A,B}$. Since $\boldsymbol{Q}$ is unimodular we can make use of the Cayley–Hamilton theorem in order to explicitly evaluate the matrix $\mathcal{M}_N$. According to this theorem any $n \times n$ unimodular square matrix $\boldsymbol{M}$ over the real or complex field is a root of its own characteristic polynomial, so that one obtains by induction the expression [91]

$$\boldsymbol{M}^N = U_{N-1}(z)\boldsymbol{M} - U_{N-2}(z)\boldsymbol{I}, \quad (9)$$

where $\boldsymbol{I}$ is the identity matrix, and $U_N \equiv [\sin(N+1)\psi]/\sin\psi$, with $\psi \equiv \cos^{-1} z$, are Chebyshev polynomials of the second kind satisfying the recursion relation

$$U_{n+1} - 2zU_n + U_{n-1} = 0, n \geqslant 1 \quad (10)$$

with $U_0(z) = 1, U_1(z) = 2z$, and $z = \mathrm{tr}\boldsymbol{M}/2$. Plugging (8) into (9) and taking into account the relationship $T_n = zU_{n-1} - U_{n-2}$, where $T_n(z) = \cos(n\cos^{-1} z)$ are Chebyshev polynomials of the first kind, one obtains

$$\mathcal{M}_N = \begin{pmatrix} T_\nu + \gamma U_{\nu-1}\sin\delta_A\sin\delta_B & -\Upsilon_+ U_{\nu-1} \\ \Upsilon_- U_{\nu-1} & T_\nu - \gamma U_{\nu-1}\sin\delta_A\sin\delta_B \end{pmatrix}, \quad (11)$$

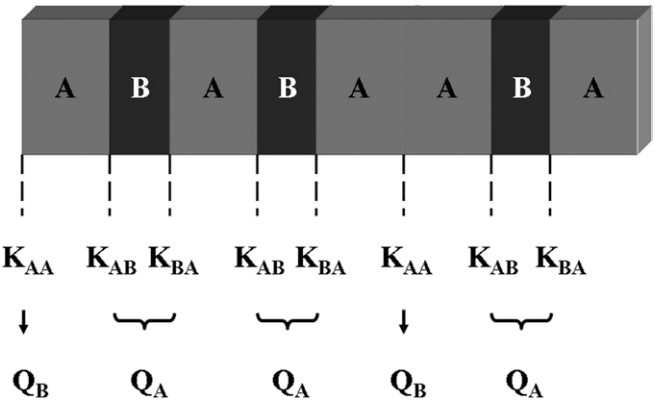

Figure 7. Sketch illustrating the sequence of layer transfer matrices $\boldsymbol{K}_{i,i+1}$ through a FDM and the corresponding sequence of renormalized transfer matrices $\boldsymbol{Q}_A$ and $\boldsymbol{Q}_B$.

where $\gamma \equiv (q^2 - q^{-2})/2$, $\Upsilon_\pm \equiv q^{\pm 1}\sin\delta_A\cos\delta_B + q^{\mp 1}\cos\delta_A\sin\delta_B$, and

$$z \equiv \frac{1}{2}\mathrm{tr}\boldsymbol{Q} = \cos\delta_A\cos\delta_B - \frac{q^2+q^{-2}}{2}\sin\delta_A\sin\delta_B. \quad (12)$$

Finally, making use of (11) into (7) one obtains the transmittance

$$T_\nu = \left\{1 + a^2\left[\sin^2(\delta_A - \delta_B) + b^2\sin^2\delta_A\sin^2\delta_B\right]U_{\nu-1}^2(z)\right\}^{-1}, \quad (13)$$

where $a \equiv (q - q^{-1})/2$ and $b \equiv q + q^{-1}$. It can be readily checked that the expressions (12) and (13) are invariant under the exchange $\delta_A \leftrightarrow \delta_B$, as required. Physically this result indicates that the optical properties of the periodic multilayer with unit cell AB remain exactly the same when the layers A and B are mutually permuted.

Let us now consider an FDM consisting of two kinds of layers, labeled A and B. Since the presence of BB layers is excluded by construction in the Fibonacci sequence, the multilayer transfer matrix is given by a matrix product involving three different types of transfer matrices ($\boldsymbol{K}_{AA}$, $\boldsymbol{K}_{BA}$ and $\boldsymbol{K}_{AB}$) which, in addition, are quasiperiodically ordered. At this point, we introduce a renormalization technique in order to derive analytical expressions for the transmittance curves [16, 92, 93]. The key point consists in renormalizing the set of transfer matrices appearing in the matrix string $\mathcal{M}_N \equiv \prod_{i=N}^{0}\boldsymbol{K}_{i,i+1}$, according to the blocking scheme $\boldsymbol{Q}_B \equiv \boldsymbol{K}_{AA}$ and $\boldsymbol{Q}_A \equiv \boldsymbol{K}_{BA}\boldsymbol{K}_{AB} = \boldsymbol{Q}$. In this way, the multilayer transfer matrix can be expressed in terms of the iterative formula $\mathcal{M}_j = \mathcal{M}_{j-1}\mathcal{M}_{j-2}$, $j \geqslant 3$, with $\mathcal{M}_1 = \boldsymbol{Q}_B$ and $\mathcal{M}_2 = \boldsymbol{Q}_A$. Note that the renormalized transfer matrix sequence is also arranged according to the Fibonacci sequence (see figure 7). Consequently, the topological order present in the original FDM is preserved by the renormalization process. Now, we realize that matrices $\boldsymbol{Q}_A$ and $\boldsymbol{Q}_B$ commute under certain circumstances. In fact, the commutator

$$[\boldsymbol{Q}_A, \boldsymbol{Q}_B] = -2\gamma\sin\delta_A\sin\delta_B\begin{pmatrix} -\cos\delta_A & q\sin\delta_A \\ q^{-1}\sin\delta_A & \cos\delta_A \end{pmatrix} \quad (14)$$

vanishes in three different cases, namely $\gamma = 0$, and the choices $\delta_A = m_1\pi$ or $\delta_B = m_2\pi$, where $m_1, m_2 \in \mathbb{Z}$ and

$m_1 \neq m_2$ in general. Therefore, in order to satisfy the commutation condition (14), it is *not* necessary to impose restrictive conditions onto both kinds of layers *simultaneously*. The condition $\gamma = 0$ is satisfied for the special cases $R\beta = \pm 1$ (s polarization) and $R^{-1}\beta = \pm 1$ (p polarization), where $R \equiv n_A/n_B$ measures the refraction index contrast and $\beta \equiv \cos\theta_A/\cos\theta_B$. Note that under normal incidence conditions this condition reduces to the trivial periodic case $n_A = n_B$ for both polarizations. For those wavelengths verifying the condition $[\boldsymbol{Q}_A, \boldsymbol{Q}_B] = 0$, we can express the global transfer matrix of the system as $\mathcal{M}_N \equiv \boldsymbol{Q}_A^{F_{j-2}} \boldsymbol{Q}_B^{F_{j-3}}$. Since $\boldsymbol{Q}_A$ and $\boldsymbol{Q}_B$ are unimodular for any choice of the system parameters and for any value of the light wavelength one can exploit the Cayley–Hamilton theorem in order to explicitly evaluate $\mathcal{M}_N$ in terms of Chebyshev polynomials, as we did in the study of the periodic case.

2.1.3. Resonance effects. Taking into account the above commutation conditions we can consider three different possible situations:

- In the case $\delta_A = m_1\pi$ and $\delta_B = m_2\pi$, one obtains $\boldsymbol{Q}_B = (-1)^{m_2}\boldsymbol{I}$ and $\boldsymbol{Q}_A = (-1)^{m_1+m_2}\boldsymbol{I}$. Accordingly, the transparency condition, $T_N = 1$, is trivially obtained. The particular case $\delta_A \equiv \delta_B = m\pi$ implies $R\beta = \eta$, where $\eta \equiv d_B/d_A$ measures the filling factor. Physically it requires the half-wavelength condition to be satisfied at every layer.
- In the case $\delta_B = m_2\pi$, with arbitrary δ_A, one obtains $T_N = (1 + a^2 \sin^2\alpha)^{-1}$, where $\alpha \equiv F_{j-1}\delta_A$. Physically this result can be easily interpreted if we keep in mind that, when the B layers satisfy the full transmission condition, the transmission properties of the FDM will depend entirely on the interaction of light with the layers of material A. Now, since the optical behavior of the double layers AA is completely equivalent to that of single A layers and, according to the Fibonacci sequence, B layers always appear flanked by A layers, those wavelengths satisfying the resonance condition $m_2\lambda = 2n_B d_B \cos\theta_B$ will effectively *see* a *periodic* distribution of A layers separated by fully transparent slabs of constant width d_B. In this case the two-component FDM will behave like an equivalent homogeneous *periodic* medium, characterized by an effective thickness $d' \equiv F_{j-1}d_A$, and a refraction index n_A. Note that, if instead of imposing the half-wavelength condition onto B layers, we make the substitution $B \to A$, replacing all the B type layers originally present in the FDM by type A ones, we should obtain a homogeneous system of length $Nd_A > d'$. Consequently, the FDM will exhibit an effective *optical phase shrinkage* for those wavelengths satisfying the resonance condition. It should be noted, however, that this effect is a generic property of any system exhibiting short-range correlations, and, therefore, it is not specific of self-similar arrangements. In fact, a similar behavior was reported in photonic crystals with correlated disorder [94].
- This physical scenario substantially changes if we impose the condition $\delta_A = m_1\pi$, so that the layers of material A become fully transparent to the incoming light and, consequently, the transmission properties of the FDM will depend on the interaction of light with the layers of material B. The key point now is to realize that these layers are spaced by *two different* distances, d_A and $d_{AA} = 2d_A$, arranged according to a quasiperiodic sequence. Hence, those wavelengths satisfying the resonance condition $m_1\lambda = 2n_A d_A \cos\theta_A$, will effectively see a quasiperiodic distribution of B layers, instead of a periodic one. In this case, the transmittance reads [92]

$$T_N = \frac{1}{1 + a^2 \sin^2(F_{j-2}\varphi)}, \tag{15}$$

where $\varphi = m_1\pi\eta(R\beta)^{-1}$. Under normal incidence conditions ($\beta = 1$) the curve $T(\eta)$ is symmetrical with respect to the axis $\eta = R$ and it exhibits a series of maxima ($T_{\max} = 1$) and minima ($T_{\min} = (1 + a^2)^{-1}$).

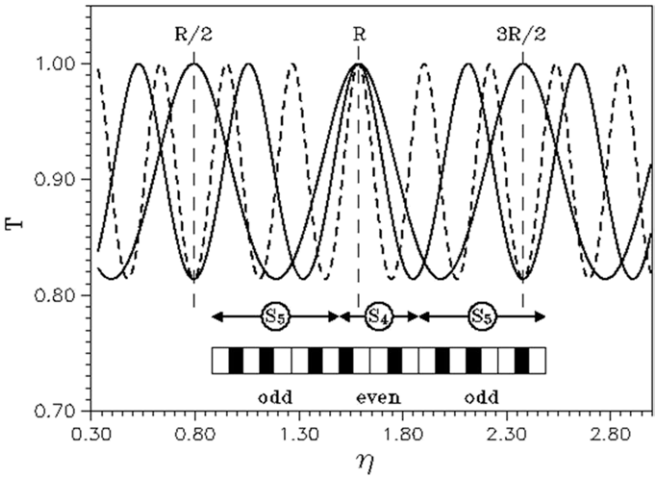

Figure 8. Dependence of the transmission coefficient with the design parameter η, for $m_1 = 1$ and $\beta = 1$, corresponding to S_4 (thick solid line), S_5 (thin solid line), and S_6 (dashed line) FDMs. We have considered that A (B) layers are composed of TiO_2 (SiO_2) whose indices of refraction (at 700 nm) are $n_A = 2.30$ and $n_B = 1.45$, respectively. The inset shows a scheme for a FDM resonating microcavity. Reprinted with permission from [92]. Copyright 1998, American Institute of Physics.

In figure 8 we show the dependence of the transmittance with η for three FDMs containing $N = 5$, $N = 8$ and $N = 13$ layers for s polarization at normal incidence. Physically the origin of the transmittance oscillatory patterns can be understood as follows. Under the A layer resonance condition, the constructive or destructive nature of the interferences, arising from the interaction of light with the quasiperiodic distribution of B layers, will be strongly dependent on the precise relationship between λ and the structural parameters d_A and d_B. Thus, when $\eta = R$ we obtain the well-known relationship $n_A d_A = n_B d_B$, corresponding to the particular case where both A and B layers simultaneously satisfy the resonance condition. Conversely, if we choose the value of η in such a way that the wavelengths satisfying the resonance condition at the A layers verify the quarter-wavelength condition at the B layers, the quasiperiodic

distribution of B layers efficiently backscatters the incoming light, resulting in a significant reduction of the transmittance value. For any choice of the parameter η other than those just described, the transmittance will adopt different values in the interval $T_{\min} \leqslant T \leqslant 1$. By inspecting this figure we observe that the number of both maxima ($T_{\max} = 1$) and minima ($T_{\min} \simeq 0.814$) increases as the FDM size increases, and their relative positions shift with respect to the symmetry axis $\eta = R = 1.5862\ldots$ Interestingly, figure 8 shows that there exists a significant number of *additional* values of η for which transparency condition is satisfied in FDMs of different lengths. Accordingly, η can be regarded as a *control design parameter* able to determine the overall FDM optical behavior, varying from that corresponding to a selective filter ($T = 1$) to that proper of a reflective coating ($T_{\min}$). In fact, plugging $m_1 = \beta = 1$ in (15) we see that, when $\eta = R/2$ or $\eta = 3R/2$, the transmittance attains an extreme value, which should be a minimum or a maximum depending on the *parity* of the Fibonacci number F_{j-2}: when F_{j-2} is even we obtain $T_N = 1$, while for odd values we have $T_N = T_{\min}$. Since the parity of the Fibonacci numbers exhibits the recurrence odd–odd–even, the transmittances corresponding to consecutive S_j FDMs should alternate accordingly, as it is illustrated in figure 8 for FDMs corresponding to $F_{j-2} = 2$, $F_{j-2} = 3$ and $F_{j-2} = 5$. This interesting property can be used to construct resonating optical cavities where an 'even' FDM (for instance S_4), exhibiting full transmission, is sandwiched between two 'odd' FDMs (for instance S_5), behaving as optical mirrors (inset, figure 8).

As discussed above, in order to compare the relative performance of quasiperiodic and periodic dielectric multilayers it is convenient to focus on the case $\delta_A = m_1\pi$. In doing so, (13) and (15) are conveniently rewritten in the form [93],

$$T_N^{QP} = \frac{1}{1 + A(R,x)\sin^2\left[F_{j-2}\, b_{m_1}(R,x,\eta)\right]}, \tag{16}$$

and

$$T_\nu^{P} = \frac{1}{1 + A(R,x)\sin^2\left[\nu\, b_{m_1}(R,x,\eta)\right]}. \tag{17}$$

where we made use of Snell's law, $R\sin\theta = \sin\theta_B$, $(\theta_A \equiv \theta)$ to introduce the auxiliary variable $x \equiv \sin^2\theta$, describing the light incidence geometry, and we have also introduced the auxiliary functions

$$A_s(R,x) \equiv \left[\frac{R^2-1}{2R}\right]^2 (1-x)^{-1}(1-R^2x)^{-1}, \quad (s \text{ polarization}) \tag{18}$$

$$A_p(R,x) \equiv A_s(R,x)[(1-(1+R^2)x]^2, \quad (p \text{ polarization}) \tag{19}$$

and

$$b_{m_1}(R,x,y) \equiv m_1\pi y\sqrt{\frac{1-R^2x}{1-x}}, \tag{20}$$

where $y \equiv \eta/R = n_B d_B/n_A d_A$, measures the phase ratio between both dielectric layers at normal incidence conditions.

In figure 9 we show the dependence of the transmittance with the phase ratio y for a periodic multilayer with $\nu = 4$ (dashed line) and an FDM with $F_{j-2} = 3$ (solid line), both

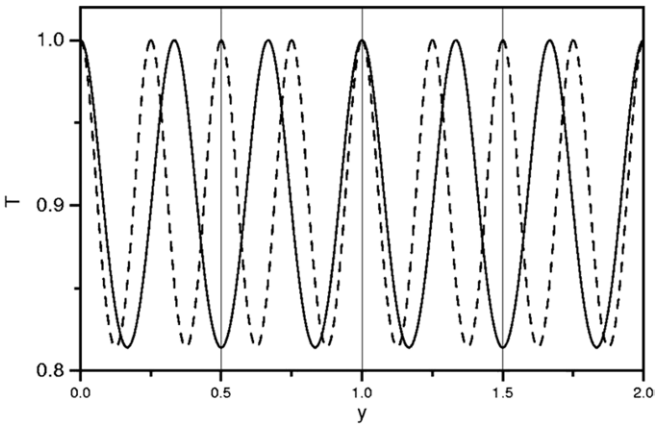

Figure 9. Dependence of the transmission coefficient with the phase ratio y for a periodic multilayer with $\nu = 4$ (dashed line) and a FDM containing $N = 8$ layers (solid line), under normal incidence geometry and $m_1 = 1$. We have taken $n_A = 1.45$ and $n_B = 2.30$. The vertical lines indicate the phase ratios satisfying the condition $y = 1/2$ and $y = 3/2$, respectively. (Adapted from [93].)

of them containing $N = 8$ layers, under normal incidence conditions. This figure exhibits a series of maxima and minima similar to those plotted in figure 8. Nevertheless, the physical origin of such an oscillatory pattern is somewhat different in this case. Thus, when $y = 1$ ($n_A d_A = n_B d_B$) both A and B layers simultaneously satisfy the resonance condition, and the long-range order of the layer sequence becomes irrelevant. However, for $y \neq 1$ the optical response of periodic and quasiperiodic multilayers progressively differs as the phase ratio is progressively increased (or decreased), in the way displayed in figure 9. A particularly interesting situation occurs if we choose the phase ratio value in such a way that the wavelengths satisfying the half-wavelength condition at the A layers of the periodic multilayer verify the quarter-wavelength condition at the B layers of the FDM. In this case, the quasiperiodic distribution of B layers efficiently backscatters the incoming light, resulting in a significant reduction of the transmission coefficient value. Conversely, the periodic multilayer exhibits full transmission for the same wavelength. This behavior opens the possibility of constructing a mixed device composed of both periodically and quasiperiodically arranged multilayers, so that the refractive index contrast and the layer thicknesses determining the phase ratio value act as *control design parameters* able to determine the optical response of their different constitutive substructures from that corresponding to a selective filter ($T = 1$) to that proper of a reflective coating ($T_{\min}$).

Such a complementary behavior can be further exploited under oblique angle incidence conditions. In figure 10 we show the dependence of the transmission coefficient with the angle of incidence for the periodic multilayer (dashed line) and FDM (solid line) previously considered in figure 9, for the case $\eta = R$. By inspecting figure 10 we can distinguish several regimes. At low incidence angles the optical response of both periodic and quasiperiodic multilayers is quite similar, although the transmission curve for the FDM systematically departs from that corresponding to the periodic multilayer, exhibiting larger transmittance values. The regime labeled I starts at the

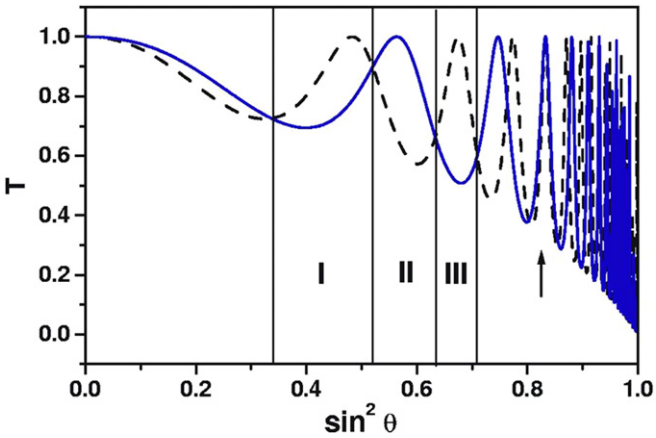

Figure 10. Dependence of the transmission coefficient with the angle of incidence θ for a periodic multilayer with $\nu = 4$ (dashed line) and an FDM containing $N = 8$ layers (solid line) for the case $m_1 = y = 1$, $n_A = 1.45$ and $n_B = 2.30$.

angle value $x \simeq 0.34$ where a crossing point between both transmission curves occurs. Afterward, the transmission curve for the periodic multilayer suddenly grows as the incidence angle is increased, reaching a broad peak at $x \simeq 0.48$ ($\theta \simeq 44^\circ$) and it rapidly decreases again to reach another crossing point with the quasiperiodic multilayer transmission curve at $x \simeq 0.52$. A similar oscillatory pattern repeats itself as the incidence angle is further increased, determining the subsequent crossing points defining the angle intervals labeled II and III. The most relevant feature of the interval III is the existence of a relatively broad incidence angle range where periodic and quasiperiodic multilayers, respectively, exhibit *complementary optical responses*, in the sense that when one of them exhibits high T values the other one exhibits low T values. In this way, the complementary optical response previously reported under normal incidence conditions also holds for the more general case of oblique incidence geometry. On the other hand, there also exist angle intervals where the transmittance of both periodic and quasiperiodic multilayers is almost indistinguishable (arrow in figure 10).

In summary, by properly choosing the different design parameters, as determined by the refractive index contrast, R, and the multilayer filling factor, η, we can select specific resonance conditions, matching the wavelength of the incoming light to some of the different characteristic lengths present in the aperiodic substrate. In addition, we can also play with the incidence angle geometry of the incoming light in order to further exploit the capabilities previously determined by the architecture of the multilayer. In fact, the most relevant feature of the transmission curves shown in figures 9 and 10 is the possibility of constructing resonating optical devices that exploit the richer interference patterns associated with the coexistence of different kinds of topological order (i.e. periodic and quasiperiodic order) in a given substrate. In this way, plentiful possibilities for new tailored materials naturally appear.

2.2. Hybrid order multilayers

2.2.1. Blending periodic and aperiodic orderings. As we have just seen, one may think of fabricating *mixed* devices composed of both periodically and quasiperiodically arranged multilayers in order to obtain new capabilities. Such a mixed structure can be viewed as a *hybrid order device* made of two different kinds of subunits, each one exhibiting a different kind of topological ordering, respectively, leading to *complementary* transmittance curves. The key point here is that such a complementary behavior can be obtained by just changing the kind of *topological order* in the stacking sequence of layers composing each subunit, so that both the chemical nature of the different layers and the wavelength of the incoming light remain unchanged. This is a quite remarkable result, since the pertinent codes to alternate between periodic and quasiperiodic orderings in the growing structure can easily be implemented in current state-of-the-art deposition processes [7, 93]. The introduction of these subunits endows the system with an *additional design parameter*, bridging the gap between the atomic level characteristic of the microstructural domain of each layer and the mesoscale level associated with the long-range order of the entire device as a whole. Therefore, since each subunit can sustain a specific kind of order (i.e. periodic or aperiodic) we are able to introduce a *modular design* in the multilayered structure by properly selecting the ordering sequence in each subunit. Certainly, there are many ways of constructing different hybrid order structures, opening a broad avenue to design new kinds of multilayered systems. Thus, one may mix together different kinds of aperiodic sequences, for instance, Fibonacci/Thue–Morse/Fibonacci or Fibonacci/Thue–Morse/Rudin–Shapiro and so on. A graphical account of some possible designs is shown in figure 11. The combination of Fibonacci and Cantor modules as that shown in figure 12 has also been recently proposed in order to design omnidirectional reflectors [95]. From a fundamental point of view, the interest of this type of hybrid order structure relies on the fact that it is based on the juxtaposition of a typical quasiperiodic structure exhibiting self-similar features (Fibonacci) with a perfectly self-similar structure which is not quasiperiodic at all (Cantor).

The hybrid order based modular design can easily be used to construct broad omnidirectional reflectors on the basis of complementary photonic band gap (PBG) superposition. The main idea is that narrow gaps appearing in the highly fragmented quasiperiodic units compensate for the relatively broad band regions appearing in the periodic ones. Thus, it has been numerically shown that the omnidirectional reflection range of an FDM can be enlarged by combining the Fibonacci structure with a periodic one so that the resulting modular structure exhibits a broader omnidirectional reflection region than that obtained for each of the composing modules independently considered [96]. In this way, one can optimize engineered combinations of quasiperiodic and periodic *short* multilayered stacks in order to obtain thin photonic heterostructures (e.g. $[ABA]^4[BAABA]^2[BA]^7$), exhibiting large omnidirectional reflection [97].

In the same vein, the possible use of hybrid order structures of the form periodic/Cantor/periodic or periodic/GTM/periodic dielectric multilayer has also been proposed for application as a polychromatic filter [98–100]. Here

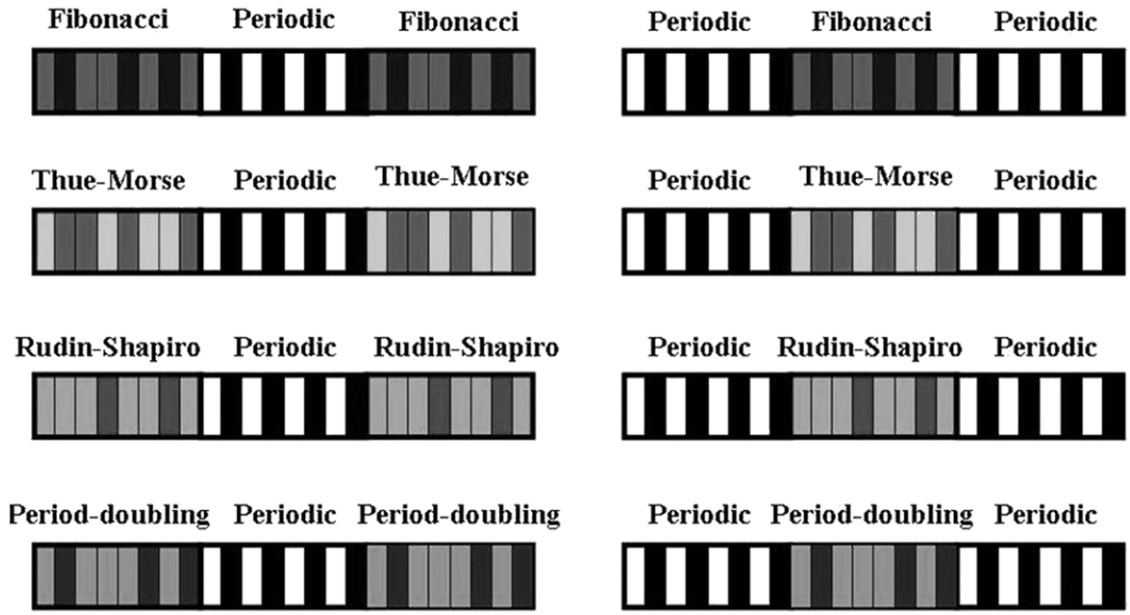

Figure 11. Diagram showing different possible sequence designs of hybrid systems obtained by combining periodic and aperiodic multilayers.

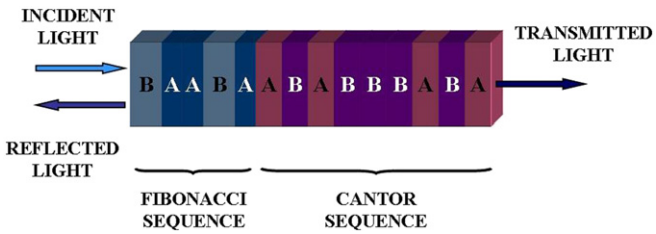

Figure 12. Schematic representation showing a fourth generation Fibonacci/third generation Cantor structure. (Adapted from [95].)

GTM stands for the generalized Thue–Morse quasiperiodic sequence, which can be either obtained from the substitution rule $A \to A^n B^m$, $B \to B^m A^n$, or $A \to A^m B^n$, $B \to B^n A^m$ [101]. In figure 13 we show the transmission spectrum for the periodic/GTM/periodic hybrid structure as derived from transfer matrix calculations. By comparing figures 13(*a*) and (*b*) we see that the inclusion of the third order approximant (with $n = 1$ and $m = 2$) module $ABBBBABBA$ in between the $A[BA]^4$ periodic ones leads to the presence of two narrow peaks around the reference wavelength $\lambda_0 = 0.5\,\mu$m. Due to multiple interference effects, the number of full transmission peaks increases substantially (and they become progressively narrower) as the number of encased quasiperiodic approximants, l, is progressively increased in the hybrid order multilayer (figure 13(*c*)).

Intimately related to these modifications in the overall spectral structure, one may expect that the competition between highly fragmented spectra supporting critical eigenstates (a characteristic feature of quasiperiodic systems) and continuous spectra possessing Bloch eigenfunctions (typical of periodic systems) should give rise to some peculiar eigenstates in these hybrid structures. Thus, the existence of selectively localized optical modes in Fibonacci/periodic/Fibonacci porous silicon based multilayers has been reported [102].

2.2.2. Conjugated and mirror symmetries. One may also consider systems entirely based on quasiperiodic arrangements of layers where the role played by the A and B layers is, respectively, interchanged. In that case the characteristic long-range quasiperiodic order is preserved under transformations involving the conjugation operation $n_A \leftrightarrow n_B$. This invariance has interesting physical implications which can be exploited in the design of optical devices. In the inset of figure 14 we sketch a multilayer containing two kinds of quasiperiodic modules. In the first one (labeled F), the A (B) layers are composed of low (high) refractive index materials. In the second one (labeled F^+), the values of the refractive indices assigned to the layers A and B are reversed, so that the total internal reflection angle condition is achieved when $x_0 \simeq 0.4$ ($\theta \simeq 40^\circ$). Consequently, the second module behaves as a perfect mirror for incidence angles verifying $x > x_0$. The key point here is the possibility of combining both kinds of modules in order to construct efficient optical microcavities by a judicious choice of the incidence angle geometry. In the upper panel of figure 14 the dependence of the transmittance with the incidence angle θ for the optical device just described is shown. Thus, by properly selecting the refraction indices of the layers materials, it would be possible to achieve broad multidirectional reflection devices based on quasiperiodic structures.

Inspired by these results the reflectance curve in Fibonacci/Fibonacci$^+$ multilayers (the symbol + here indicates the conjugation operation $n_A \leftrightarrow n_B$) based on porous silicon has been recently reported (figure 15) [103]. Good agreement between the experimental and theoretical reflectance spectrum is observed, except by a shift around $\lambda_0/\lambda = 1$, which increases as the wavelength decreases. This result is a consequence of deviations from the quarter wavelength condition due to the refractive index dispersion of porous silicon layers.

Depending on the parity of the generation order, the Thue–Morse sequence exhibits either conjugation or mirror

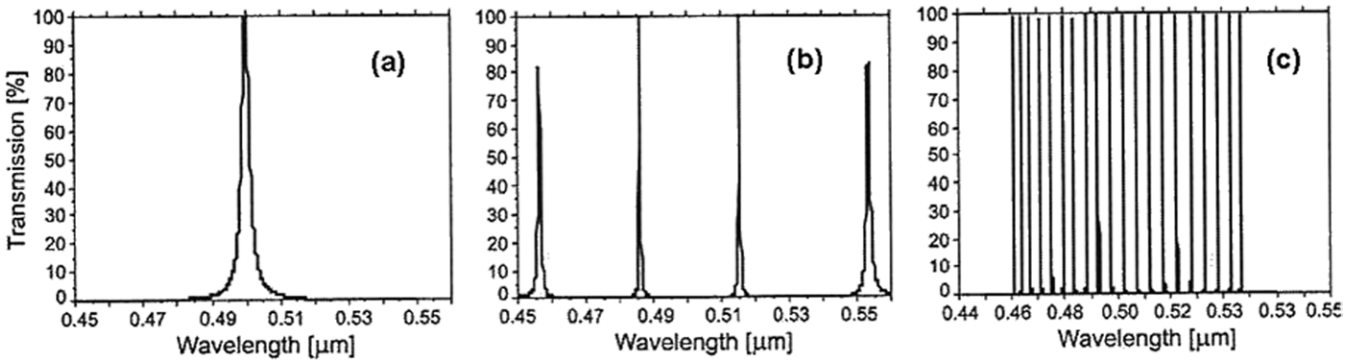

Figure 13. Transmission spectrum for the $A[BA]^4[ABBBBABBA]^l A[BA]^4$ structure for (*a*) $l = 0$, (*b*) $l = 2$ and (*c*) $l = 5$ [98, 99]. Reproduced with permission from [99]. (Courtesy of Yassine Bouazzi.)

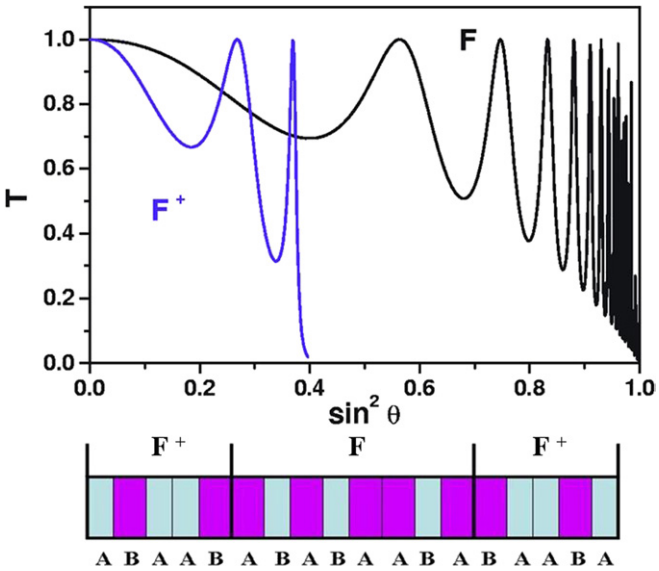

Figure 14. Dependence of the transmission coefficient with the incidence angle for the conjugated order device sketched in the lower panel, with $n_A = 1.46$ (SiO_2), $n_B = 2.35$ (TiO_2) (type F subunit) and $n_A = 2.35$ (TiO_2), $n_B = 1.46$ (SiO_2) (type F^+ subunit). Low panel: scheme of a conjugated order optical resonating microcavity based on three quasiperiodic subunits, where a FDM (with $N = 8$), showing high transmission, is encased between two Fibonacci multilayers (with $N = 5$), acting as optical mirrors. Dark (light) layers correspond to low (high) refractive index materials, respectively.

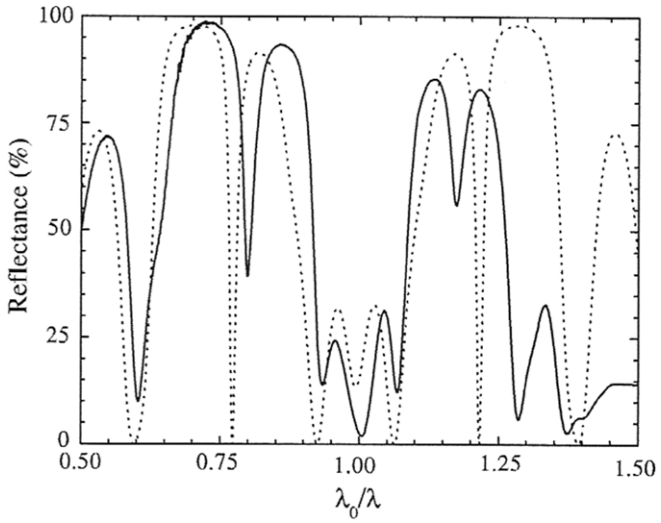

Figure 15. Experimental (solid line) and theoretical (dashed line) reflectance spectra at an incidence angle of 5° of a symmetric Fibonacci structure S_6/S_6^+ made of porous silicon. $\lambda_0 = 600$ nm [103]. (Courtesy of Gerardo G Naumis.)

symmetries by construction, whereas other substitutional sequences considered so far, like the Fibonacci, period-doubling or Rudin–Shapiro ones, lack these symmetries. Nevertheless, one can intentionally design related systems exhibiting mirror symmetry by

(i) reversing the order of the letters in the original sequence (i.e. $ABAAB \rightarrow BAABA$) and
(ii) concatenating the original sequence to the reversed one to obtain the string of letters $ABAAB|BAABA$ [75].

Alternatively, aperiodic sequences with mirror symmetry can be obtained by making use of their respective substitution rules in terms of the iterative formula $S_{j+1} = S_{j-1}S_jS_jS_{j-1}$. It is clear that the resulting sequence has mirror symmetry by construction. In doing so, the structure is endowed with a nested series of dimer-like positional correlations among the letters, starting from the mirror symmetry plane (i.e. $A\{B[A\{A[B/B]A\}A]B\}A$). This structural correlation enhances resonant transmission effects leading to the presence of additional PBGs in a given frequency interval (as compared with those present in an aperiodic multilayer of similar length without mirror symmetry) [104]. This interesting feature was used to manipulate the resonant transmission properties at specific wavelengths by designing and growing a symmetric Fibonacci/Fibonacci^{-1} multilayer (the symbol $^{-1}$ here indicates the letters reversal operation) based on TiO_2 and SiO_2 dielectric layers. The measured transmission spectra indicated the potential applications of this kind of aperiodic structure in multiwavelength narrow band filters and wavelength division multiplexing devices [105, 106]. On the other hand, the propagation of light waves in double-period multilayers with mirror symmetry has been numerically studied by considering sequences of the form $S_j = S_jS_j^{-1}$. The obtained results suggest that the main effect of introducing mirror symmetry is to enhance the number of self-similar features in the transmission spectra [104].

In summary, by making use of certain formal operations (letter conjugation, letter reversal), followed by concatenation of the obtained sequences (regarded as structural building blocks), one can exploit additional symmetries in the resulting aperiodic structures. The combination of these systems as well as with periodic ones, would result in a next generation of structurally complex systems based on aperiodic orderings.

2.2.3. Distorted quasiperiodicity. Another possible way to construct structurally complex systems out of quasiperiodic ones relies on the projection of a given quasiperiodic lattice in order to obtain a *distorted quasiperiodic* structure. In doing so, one introduces additional design parameters in the projected structure, which are directly related to the adopted projection rule, of the form $y(x, \xi_\nu)$, where ξ_ν are suitable parameters. This approach was originally introduced to obtain a broad omnidirectional reflection band in multilayers based on the Fibonacci sequence. To this end, the power law $y = x^{1+\xi}$ was used, where ξ measures the distortion degree introduced to the original Fibonacci multilayer [107]. In this way, the thickness of each layer in the deformed Fibonacci system becomes variable and depends on the sequential order i of the considered layer and the deformation degree according to the expression

$$d_i' = d[i^{\xi+1} - (i-1)^{\xi+1}], \qquad i \geqslant 1 \tag{21}$$

where d is the thickness of the considered layer in the original Fibonacci sequence. In the particular case of a dielectric multilayer the change in the layer thickness is accompanied by a change in its related optical thickness. This originates a modification of the optical properties in the multilayer which can be precisely controlled in terms of the projection parameter ξ. It is clear that this procedure can be immediately generalized to any arbitrary sequence in order to obtain distorted Thue–Morse, Rudin–Shapiro, or period-doubling sequences as well as distorted hybrid order structures obtained from them. On the other hand, for a given aperiodic sequence, one can properly vary the projection rule to tailor the resulting distorted structure at will. The potential of this approach to design useful orderings in multilayered devices is certainly remarkable. For instance, the optical properties of a distorted hybrid structure based on a fourth generation Fibonacci/third generation Cantor multilayer were numerically investigated. By applying the modification rule given by (21) it was possible to obtain omnidirectional mirrors covering all optical telecommunication wavelengths centered upon 0.85, 1.3 and 1.55 μm, for different incidence angles for both s-polarized light and p-polarized light [95].

Another appealing way of distorting periodicity in FDMs consists of replacing each B layer in the original Fibonacci sequence by a BB double layer instead (in practice it will suffice to duplicate the B layer thickness, i.e. $d_B \rightarrow 2d_B$). As is well known, the presence of BB dimers is forbidden in the standard Fibonacci sequence by construction, so that these BB layers can be regarded as a sort of local defect, thereby distorting the characteristic long-range periodic order of the resulting multilayer. Physically, the presence of BB dimers gives rise to the presence of new, specific resonant frequencies which are naturally absent in the unperturbed FDM structure. Accordingly, one may think of generating a quasiperiodic-periodic structural transition by successively encasing longer and longer strings of the form $BBBB\ldots$ in the place originally occupied by B layers. To the best of my knowledge, this kind of structure has not been thoroughly analyzed in the optics field yet. Quite interestingly, recent studies of 'dimer' Fibonacci semiconductor superlattices (obtained from the replacement $B \rightarrow BB$ in the corresponding quantum-wells) indicate that the dimer-related states play a significant role in the resulting electronic properties, enhancing the formation of relatively broad minibands with a concomitant disappearance of the critical localized states usually present in Fibonacci systems [108].

2.3. Some potential applications

2.3.1. Omnidirectional mirrors and optical filters. Mirrors based on alternating stacks of dielectric layers have very broad applications in photonics and optoelectronic technology. Usually these mirrors are fabricated by sequentially depositing layers of two different materials with significantly different refractive indices. By changing the number of layers, the layer thicknesses and the adopted sequence of layer deposition, the value of the reflectivity and the reflection wavelength band can be accurately and precisely controlled. In this way, mirrors with high reflectivity values and reflection windows ranging from a few nanometres to hundreds of nanometers in width can be achieved.

A more powerful design is aimed at achieving so-called omnidirectional reflectors, namely mirrors able to reflect light at any polarization, any incidence angle, and over a wide range of wavelengths. In fact, under proper conditions, 1D periodic multilayers can reflect light from all incidence angles and any polarization [109]. However, even when these special conditions are properly fulfilled, only one complete PBG exists in a period of the reciprocal space for periodic multilayers. This limitation does not apply to aperiodic multilayers possessing a much more complex structure in reciprocal space. Thus, the presence of PBG scaling, similar to that previously observed in Fibonacci multilayers [62], along with the presence of an omnidirectional PBG, has been experimentally confirmed for multilayers based on the stacking of either Si/SiO_2 [70], or TiO_2/SiO_2 layers [110], according to the Thue–Morse sequence. The physical origin of several fundamental PBGs in structures with different Fourier measures but sharing the self-similar property can be properly attributed to the presence of short-range correlations among certain basic building blocks interspersed through the whole multilayer. As a consequence, the number of frequency regions able to develop a full-fledged omnidirectional PBG progressively increases by properly tuning the refractive index contrast, as illustrated in figure 16 [110].

Reviewing the existing literature, one realizes that it is very difficult to make periodic sequence-based mirrors with *multiple* reflection windows having similar high values of reflectivity over a broad wavelength region, for example

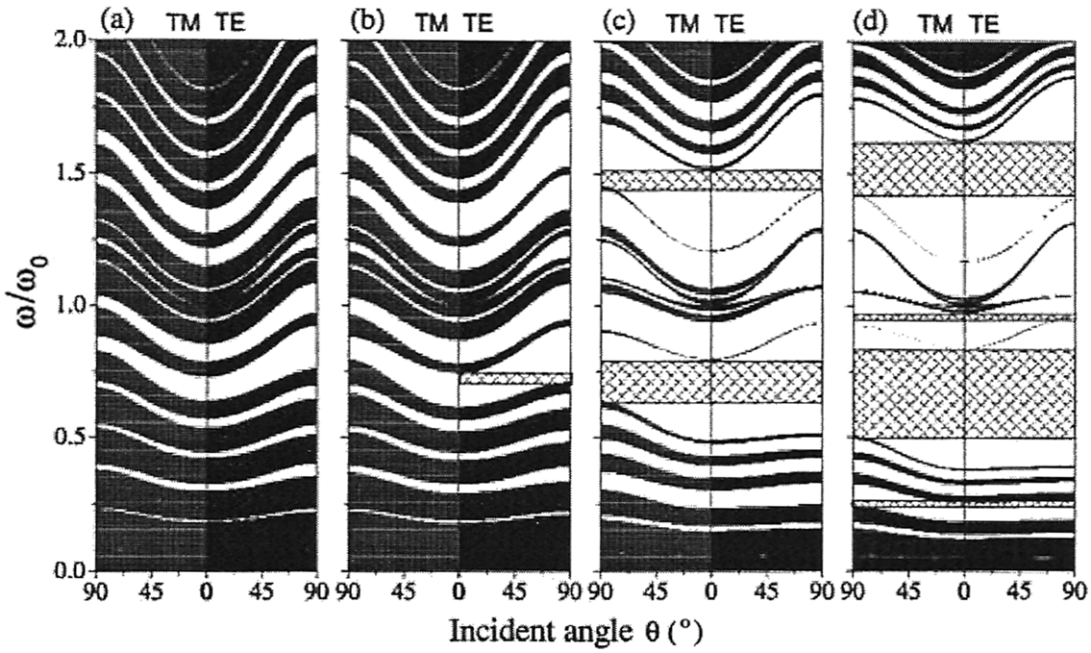

Figure 16. Calculated PBG structures for Thue–Morse dielectric multilayers containing $N = 32$ layers, with $n_A = 1.47$ and different values of the ratio $r \equiv n_B/n_A$. (*a*) $r = 1.4$, (*b*) $r = 1.6$, (*c*) $r = 3.2$ and (*d*) $r = 6.0$. The omnidirectional PBG is marked as a gridded rectangle [110]. (Courtesy of Rue Wen Peng.)

covering the entire visible region from 400 to 700 nm. Within this context, a useful concept for mirror design based on the Fibonacci sequence has been recently proposed in order to obtain tens or even hundreds of narrow, comparably high reflectivity windows over a very broad spectral region [111]. The proposed design is based on the sequencing rule $\mathcal{F}_j = S_0S_1S_2...S_j$, that is, the jth-order structure is obtained from the continued concatenation of all the Fibonacci approximants from $S_0 = B$ up to S_j, where each Fibonacci approximant, in turn, is obtained making use of the usual concatenation rule $S_j = S_{j-2}S_{j-1}$ (alternatively, $S_j = S_{j-1}S_{j-2}$) with $S_0 = B$ and $S_1 = A$. The total number of layers is then given by $N = F_{j+1} - 1$. Similarly dense reflectivity spectra were reported for dielectric multilayers based on Fibonacci-class sequences. On this basis, a systematic procedure aimed at designing a dispersion compensator for long distance optical fiber transmission lines was proposed [80].

2.3.2. Number recognition. Propagation of electromagnetic waves in aperiodic multilayers can be usefully exploited for number recognition and data storage purposes [30]. To this end, one should consider a multilayer composed of K different types of materials as a number written in base K. Thus, layered structures built of two different substances will correspond to binary numbers, where layers with low (high) refraction index are labeled with symbol '0' ('1'), respectively (figure 17). For instance, periodic multilayers consisting of alternating high-low-refraction indices of the form 10, 1010, 101010, ... correspond to decimal numbers 2, 10, 42,..., respectively. The key point of this approach is that, due to multiple scattering and interference effects, the propagation of an electromagnetic wave through the multilayer results in the formation of a characteristic transmission (or reflection) pattern, which could be properly used to identify the number associated with each multilayer. Due to the sensitivity of interference processes to minor modifications in the arrangement of the layers this method allows for an efficient detection of possible errors in the layer distribution in a non-invasive way. This property could be used in optical data recording and read-out, though it is clear that not only the identification of certain specific numbers (i.e. those related to a given substitution sequence) but also the possibility to code and identify any given number is necessary for information coding. In this regard, the very possibility of performing operations with numbers using wave propagation through multilayer based Fabry–Perot interferometers was illustrated [30, 31]. In the same vein, a systematic analysis of progressive sequential splitting of some peaks in the spectral portraits of Cantor dielectric multilayers revealed a direct correlation between their associated number value and their prime factors [31, 32].

As we have mentioned in section 1.2, a characteristic feature of the transmission spectra of Cantor dielectric multilayers is their scalability. A similar property has also been reported for the spectral transmission properties of a multilayer structure in which the refractive index of the layers follows a self-similar arithmetical sequence named 'the 1s-counting sequence', which is related to Pascal's triangle. This sequence is defined by counting the number of '1's in the binary representation of natural numbers, namely $0 = \mathbf{0}$, $1 = \mathbf{1}$, $2 = \mathbf{10}$, $3 = \mathbf{11}$, $4 = \mathbf{100}$, $5 = \mathbf{101}$, $6 = \mathbf{110}$, $7 = \mathbf{111}$, etc. Counting the number of '$\mathbf{1}$'s in each representation we obtain the sequence $A_j = \{0, 1, 1, 2, 1, 2, 2, 3...\}$. Quite conveniently, this series can also be generated following the recursive formula $A_j = \{A_{j-1}, 1 + A_{j-1}\}$, with $A_0 = 0$ as the initial value. The self-similarity property of the sequence can be grasped by decimating every second term in a sequence of

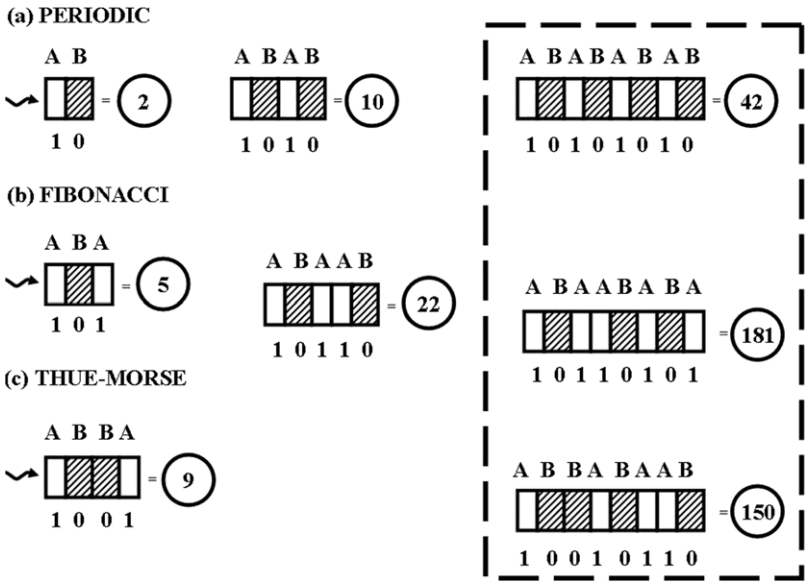

Figure 17. Sketch illustrating the different code number capabilities of different dielectric multilayers depending on the type of order (periodic, Fibonacci sequence or Thue–Morse sequence) in the arrangement of their layers. We note (dashed box on the right) that depending on the stacking order (which determines the binary representation of the refraction index profile) three multilayers with the same number of layers ($N = 8$) will code for three different decimal numbers values.

order j, which leads to the corresponding $j-1$ order sequence, as is illustrated below

$$A_4 = \{0, 1, 1, 2, 1, 2, 2, 3, 1, 2, 2, 3, 2, 3, 3, 4\} \rightarrow \{0, , 1, , 1, , 2, , 1, , 2, , 2, , 3\}. \quad (22)$$

On the basis of this numerical sequence one can construct a dielectric multilayer composed of $N = 2^j$ layers, each one having a refractive index given by

$$n_l = n_* + \epsilon\{A_l\}, \qquad l = 1, ..., N \quad (23)$$

where n_* is a suitable initial reference value and ϵ is a small increment [112].

In figure 18 the refractive index profile determined from (23) is compared with those corresponding to both periodic and random refractive index distributions for multilayers of the same length. The resulting transmittance under normal incidence geometry at quarter-wave condition is shown in figure 19. As we can see, the number of null transmission gaps is reduced in the aperiodic multilayer, compared with the periodic one. This is due to the *absence* of long-range quasiperiodic order in the considered A_j sequence. Nevertheless, the transmittance of the aperiodic multilayer exhibits exact scalability, since the transmittance spectra of smaller structures is contained in the spectrum of the larger one after a proper scaling by a power of two factor.

2.3.3. Thermal emission control. The multilayered structures considered up to now are made of lossless, linear optical materials. Some interesting results are obtained when one considers more realistic materials, able to couple with the electromagnetic field. For instance, one may consider the optical properties of multilayered structures containing aperiodically arranged optically *anisotropic* constituent materials [113, 114], or simply consider that some of the layers are able to absorb a fraction of the incident radiation. Now, even in the case of highly absorptive materials, not all incident radiation is usually absorbed by a given material. This is because the material reflects some radiation at its surface. Therefore, most absorbing materials behave as the so-called graybody when heated, exhibiting emittance values lower than unity.

An ingenious way to circumvent this shortcoming, enhancing the thermal emissivity of a given material above that corresponding to its graybody value *at certain* frequencies, was proposed on the basis of the structural design depicted in figure 20. In fact, it has been observed that quantum confinement effects modify the spontaneous emission processes in PBG multilayered structures. Accordingly, one should expect a modification of the thermal radiation in such systems. A convenient way to deal with this problem within the framework of the transfer matrix technique relies on the evaluation of the so-called thermal optical power

$$\mathcal{E}(\omega) = 1 - R(\omega) - T(\omega), \quad (24)$$

where $R(\omega)$ and $T(\omega)$ are the reflectance and transmittance, respectively. Equation (24) is physically interpreted as the ratio of the optical power emitted at frequency ω into a spherical angle element $d\Omega$ by a unit surface area of the thin film, to the power emitted by a blackbody with the same area at the same temperature. In this way, the power spectrum of the heated multilayered system located in front of an emitting hot surface (figure 20) is given by the expression [115, 116]

$$\mathcal{P}'(\omega, T) = \mathcal{E}(\omega)\mathcal{P}(\omega, T), \quad (25)$$

where

$$\mathcal{P}(\omega, T) = \frac{\hbar\omega^3}{2\pi^2 c^2} \frac{1}{e^{\frac{\hbar\omega}{k_B T}} - 1}. \quad (26)$$

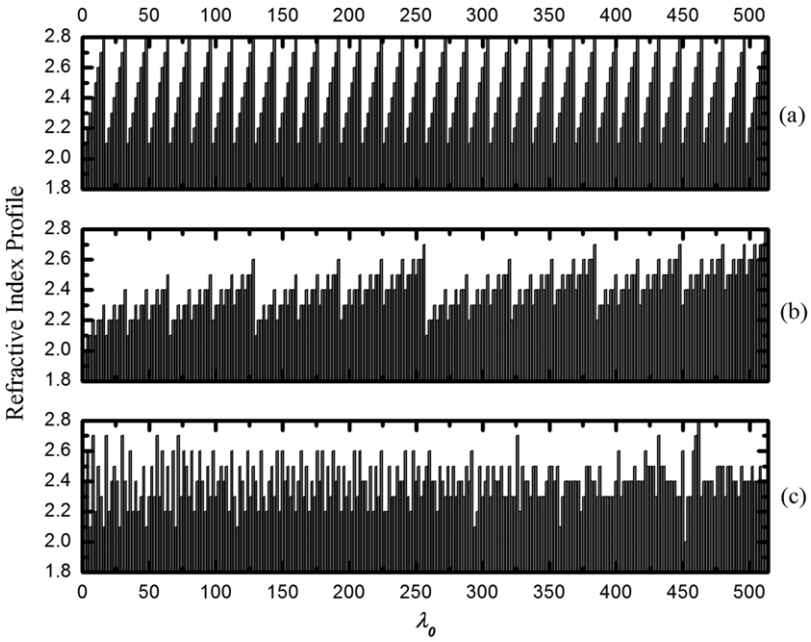

Figure 18. Refractive index profile as a function of the optical thickness for structures with $N = 256$ layers in air. (a) Periodic structure formed with 32 cells, each one having 8 slabs with refractive index ranging from values 2.1 to 2.8, respectively. (b) Aperiodic structure with a refractive index profile given by (23) with $n_* = 2.0$ and $\epsilon = 0.1$. (c) Random structure [112]. (Courtesy of X I Saldaña.)

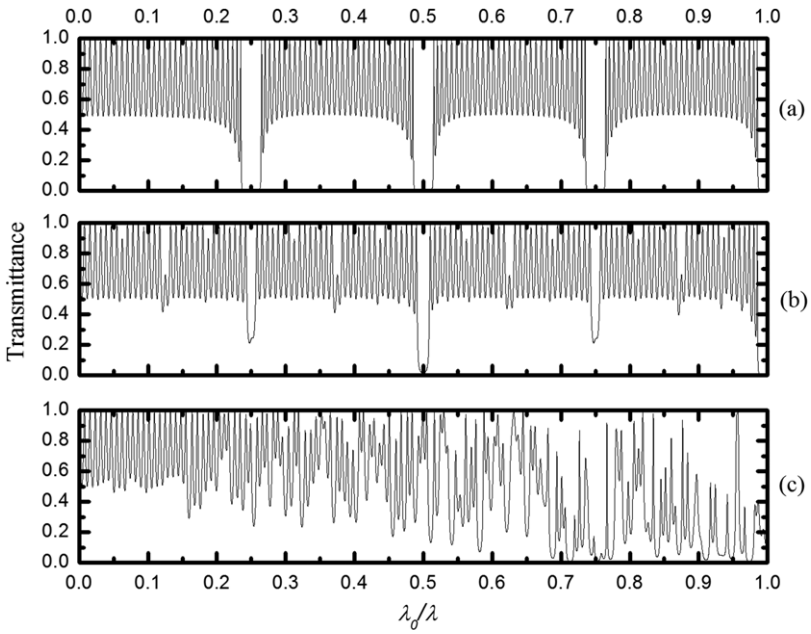

Figure 19. Transmission spectrum for the structures whose refractive index profiles are shown in figure 18 [112]. (Courtesy of X I Saldaña.)

is the well-known Planck's law. Some illustrative results are shown in figure 21.

Let us first consider the case where a periodic film coating sits atop the heated substrate (figure 21(a)). As we see, the film significantly blocks heat radiation emitted by the substrate at the frequencies corresponding to the photonic crystal bandgap ($\omega/\omega_0 = 1$) as expected, but we also observe that the substrate's emission is enhanced from the gray-body level all the way up to the perfect blackbody rate at a number of frequencies corresponding to the pass-band transmission resonances of the multilayered film. This occurs because the thin film acts as an antireflective coating at these resonances. In this way, all the radiation incident from the left tunnels through the multilayer structure into the substrate for these selected frequencies, so that the substrate effectively behaves as a perfectly absorbing blackbody in that case [116]. A similar enhancement of the substrate's thermal emittance at certain resonance frequencies accompanied by the corresponding inhibition at the stop-bands is observed in the aperiodically arranged thin film coatings as well. In the case of the Fibonacci coating (figure 21(b)) a characteristic trifurcation splitting can be clearly appreciated around a number of frequencies, and one finds a strong emittance within the spectral range corresponding to the midgap in the periodic case. In fact,

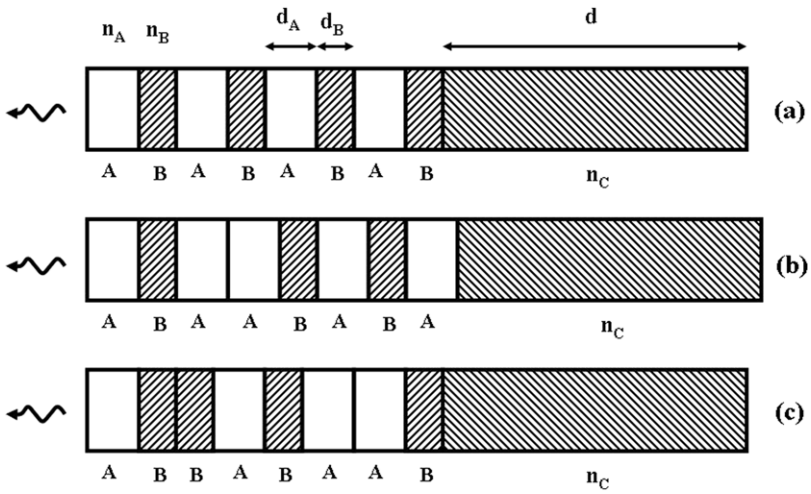

Figure 20. A multilayered stack (thin film) made of alternating layers of refractive indices n_A (real) and n_B (complex) coats a thick absorbing substrate of refraction index n_C. The entire structure is embedded in a medium, taken to be air ($n = 1$). Different working regimes are obtained depending on the adopted absorber distribution (shadowed layers). In (a) the absorber layers are periodically distributed, whereas in (b) and (c) they are, respectively, arranged according to the Fibonacci and Thue–Morse sequences.

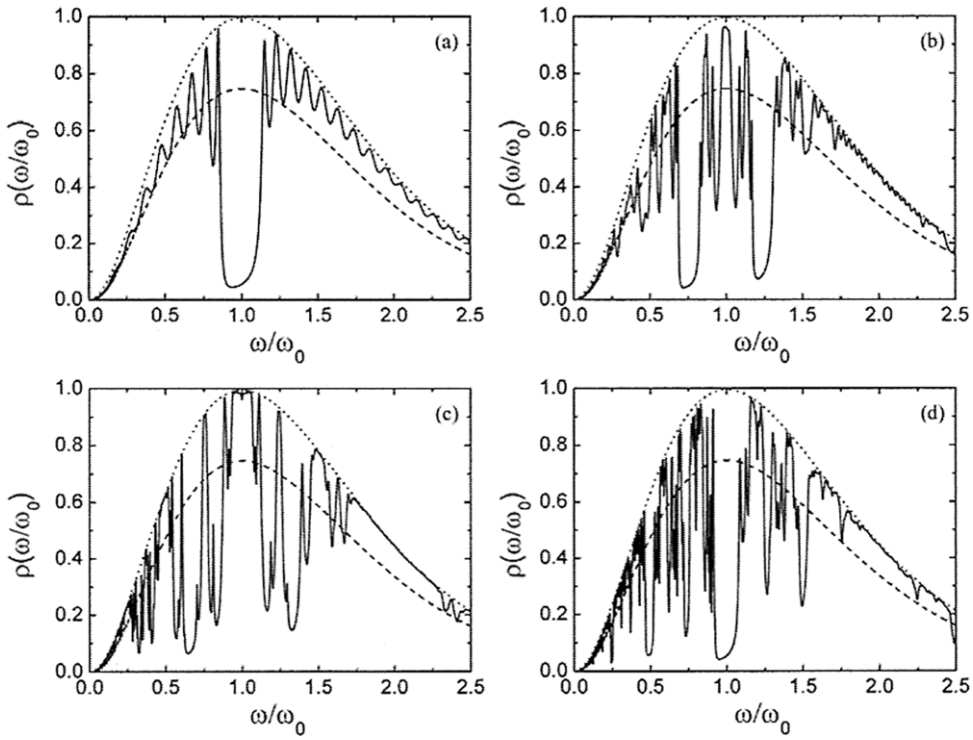

Figure 21. Thermal radiation spectra as a function of the reduced frequency under normal incidence conditions for the devices shown in figure 20 with $n_A = 1.45$ (SiO_2) and $n_B = 1.0 + 0.01$i, where the thin film coat layers are, respectively, arranged according to the following sequences: (a) periodic, (b) Fibonacci ($N = 377$), (c) Thue–Morse ($N = 512$) and (d) period-doubling ($N = 512$). The perfect blackbody thermal spectrum is given by the dotted curve, whereas the dashed curve gives the thermal spectrum of the substrate, with refractive index $n_C = 3 + 0.03$i. The temperature is chosen so that the blackbody (Wien) peak is aligned with the midgap frequency $\omega_0 = 2\pi c/\lambda_0$ ($\lambda_0 = 700$ nm). All the curves are properly normalized by this peak power. (From [117]. Courtesy of Eudenilson L Albuquerque.)

the presence of allowed bands in certain forbidden regions of the periodic system is a characteristic feature of quasiperiodic systems [16]. An analogous pattern is observed in the thermal spectrum corresponding to the Thue–Morse thin film, whereas that corresponding to the period-doubling sequence is more similar to the periodic one around the $\omega/\omega_0 = 1$ spectral range. In all the aperiodic arrangements, however, one has a richer thermal emission spectrum, reflecting in a conspicuous way the highly fragmented nature of their transmission profiles. Quite interestingly, these spiky thermal emission spectra can be substantially smoothed (hence obtaining broader spectral ranges with enhanced emittance) using metamaterials in the composition of the multilayer coat [117].

2.3.4. Layered metamaterials. Metamaterials are artificially constructed composites exhibiting a negative electrical

permittivity ϵ together with a negative magnetic permeability μ in the same frequency range. This yields a negative refractive index (i.e. $n = i^2\sqrt{|\epsilon|}\sqrt{|\mu|} = -\sqrt{\epsilon\mu}$). The main effect of having a negative refraction index is that the electric field $\boldsymbol{E}$, the magnetic field $\boldsymbol{H}$, and the wave vector $\boldsymbol{k}$, form a left-handed triplet. Due to that, these materials are also referred to as left-handed materials, because they support waves with the phase velocity opposite to the direction of the energy flow. Moreover, their phase and group velocity are antiparallel, since the group velocity usually has the same direction as the energy flow (Poynting vector) [118].

The study of photonic systems consisting of alternating layers of left-handed and right-handed materials has recently received a great deal of attention. Thus, it has been shown that multilayered structures made of alternating layers of metamaterials and ordinary dielectrics can exhibit new types of PBGs which are not based on interference effects. The first kind of so-called non-Bragg gap arises naturally when the volume average refractive index of the multilayer, $\bar{n}$, equals zero, so that the structure cannot support propagating waves [119]. The zero-$\bar{n}$ gap is rather robust and insensitive to both the light incidence angle and polarization effects, as compared with the ordinary Bragg gaps [120, 121]. The second kind of non-Bragg gaps appear in dispersive materials at frequencies where either $\mu(\omega)$ or $\epsilon(\omega)$ vanishes in the metamaterial. Unlike the zero-$\bar{n}$ gap, these gaps occur at frequencies where only a single constituent material of the multilayered structure shows zero refractive index. In addition, zero-μ and zero-ϵ gaps are polarization dependent, very robust against disorder, and they can interact with zero-$\bar{n}$ gaps, giving rise to new behaviors [122, 123].

The average refractive index for a periodic multilayer made of left-handed and right-handed alternating materials is given by

$$\bar{n} = \frac{n_A d_A + n_B d_B}{d_A + d_B}, \tag{27}$$

where the refractive index of the metamaterial will generally depend on the frequency. For instance, the following constitutive parameters have been adopted in a number of works [119, 124–126],

$$\epsilon(f) = 1 + \frac{5^2}{0.9^2 - f^2} + \frac{10^2}{11.5^2 - f^2},$$
$$\mu(f) = 1 + \frac{3^2}{0.902^2 - f^2}, \tag{28}$$

where f is the frequency in GHz. Therefore, the precise location of the zero-$\bar{n}$ gap can be finely tuned by properly choosing the optical parameters of the system. Now, from (27) we see that the zero-$\bar{n}$ gap central location is determined from the condition $n_A = -n_B\eta$, so that it does not depend on the system size. In the case of an aperiodic system, the average refractive index reads

$$\bar{n} = \frac{n_A d_A N_A + n_B d_B N_B}{d_A N_A + d_B N_B}, \tag{29}$$

where N_A (N_B) is the number of A (B) layers present in the multilayer. These numbers will in general depend on the generation order of the considered substitution rule, though some exceptions exist. For example, the average refraction indices for nth order Fibonacci and Thue–Morse multilayers are, respectively, given by [125, 126]

$$\bar{n}_F(n) = \frac{n_A d_A F_{n-1} + n_B d_B F_{n-2}}{d_A F_{n-1} + d_B F_{n-2}}, \quad \bar{n}_{TM} = \frac{n_A d_A + n_B d_B}{d_A + d_B}, \tag{30}$$

where we note that $\bar{n}_{TM}$ does not depend on the system size, since the number of A layers and B layers is the same in a Thue–Morse sequence of any order. Thus, the location of this gap in the Thue–Morse multilayer coincides with that present in the periodic sequence generated from the substitution rule $A \to AB$, $B \to AB$. Accordingly, for most aperiodic sequences we have an additional design parameter which is related to the N_A/N_B ratio. Since this ratio converges towards a certain limiting value as the generation order is progressively increased, the precise determination of the zero-$\bar{n}$ gap central location appears as a potential experimental way to accurately determine the quasiperiodic limit threshold of a given aperiodic multilayer. For instance, making use of the well-known relationship $\lim_{k\to\infty}(F_k/F_{k-1}) = \tau$ in (30) one obtains the zero-$\bar{n}$ gap condition $n_A = -n_B\eta\tau^{-1}$ for Fibonacci multilayers.

Thus, making use of the physical parameters given in figure 22, the zero-$\bar{n}$ gap of a Fibonacci multilayer is located at frequency $f_0 = 2.547$ GHz in the quasiperiodic limit. By inspecting figure 22 we realize that this gap readily develops from relatively low generation order values, and it is almost completely formed for generation orders higher than $n = 6$ (i.e. $N \geqslant 13$, which is a relatively small number of layers). The above frequency value was obtained by assuming the B layers are the usual positive index material. If we consider these layers are assigned to the metamaterial instead, one obtains the zero-$\bar{n}$ gap located at frequency $f_0 = 2.015$ GHz in the quasiperiodic limit (keeping all the remaining parameters the same) [124]. This frequency shift clearly indicates that the location of the zero-$\bar{n}$ gap in an FDM is not invariant under the conjugation operation $n_A \leftrightarrow n_B$, whereas it keeps the same values in the case of both periodic and Thue–Morse multilayers. Two interesting features can be drawn from figure 22, namely the following:

- Usual Bragg interference mechanisms in the high frequency region (labeled I) coexist with non-Bragg ones in the low-frequency region (labeled NB). In both cases, a highly fragmented energy spectrum is observed for generation orders higher than $k = 6$ (Fibonacci) and $k = 5$ (Thue–Morse).
- Although the generation orders are similar for both kinds of aperiodic multilayers, the number of layers corresponding to a given generation grows at different rates for Fibonacci (i.e. $N = F_k$) and Thue–Morse (i.e. $N = 2^k$) systems. Thus for $k = 5$ the Thue–Morse multilayer doubles the size of the Fibonacci one and for $k = 9$ the Thue–Morse multilayer is more than four times longer than the FDM. Accordingly, for a given generation order the energy spectra of Thue–Morse multilayers systematically display finer details.

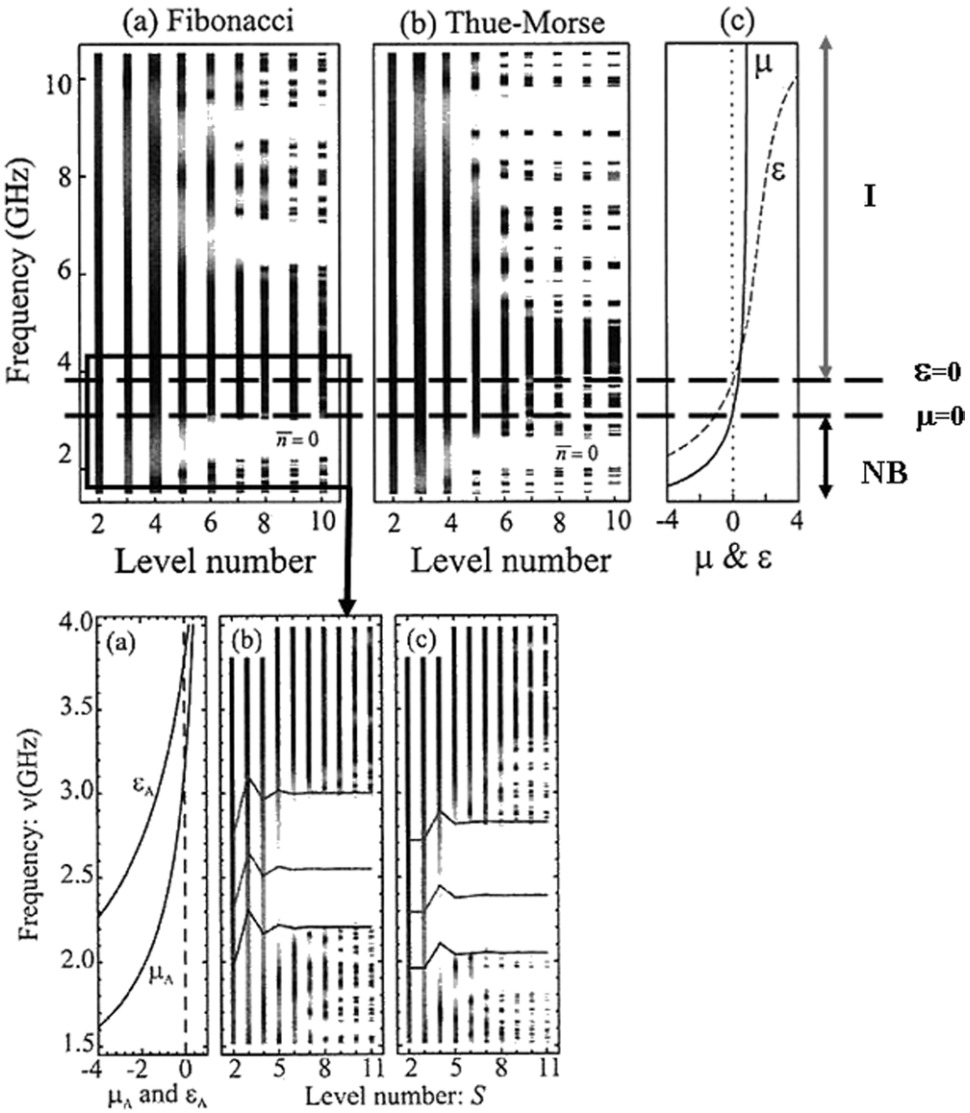

Figure 22. Upper panel: photonic spectra at normal incidence geometry for (*a*) Fibonacci and (*b*) Thue–Morse multilayers alternating right-handed and left-handed materials. In (*c*) the frequency dependence of the metamaterial *A* layers constitutive parameters given by (28) is plotted. Lower panel: (*a*) zoom of the frequency interval for which both $\epsilon < 0$ and $\mu < 0$. The lines indicate the zero-$\bar{n}$ gap center and band-edge locations as prescribed by (30) and (31), respectively, for (*b*) Fibonacci, and (*c*) Tribonacci aperiodic multilayers. The *B* layers are positive index materials with $\epsilon = \mu = 1$ (air). The widths of the metamaterial and air layers are $d_A = 6$ mm and $d_B = 12$ mm, respectively. The gray-code bar gives the reflection coefficient value, being $R = 1$ ($T = 0$) in the white regions and $R = 0$ ($T = 1$) in the black regions (Adapted from [82, 125]. Courtesy of Juan Antonio Monsoriu.)

It has been shown that the zero-$\bar{n}$ gap band edges are approximately described in terms of the following analytical expressions for both periodic and aperiodic multilayers [82],

$$\begin{aligned} \langle \mu \rangle = 0, \qquad & \left(\frac{\omega}{c}\right)^2 \langle \epsilon \rangle + k_\parallel^2 \left\langle \mu^{-1} \right\rangle \text{(TE)}, \\ \langle \epsilon \rangle = 0, \qquad & \left(\frac{\omega}{c}\right)^2 \langle \mu \rangle + k_\parallel^2 \left\langle \epsilon^{-1} \right\rangle \text{(TM)}, \end{aligned} \tag{31}$$

where $k_\parallel$ is the wave vector component along the layer plane for oblique propagation ($k_\parallel = 0$ at normal incidence) and $\langle \epsilon \rangle$, $\langle \mu \rangle$, $\left\langle \epsilon^{-1} \right\rangle$, and $\left\langle \mu^{-1} \right\rangle$ are volume averaged quantities. In the low panel of figure 22 the frequency interval around the zero-$\bar{n}$ gap is magnified in order to illustrate the applicability of (31) to both Fibonacci and Tribonacci (see section 2.1.1) quasiperiodic multilayers.

Studies on the dependence of the photonic spectra of aperiodic structures as a function of the incident angle for both TE and TM polarizations indicate that the $\epsilon = 0$ and $\mu = 0$ gaps are strongly polarization-selective, since the zero-μ gap appears for TE (but not for TM polarization), whereas the zero-ϵ gap appears for TM (but not for TE polarization). These polarization-selective gaps are more robust than the zero-$\bar{n}$ gap, appearing in the frequency spectra even for lower values of the generation order (figure 23) [125]. The existence of a full-fledged omnidirectional PBG in Fibonacci multilayers composed of alternating layers of right-handed and left-handed materials is mainly determined by the layers width ratio η so that the gap width attains a maximum for an optimum filling factor $d_A/(d_A + d_B)$ value, and closes if this filling factor is greater than a certain critical value [127].

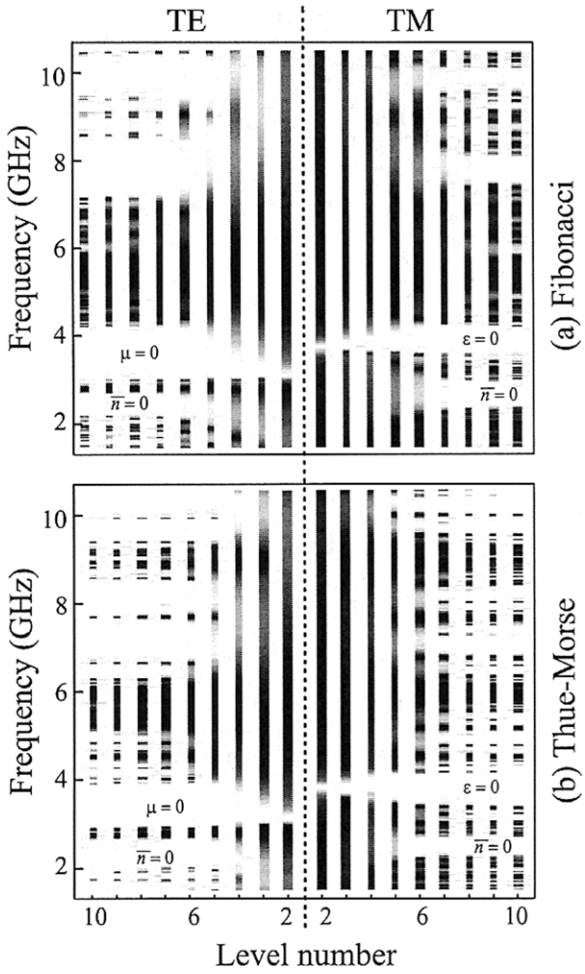

Figure 23. Photonic spectra for the (*a*) Fibonacci and (*b*) Thue–Morse multilayers at oblique incidence ($\theta = 45°$). The system parameters are the same as those indicated in figure 22. Reproduced with permission from [125]. (Courtesy of Juan Antonio Monsoriu.)

Omnidirectional PBGs have also been reported in Fibonacci multilayers containing both $\epsilon < 0$ (say, A layers) and $\mu < 0$ (say, B layers) so that this structure is entirely composed of metamaterials rather than a mixture of right-handed and left-handed materials [128]. In this case the PBG width in the quasiperiodic limit is given by $\Delta\omega = \omega_+ - \omega_-$, where ω_+ (ω_-) are determined from the condition $\langle\epsilon\rangle = 0$ ($\langle\mu\rangle = 0$), respectively, with

$$\langle\epsilon\rangle = \frac{\tau\epsilon_A(\omega) + \eta\epsilon_B}{\tau + \eta}, \qquad \langle\mu\rangle = \frac{\tau\mu_A + \eta\mu_B(\omega)}{\tau + \eta} \tag{32}$$

where $\epsilon_A(\omega) = \epsilon_a - (\omega_e/\omega)^2$, $\mu_B(\omega) = \mu_b - (\omega_p/\omega)^2$ and $\omega_{e(p)}$ are the electronic (magnetic) plasma frequencies. Making use of (32) one checks that the omnidirectional PBG is very sensitive to the adopted value of the design parameter η. Thus $\Delta\omega$ progressively decreases as η increases, vanishing when $\eta = \tau$, and hence progressively increasing as η is further increased [128].

The possibility of tailoring the thermal emittance of a substrate (see section 2.3.3) by coating it with a film composed of alternating negative and positive refraction index materials arranged according to a triadic Cantor set has been numerically analyzed as well [129]. The sequential splitting characteristic of self-similar Cantor sets gives rise to the presence of narrow emittance peaks located at the midgap frequency region. Thus, while a full reflection band appears in the emittance spectra of periodic multilayers, Cantor-type ones exhibit sharp and narrow resonances throughout the band, even for low generation numbers.

The optical properties of Fibonacci structures composed of alternating *chiral* and achiral isotropic layers have been recently studied. Isotropic chiral metamaterials are macroscopically continuous media composed of equivalent chiral objects that are uniformly distributed and randomly oriented [130]. Chiral objects are three-dimensional (3D) bodies that cannot be brought into congruence with their mirror image by translation and rotation operations. Self-similarity, scalability and sequential splitting of the spectra in quasiperiodic chiral photonic structures was first investigated [131], and subsequently the chirality influence on the critical modes localization was analyzed [132].

In summary, in this section we have analyzed the possibility of exploiting aperiodic order in devices based on aperiodic multilayered structures. As we have seen, in many instances the recourse to Fibonacci, Thue–Morse or fractal arrangements of layers improves the obtained response compared with that of periodic arrangements. One of the main lessons to be extracted from the different experimental realizations described in this section is that aperiodic order is able by itself to endow a previously existing device with novel properties, opening new avenues for innovative applications on the basis of well-known physical mechanisms. Such a feature has been illustrated in some detail in the case of resonant optical cavities, multiband filters, x-ray mirrors, thermal emissivity control and non-Bragg PBGs.

3. Optical devices in two dimensions

In the previous section we have discussed the way aperiodic order affects the physical properties of aperiodic multilayered systems in one dimension. In this section we will study aperiodically ordered two-dimensional (2D) structures. The general approach in the design of 2D aperiodic structures consists of two basic steps:

(i) one defines an aperiodic pattern in 2D, usually a lattice of points exhibiting long-range quasiperiodic order. To this end, there exist two main routes in turn. In section 3.1 we will consider the generalization of 1D substitution sequences to the 2D case, whereas in section 3.2 we will consider structures based on aperiodic tilings of a plane.

(ii) the previously obtained lattice points are decorated with appropriate optical nano-elements like metallic particles or dielectric cylinders located at the vertices or centers of the tiles. Alternatively, one can decorate the lattice points by etching a pattern of air holes in a homogeneous dielectric slab.

This relatively simple procedure enables the fabrication of planar optical devices with varying light transport properties,

including different realizations of PQCs, which we will consider in section 3.3.

The optical response of 1D aperiodic multilayers was mainly analyzed in terms of two physical magnitudes: the reflectance/transmittance curve and the electrical field intensity profile along the multilayer growth direction. Thus, the existence of omnidirectional PBGs was properly described in terms of the transmission coefficient $T_N(\omega, \theta)$ for each polarization state. This mathematical function is not so useful in 2D and must be complemented by other physical magnitudes like the optical band structure diagram, the density of states (DOS), and the power radiation spectra. In fact, conclusions drawn for 1D structures cannot always be straightforwardly extended to higher dimensions. For instance, PBGs appear even for arbitrarily small refractive index contrasts in multilayers, whereas a relatively large contrast is required in 2D photonic crystals. In contrast, the physical interpretation of the electrical intensity spatial pattern can be readily extended from one to two dimensions.

To study the frequency response of aperiodic photonic structures and to identify the spectral position of their PBGs one can calculate the radiation power spectrum of a line source embedded in the structure by integrating the output energy flux through a closed contour L, according to the expression

$$\oint_L \boldsymbol{S}(\boldsymbol{r}) \cdot \boldsymbol{n}\, \mathrm{d}r, \tag{33}$$

where $\boldsymbol{S}$ is the Poynting vector, $\boldsymbol{r}$ is a 2D vector, and $\boldsymbol{n}$ is a unit vector normal to the contour, and divide it by the total flux without the sample. A band gap corresponds to a dip in the radiation power spectrum, which deepens as the sample size is increased. The spectral positions of low-frequency PBGs in nano-element-based photonic crystals largely depend on the resonant properties of the individual optical elements (Mie resonances). As a result, the low-frequency gaps observed in PQCs approximately coincide with the PBGs positions in their periodic counterparts with similar geometries and material compositions [133–135]. However, aperiodic structures also feature a number of additional optical modes originating from diffraction effects in the quasi-lattice high density planes [136], as well as multiple scattering resonances in self-similar local environments [137]. Both the number and the precise frequency values of these modes depend on the aperiodic lattice filling factor (i.e. the ratio of surface area covered by the optical elements to the total area of the photonic structure), which is in turn determined by the adopted geometrical parameters in the considered structure.

3.1. Inflation rules in two dimensions

The substitution sequences introduced in section 2.1.1 can be conveniently extended into two spatial dimensions. A simple method to achieve this goal is based on alternating the iterations of 1D substitution sequences along two *orthogonal* directions. For instance, a 2D Fibonacci lattice can be obtained from a seed letter A or B by applying two complementary Fibonacci sequence substitution rules $g_A : A \to AB,\ B \to A$ and $g_B : A \to B,\ B \to BA$ (depending on whether the *first* element encountered in the 2D letter expansion is A or B) along the horizontal (from left to right) and the vertical (up–down) directions, alternatively [138, 139]. For the sake of illustration, the first generations of this Fibonacci structure are shown below in matrix form

$$\begin{gathered} A \to AB \\ \begin{pmatrix} A & B \\ B & A \end{pmatrix} \to \begin{pmatrix} A & B & A \\ B & A & B \end{pmatrix} \\ \begin{pmatrix} A & B & A \\ B & A & B \\ A & B & A \end{pmatrix} \to \begin{pmatrix} A & B & A & A & B \\ B & A & B & B & A \\ A & B & A & A & B \end{pmatrix} \ldots . \end{gathered} \tag{34}$$

A generalization of the Thue–Morse substitution rule is somewhat simpler, since the same standard substitution rule $g : A \to AB,\ B \to BA$ can be applied irrespective of the character of the first letter encountered. In this way, starting from the seed letter A one obtains [138],

$$\begin{gathered} A \to AB \\ \begin{pmatrix} A & B \\ B & A \end{pmatrix} \to \begin{pmatrix} A & B & B & A \\ B & A & A & B \end{pmatrix} \to \begin{pmatrix} A & B & B & A \\ B & A & A & B \\ B & A & A & B \\ A & B & B & A \end{pmatrix} \ldots . \end{gathered} \tag{35}$$

The 2D extension of the Rudin–Shapiro lattice is obtained similarly, with the proviso that the inflation rule for this sequence now acts upon a two-letter combination instead of a one-letter one. In fact, in a two-letter alphabet, the Rudin–Shapiro sequence can be obtained by the iteration of the following substitution rule [140],

$$\begin{aligned} AA &\to AAAB, & AB &\to AABA \\ BA &\to BBAB, & BB &\to BBBA. \end{aligned}$$

As a result the inflation seed must be the 2×2 matrix [139],

$$\begin{pmatrix} B & A \\ A & B \end{pmatrix} \to \begin{pmatrix} B & B & A & B \\ A & A & B & A \end{pmatrix} \to \begin{pmatrix} B & B & A & B \\ B & B & A & B \\ A & A & B & A \\ B & B & A & B \end{pmatrix} \ldots . \tag{36}$$

An alternative way of obtaining the Thue–Morse lattice is based on the recursive rule given in the matrix form [141],

$$M_{k+1} = \begin{pmatrix} J_k - M_k & M_k \\ M_k & J_k - M_k \end{pmatrix}, \tag{37}$$

where J_k is a $2^k \times 2^k$ matrix in which each element is equal to one, and the initial matrices to start iteration are

$$M_1 = \begin{pmatrix} 1 & 0 \\ 0 & 1 \end{pmatrix}, \qquad J_1 = \begin{pmatrix} 1 & 1 \\ 1 & 1 \end{pmatrix}. \tag{38}$$

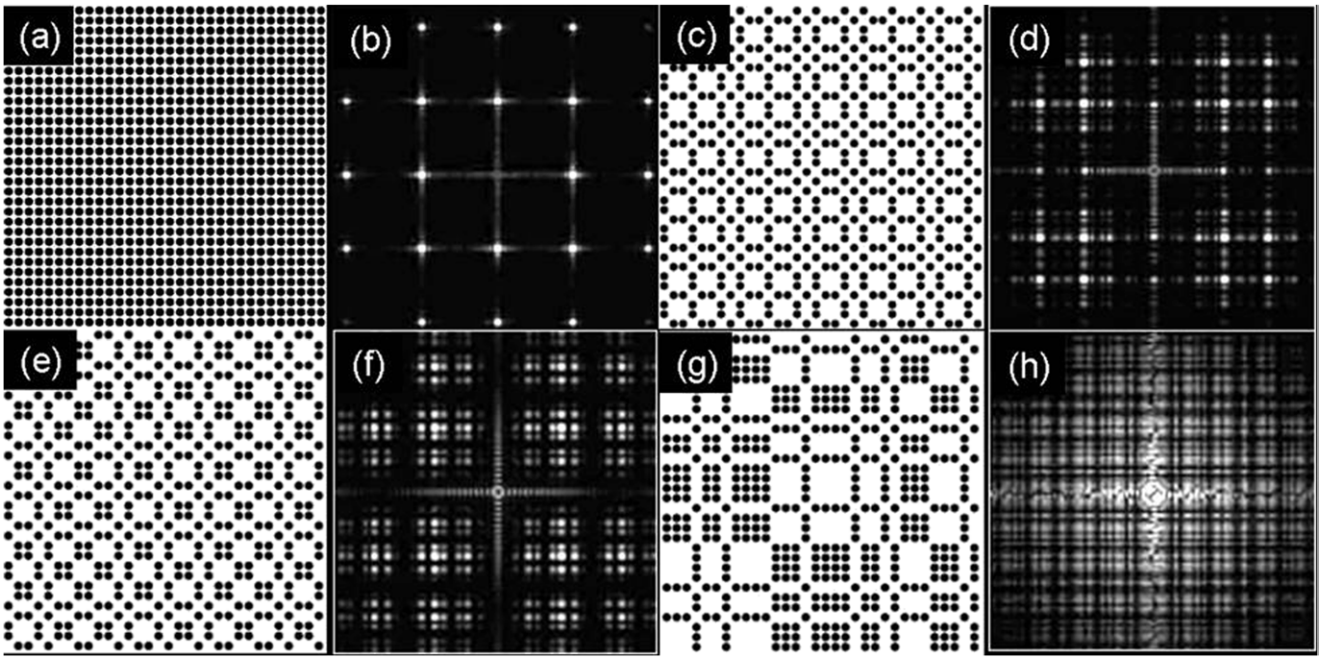

Figure 24. 2D periodic square (*a*) Fibonacci (*c*), Thue–Morse (*e*) and Rudin–Shapiro (*g*) aperiodic lattices obtained after seven iterations along with their Fourier spectra shown in (*b*), (*d*), (*f*) and (*h*), respectively [142]. (Courtesy of Luca Dal Negro.)

Making use of (38) into (37) one obtains

$$M_2 = \begin{pmatrix} 0 & 1 & 1 & 0 \\ 1 & 0 & 0 & 1 \\ 1 & 0 & 0 & 1 \\ 0 & 1 & 1 & 0 \end{pmatrix},$$

$$M_3 = \begin{pmatrix} 1 & 0 & 0 & 1 & 0 & 1 & 1 & 0 \\ 0 & 1 & 1 & 0 & 1 & 0 & 0 & 1 \\ 0 & 1 & 1 & 0 & 1 & 0 & 0 & 1 \\ 1 & 0 & 0 & 1 & 0 & 1 & 1 & 0 \\ 0 & 1 & 1 & 0 & 1 & 0 & 0 & 1 \\ 1 & 0 & 0 & 1 & 0 & 1 & 1 & 0 \\ 1 & 0 & 0 & 1 & 0 & 1 & 1 & 0 \\ 0 & 1 & 1 & 0 & 1 & 0 & 0 & 1 \end{pmatrix} \ldots . \tag{39}$$

It can be readily checked that the pattern of letters given by (35) is completely equivalent to the number patterns appearing in the matrix M_k given by (39) by simply identifying $A \rightarrow$ '0' and $B \rightarrow$ '1'. It is also easily verified that any row and any column of the symmetric M_k matrix containing 2^{2k} elements is a 1D Thue–Morse sequence of order k.

The direct and reciprocal spaces of the 2D aperiodic lattices obtained from (34)–(36) are shown in figure 24, which illustrates the extension of the characteristic Fourier properties of the corresponding 1D sequences to higher dimensions. In this way, aperiodically ordered optical devices allow one to study the effects of a purely measure-theory mathematical property on the propagation, confinement and localization properties of light. The Fourier spectrum of a fifth generation 2D Thue–Morse lattice grown according to (37) is shown in figure 25. The lowest band gaps ω_1 and ω_2 are related to the first Mie resonances of the cylinders, and their frequencies are practically independent of the periodic or aperiodic spatial arrangement of the cylinders. In contrast, the band gaps $\omega_3 - \omega_6$ are unambiguously explained as stemming from interference effects with the quasi-lattice high density planes [135].

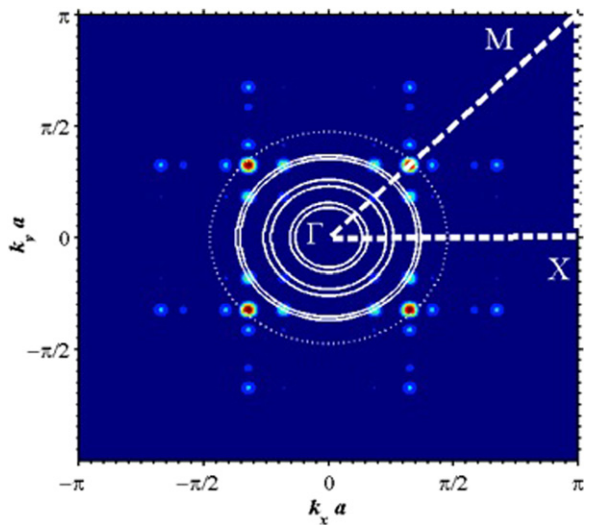

Figure 25. Fourier spectrum of the Thue–Morse lattice corresponding to M_5. The corresponding aperiodic photonic structure is obtained by placing identical dielectric cylinders located at the '0' sites in the 2D Thue–Morse lattice. The pillars are assumed to lie in a vacuum, with relative dielectric constant $\epsilon = 12.25$ (which corresponds to silicon in infrared spectrum) and radius $r = 0.35a$ (where a is the nearest-neighbor center-to-center separation). The solid line circles are given by the Bragg condition determining the band gap frequencies (ordered in increasing radial distances) $\omega_1 = 0.212$, $\omega_2 = 0.247$, $\omega_3 = 0.363$, $\omega_4 = 0.410$, $\omega_5 = 0.461$ and $\omega_6 = 0.557$ expressed in a/λ units. The dotted circle corresponds to the Bragg condition for the highest frequency band gap of a periodic square photonic crystal [135]. Reprinted with permission from [142]. Copyright 2010, American Institute of Physics.

The experimental realization of 2D aperiodic structures is a hard fabrication challenge. Notwithstanding this, several large area (up to 800 μm^2) 2D Thue–Morse lattices (up to

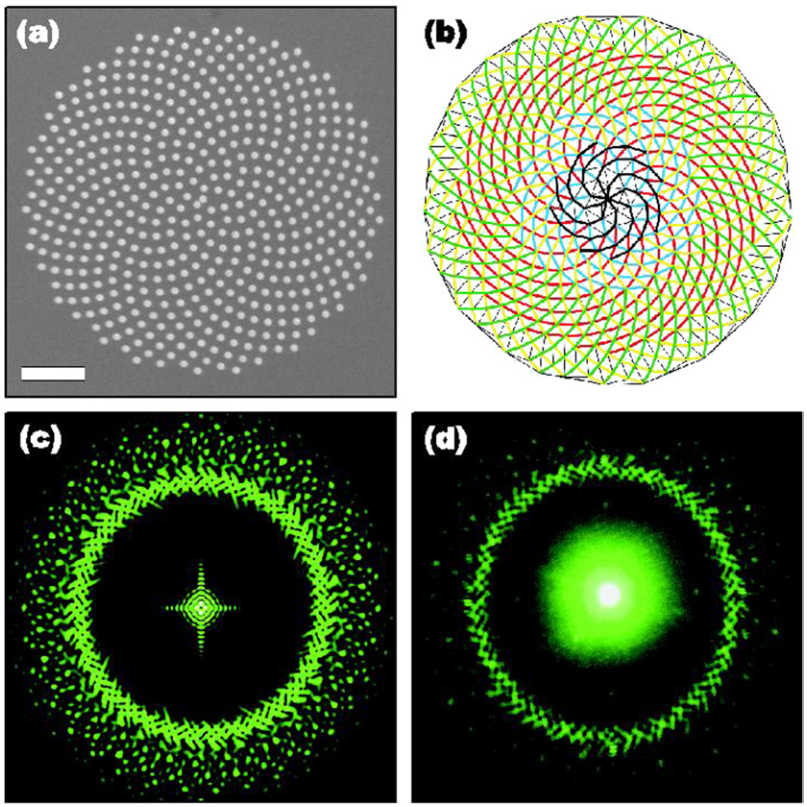

Figure 26. (*a*) Scanning electron microscope image of a sunflower fabricated by electron beam lithography containing 500 holes of radius $r = 0.539\ \mu$m. The pattern has a strong modal nearest-neighbor pitch $a = 2.2\ \mu$m derived from a Delaunay triangulation of the points set highlighting the so-called parastichies spiral curves (*b*). The number of parastichies in each rotational sense are consecutive numbers in the Fibonacci series. The calculated and experimental diffraction patterns are shown in (*c*) and (*d*), respectively [146]. (Courtesy of Michael E Pollard.)

$k = 10$ order) made of air rods ($n = 1, r = 100$ nm) embedded into polymethyl-methacrylate (PMMA, $n \sim 1.5$) have been recently fabricated with nanometric resolution (10 nm) by means of electron beam lithography techniques [143]. The obtained samples have been characterized by successfully comparing experimental far-field diffraction patterns with theoretical Fourier spectra corresponding to Thue–Morse patterns with lattice constants ranging from $a = 140$–1080 nm.

In addition to structures based on the extension of substitution sequences to higher dimensions, one can also consider 2D lattices derived from certain geometrical constructions. For instance, *spiral lattices* provide an interesting example of perfectly ordered systems where both translational and orientational symmetries are discarded. These lattices are based on the application of a simple mathematical algorithm. In the first place we consider a generating spiral curve, which can adopt any general form in polar coordinates, like $r = a\theta$ (Archimedean), $r = a\sqrt{\theta}$ (parabolic), or $r = ae^{\theta}$ (logarithmic). Then the spiral lattice is obtained by restricting r and θ according to a quantization condition of the form [144]

$$r = al^{\nu}, \theta = \phi_d l, l = 0, 1, 2..., \tag{40}$$

where ν is a real number, and ϕ_d measures the angle between adjacent radius vectors $r(l)$ and $r(l + 1)$. Adopting irrational values for ϕ_d we obtain lattices entirely lacking rotational symmetry. Accordingly, their Fourier transform does not show well-defined sharp spots, but diffuse rings similar to the diffraction patterns obtained for amorphous materials [145]. The spiral lattices generated in this way exhibit arrangements analogous to those observed in many botanical structures (the so-called Vogel's spirals, which describe the arrangement of florets in the sunflower head, are obtained when $\nu = 1/2$ in equation 40) and are characterized by self-similar inflation or deflation operations, like those observed in QC [7]. In figure 26(*a*) a 2D parabolic spiral lattice derived from the equation

$$x_n = A\sqrt{n}\cos n\Psi, \qquad y_n = A\sqrt{n}\sin n\Psi \tag{41}$$

is shown, where A is a scaling factor and $\Psi = 2\pi/\tau^2 \simeq 137.508^{\circ}$ is the so-called golden angle. In a recent work, planar arrays of Au nanoparticles arranged according to the three main types of Vogel's spirals ($\Psi = 2\pi/\tau^2$, $\Psi = 137.3^{\circ}$ and $\Psi = 137.6^{\circ}$) were fabricated by electron beam lithography on quartz substrates [147]. In this way, polarization-insensitive planar light diffraction in the visible spectral range was demonstrated as stemming from their almost circularly symmetric Fourier space.

3.2. Aperiodic tilings

The word tiling is generally used to describe a pattern or structure that comprises one or more polygonal shapes (tiles)

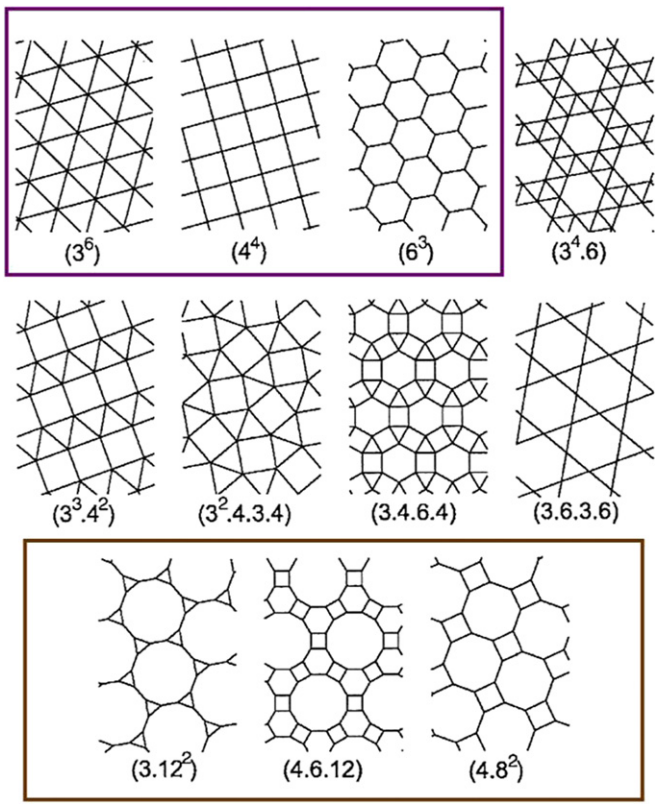

Figure 27. Archimedean tilings. A set of integers $(n_1.n_2.n_3.\ldots)$ denotes the vertex type in the way that n_1-gon, n_2-gon, n_3-gon,... different polygons consecutively meet on each vertex. For instance, the symbol $(3^2.4.3.4)$ represents a tiling in which two equilateral triangles, a square, an equilateral triangle, and a square successively gather edge-to-edge around any given vertex. The three first tilings shown at the top file, corresponding to the notation (3^6), (4^4) and (6^3), are composed of just one type of polygon tile and are usually referred to as Platonic tiles. The last three tilings at the bottom are of interest for structure analysis of quasicrystal approximants exhibiting octagonal and dodecagonal symmetries.

that pave a plane exactly, leaving no spaces between them. Squares, equilateral triangles and hexagons are particularly easy to tile with, in order to achieve a periodic pattern that repeats itself at regular intervals. The obtained patterns are endowed with the characteristic symmetries—threefold, fourfold, sixfold—of the tiles they are made up from. In the case of a regular pentagon tile, however, no matter how hard you try, they cannot be used to fill the entire plane and form a periodic tiling pattern: unfilled gaps will always remain. Certainly, one may relax the tiling rules by allowing for *different* types of polygons to be simultaneously used to construct the tile. If one imposes all the vertices to be of the same type at every joining point, only eleven types of tiling of the plane by regular polygons can be found, the so-called *Archimedean tiling* patterns shown in figure 27 (we note that the so-called regular or *Platonic tilings* are a subset of Archimedean ones).

A significant step forward toward more general tiling patterns consists in relaxing the periodicity condition as well. Thus, 2D *aperiodic tilings* are collections of polygons capable of covering a plane with neither gaps nor overlaps in such a way that the resulting overall pattern lacks any translational

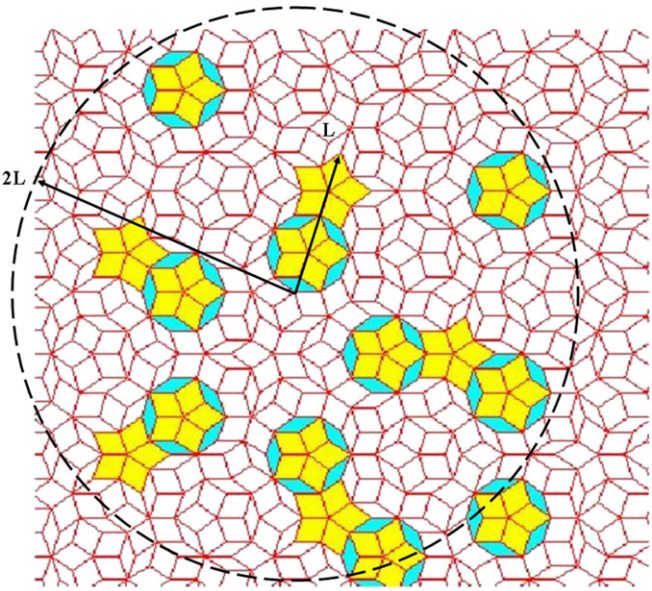

Figure 28. Penrose tiling illustrating the local isomorphism feature prescribed by Conway's theorem in two dimensions (compare it with the 1D case shown in figure 5).

symmetry. The *simpler* aperiodic tiling was discovered by Sir Roger Penrose in 1974 [148], and consists of just two different tiles: a flat (dark gray) and a thick (light gray) rhombus (figure 28). From the solid state physicist's viewpoint, the most relevant feature of Penrose construction is not the fact that it lacks translational symmetry, but that it possesses long-range quasiperiodic order, so that it is capable of producing sharp diffraction peaks [149]. Thus, the notion of repetitiveness, typical of periodic arrangements, should be replaced by that of local isomorphism, which expresses the occurrence of any bounded region of the tiling infinitely often across the whole tiling, irrespective of its size. In the particular case of Penrose tilings Conway's theorem states that given any local pattern having a certain characteristic length, L, several identical patterns can be found within a distance of $2L$ (figure 28) [35].

3.3. Photonic quasicrystals in two dimensions

One of the main differences between periodic photonic crystals and PQCs is that the latter lack translational symmetry, so that the notion of the Brillouin zone becomes ill-defined in this case. To overcome this shortcoming two approaches are usually considered. The first one relies on the notion of approximant unit-cell structure, which was previously introduced within the context of 1D multilayers in section 1.3. The second one directly considers a finite structure. From the modeling point of view, the second approach seems more appropriate to study actual physical realizations, which will always be finite, but it is constrained to the consideration of quite small systems due to computation limitations. The first approach is more convenient from both a fundamental point of view (since it allows for a systematic study of the quasiperiodic order threshold) and a practical viewpoint (since the related optical band structures can be derived in a standard way). Nonetheless, the artificial periodicity introduced in the supercell approximation may lead

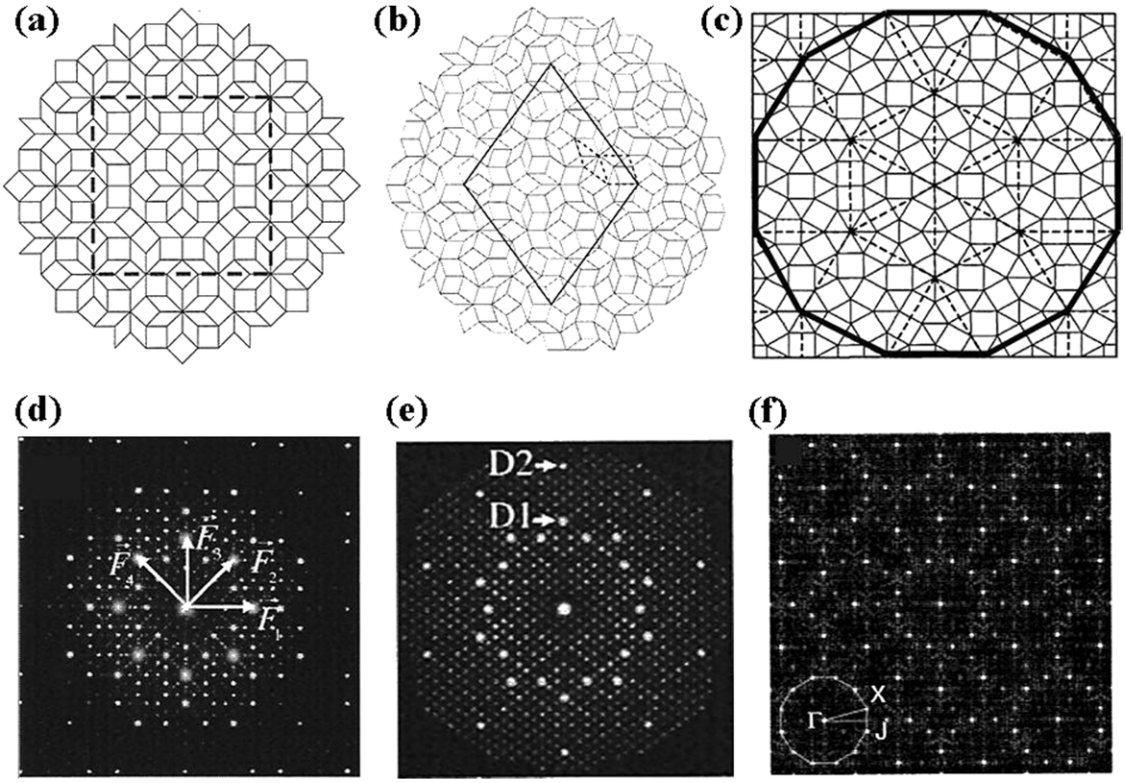

Figure 29. Portions of the (*a*) Ammann–Beenker, (*b*) regular Penrose and (*c*) Stampfli tilings along with their corresponding diffraction patterns exhibiting characteristic octagonal (*d*), decagonal (*e*) and dodecagonal (*f*) symmetries. Approximant unit cells considered in different works are highlighted by thick line polygons in the tiles (*a*), (*b*) and (*c*). The high-symmetry components of the Fourier spectra, responsible for the gap opening, are indicated by the arrows *F* and D1, D2, in (*d*) and (*e*), respectively. The Brillouin zone indicated by the white dodecagon at the bottom left of panel (*f*) corresponds to the unit cell highlighted in (*c*) with a thick line. (Adapted from [40](*a*), [151](*b*), (*e*), [152](*c*), [153](*d*) and [154](*f*).)

to some spurious results which must be carefully distilled from the intrinsic quasiperiodic features.

3.3.1. Quasiperiodic lattices. Three main representatives of quasiperiodic lattices have been considered in the literature, namely the *Ammann–Beenker* octagonal lattice (figure 29(*a*)), the regular *Penrose* lattice (figures 28 and 29(*b*)) and the *Stampfli* dodecagonal lattice (figure 29(*c*)). Other related tilings, such as the decagonal (figure 33) and dodecagonal Penrose lattices, have been also addressed in some works. All these tilings can be constructed from two unit tiles.

- The Ammann–Beenker lattice is formed by squares and 45° rhombi of equal edges a, leading to the presence of three relevant distances, $\sqrt{2}a > a > \sqrt{2-\sqrt{2}}a$, between different close vertices throughout the pattern. In turn, each vertex can be classified as belonging to six different possible environments (figure 33) according to their next-neighbors number (coordination index). The ratio of the frequencies of the square to the rhombus tiles in the infinite tiling is $1 : \sqrt{2}$, and that of the two mirror symmetrical rhombi is the same. The ratio of the areas of a square to a rhombus tile is $\sqrt{2}$, so that the total area of the tiling covered by squares equals that covered by rhombi.
- The Penrose tiling is formed by skinny (acute angle $\pi/5$) and fat (acute angle $2\pi/5$) rhombi with equal edge length a. Their frequency of appearance in the infinite tiling is $1 : \tau$ and their areas' ratio is τ. There exist eight different vertex configurations and five relevant distances, $\sqrt{1+\tau^2}a > \tau a > a > \sqrt{3-\tau}a > \sqrt{2-\tau}a$, between different close vertices.
- The Stampfli tile is formed by equilateral triangles and squares of length a. The ratio of squares to triangles is $\sqrt{3}/4$. There exist three different vertex configurations and two relevant distances, $\sqrt{2}a$ and a between close vertices [150].

3.3.2. Optical band structures. During the last few years a number of systematic numerical studies regarding the optical band diagram of periodic approximant structures in relation to their parent quasiperiodic lattices has been reported [136, 151, 155, 156]. It has been found that:

- Even the lowest order approximants can support quite *isotropic* PBGs (i.e. both the position and width of the predicted PBGs do not significantly depend on the light propagation direction in the plane) hence allowing for a more uniform light reflection (figure 30). This property stems from the fact that the first Brillouin zone has more symmetries in quasiperiodic lattices (figure 29) as compared with conventional photonic crystals based on periodic square or hexagonal lattices, hence favoring the

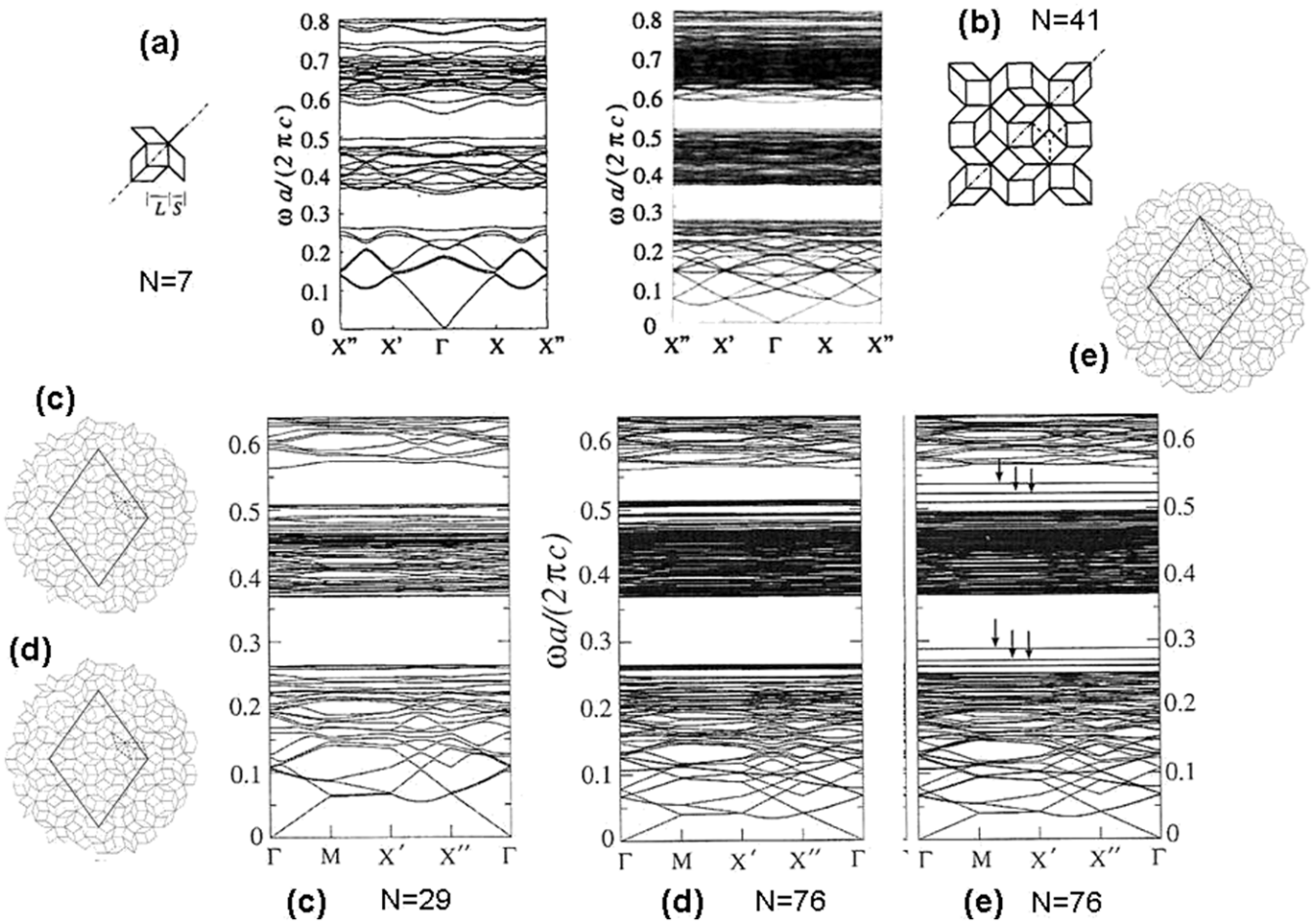

Figure 30. Optical band diagrams obtained for TM polarization for Amman-Beenker (*a*), (*b*), regular Penrose (*c*), (*d*) and decagonal Penrose (*e*) approximant lattices containing different number of vertices, N. Two main PBGs with midgap normalized frequencies ($\omega a/2\pi c$) at 0.32 and 0.55 and relative widths of about 30% and 15%, respectively, characterize the band diagram of all considered systems. (Adapted from [136, 151, 155].)

possible appearance of a complete gap in these systems. Although quite isotropic PBGs are also obtained for periodic structures displaying high order local rotational symmetries, like Archimedean tilings, the resulting PBGs are significantly narrower (gap-midgap ratios $\sim$ 0.05) and they appear at relatively higher frequency values ($a/\lambda \geqslant 0.6$) in this case [157, 158].

- The PBG widths depend on both the amplitude of the strongest Fourier components and their number. Since the Brillouin zone vectors responsible for the opening of the low-frequency PBGs are determined by common structure parameters for both the approximants and the quasiperiodic lattice, the quasiperiodic limit threshold is attained for relatively small order approximants (figure 29).
- Most bands are very flat, indicating that a significant reduction of the group velocity (within the range $0.005c - 0.02c$) occurs in all directions [133],
- PGBs in PQCs are, remarkably, almost independent of the angle of incidence of the incoming light [159].

To open a complete gap in 2D photonic crystals the refractive index needs to be larger than 2, which rules out the possibility of using polymer materials to fabricate periodic photonic crystals because their refractive indices are typically lower than 1.7. Compared with periodic photonic crystals, PQCs require a smaller refractive index threshold value to open a complete gap. For example, the threshold value is $n = 1.26$ for an octagonal quasilattice, which indicates that optoelectronic components based on PQCs may be obtained in low refractive index materials such as silica, glasses and polymers. Experimental evidence for complete bandgaps for both TE and TM polarizations has been reported for different setups, including octagonal arrangements of dielectric Ammann–Beenker cylinders in air or dodecagonal Stampfli tiles. In contrast to periodic lattices, the TM bandgap lies exactly in the middle of the TE bandgap, leading to an efficient overlapping for both polarization states in the resulting complete PBG. According to numerical simulations, this bandgap remains open for very low refraction index materials such as glass ($n = 1.45$) with similar filling fractions [154]. Motivated by this possibility, a high-quality octagonal PQC was fabricated using a laser-induced microexplosion method. The resulting structure consisted of air cylinders embedded in a polymer material dielectric matrix arranged according to the Ammann–Beenker pattern. The frequency spectrum

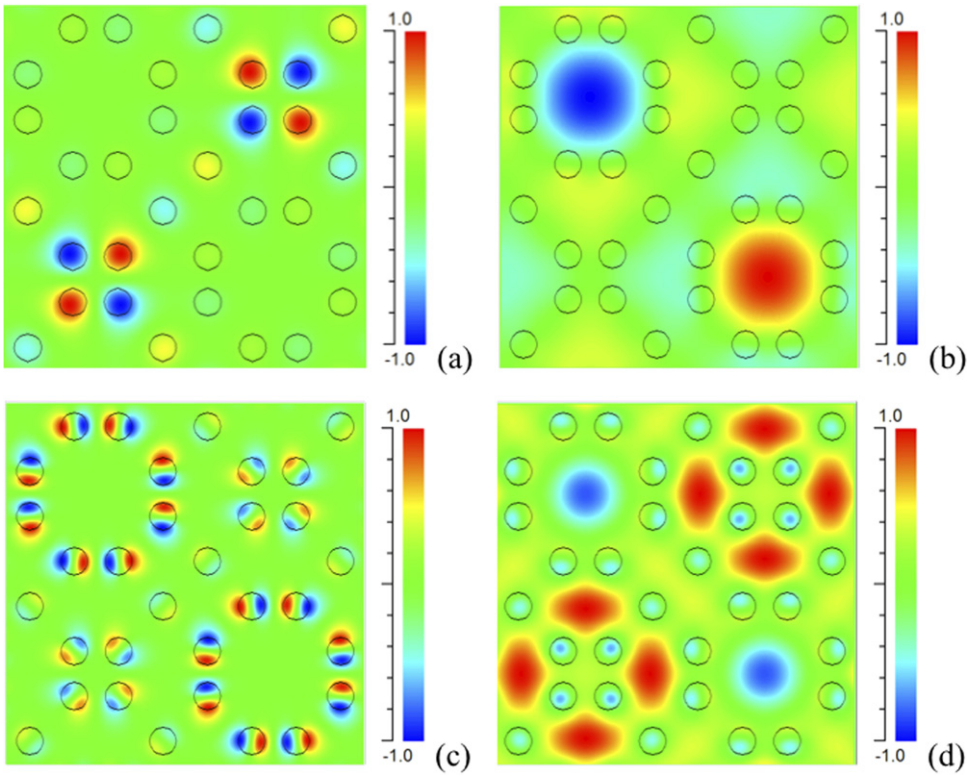

Figure 31. Comparison between the electric field patterns at the Γ point of a M_3 generation order Thue–Morse lattice (see section 3.1) containing $N = 64$ dielectric rods for two states located at the band edges (*a*), (*c*) and two states located near the center of the band gaps (*b*), (*d*). The modes shown in (*a*) and (*c*) are mainly concentrated on the high-dielectric regions and can be classified as monopole and dipole modes. On the other hand, the states shown in (*b*) and (*d*), which can be regarded as defect modes, are concentrated in the low-dielectric region [135]. (Courtesy of Luigi Moretti.)

exhibits a number of relatively broad gaps inside which TM mode propagation is forbidden [160].

3.3.3. Electric field patterns. Most band-edge states in 2D aperiodic systems are characterized by light wave patterns localized in square, hexagonal and octagonal high-symmetry local environments of the underlying tile. By comparing the electric field patterns shown in figures 31 and 32 we can see that the optical modes supported by the Rudin–Shapiro lattice are generally more localized than those in the Thue–Morse lattices, which agrees with the absolutely continuous nature of the Rudin–Shapiro's Fourier spectrum. Consistently, an increase in the structure size does not have a significant effect on the localization properties of the Rudin–Shapiro modes, which are also characterized by higher values of the resonance Q-factors (narrower mode line-widths) as compared with those obtained for Thue–Morse structures [134].

Unlike classical Anderson localization phenomena, in these aperiodic systems the localization is not triggered by destructive interference phenomena, but rather determined by resonant effects between local nearest-neighbor scatterers via Mie resonance modes [155]. In fact, the intensity distributions shown in figure 33 indicate that the field patterns are essentially determined by the optical elements forming octagonal or decagonal rings in the Ammann–Beenker and Penrose lattices, respectively. This suggests a local interaction mechanism. In fact, these field distributions can be considered as antibonding states of the first Mie resonance modes of the octagonal ring cylinders in a tight-binding framework. In this regard, it is worth noting that the Mie modes themselves (located at $\omega = 0.16$ and $\omega = 0.37$) lie far from the PBGs shown in figure 30. The nature of the band-edge states in 2D aperiodic lattices, however, cannot be properly addressed by considering relatively small systems containing about 100–200 optical elements only, and it is reasonably expected that the transport properties of very large quasiperiodic systems may be more complicated as compared with approximants based on the finite-size unit cells (figure 29). For instance, ring–ring interactions mediated by significantly extended critical modes, exhibiting self-similar patterns, may introduce novel optical phenomena. In fact, experimental studies on the emission in a Penrose-type QC laser provided clear indication that the lasing action stems from well-defined extended modes that are coherently spread (with a coherent length $\geqslant 100a$) through the sample due to the quasiperiodic long-range order of the quasi-lattice [161, 162]. Quite remarkably, recent numerical studies analyzing how the properties of band-edge states evolve with sample size in Stampfli lattices containing up to 10^4 dielectric cylinders show that these states are characterized by the presence of a hierarchy of local resonances which progressively appear as soon as the size of the considered sample allows for it. In this way, the self-similarity of the structure properly manifests itself in the quasiperiodic limit [163].

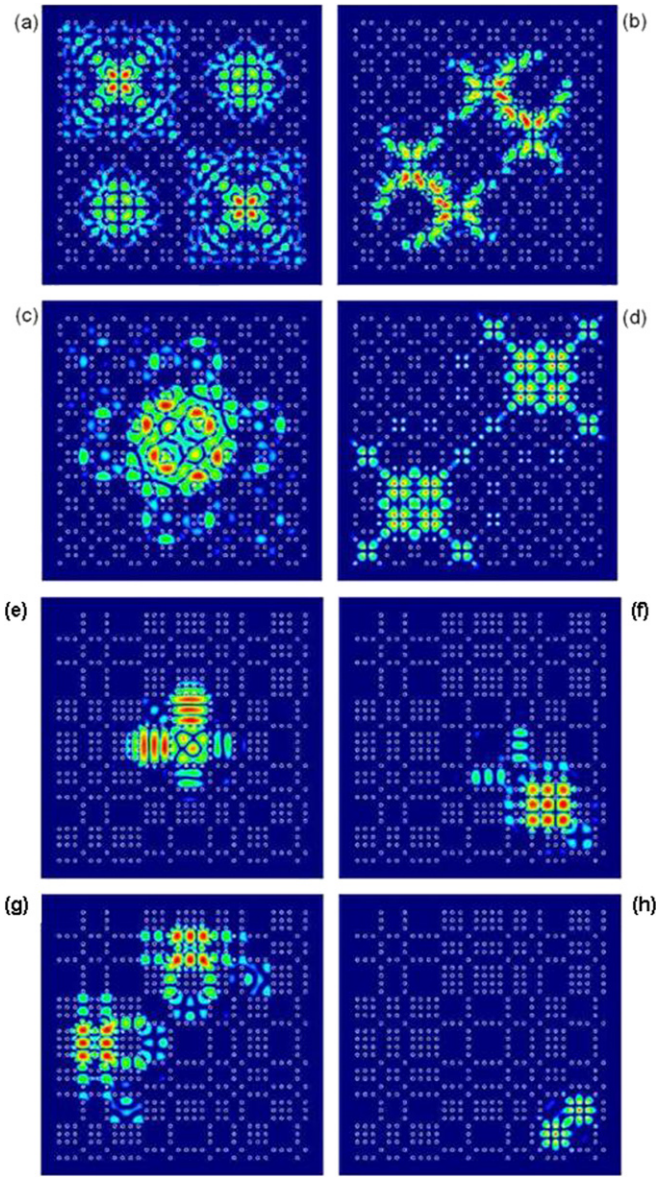

Figure 32. Electric field patterns of selected critical modes in and around the first TM band gap of a Thue–Morse (top panels) and Rudin–Shapiro (low panels) structures with $N = 512$ dielectric cylinders. (*a*) $a/\lambda = 0.452$, $Q = 891$; (*b*) $a/\lambda = 0.417$, $Q = 16940$; (*c*) $a/\lambda = 0.339$, $Q = 3363$; (*d*) $a/\lambda = 0.262$, $Q = 860$; (*e*) $a/\lambda = 0.397$, $Q = 41070$; (*f*) $a/\lambda = 0.361$, $Q = 3002$; (*g*) $a/\lambda = 0.400$, $Q = 31530$; (*h*) $a/\lambda = 0.279$, $Q = 1212$. (Adapted from [134]. Courtesy of Luca Dal Negro.)

On the other hand, point defects (missing cylinders) or line defects (missing rows of cylinders) can be, respectively, used to create highly localized defect modes or to form waveguides in PBG systems in both periodic and aperiodic systems alike. The existence of such localized modes can be fruitfully exploited in order to design single-cell resonators with high-quality factors [164], or coupled-resonator optical waveguides [165]. Numerical evidence of guided resonances in Ammann–Beenker octagonal tilings obtained by placing air holes in a silicon slab at the positions of the tiling vertices has recently been reported [153]. This result indicates that spatial periodicity is not an essential requirement for their excitation, thereby providing new degrees of freedom in the engineering of guided resonances [166].

3.4. Optimized structures

Several methods to find optimal dielectric patterns rendering the widest PBG for two-component PQCs have recently been proposed. For the case of TM polarization, nearly optimal decoration for a given pattern is obtained by placing identical optical elements centered at each lattice point and properly adjusting their radius in order to tune Mie and Bragg scattering effects, leading to substantial band gaps. On the other hand, to obtain optimal PBGs for TE polarization, tile edges are replaced by a dielectric wall of finite thickness and the vertices by cylinders of finite radius. In this way, the tiles can be regarded as individual scattering objects supporting electromagnetic resonances, which couple to each other when placed in the connected network [167, 168]. From these studies it has been reported that, at low-dielectric contrasts, the higher symmetry quasicrystalline structures have greater band gaps than the crystalline ones, but, at higher contrasts, the hexagonal periodic structure yields the greater PBGs. Significantly, for all considered contrasts, optimized PQCs gaps are more isotropic than those of periodic structures due to the fact that their effective Brillouin zones are more circular than the Brillouin zones of periodic photonic crystals. Thus, it seems natural to investigate aperiodic structures exhibiting progressively higher order rotational and mirror symmetries.

To this end, novel methods for designing PQCs without relying on geometrical tilings have been introduced. For instance, in the so-called inverse Fourier transform method one starts by choosing an n-sized polygon in the reciprocal space and subsequently one derives the optical elements positions required in real space. In this way, one can design PQCs with relatively wide PBGs possessing an arbitrary number of rotational symmetries such as those found in 18-fold, 40-fold and 120-fold aperiodic lattices [169, 170]. Nonetheless, up to now the best approximation to a 'Bragg ring' in reciprocal space has been obtained in spiral lattices based PQCs. By comparing the PBG in the spiral lattice shown in figure 26 with those corresponding to periodic hexagonal, on the one hand, and Stampfli dodecagonal PQCs, on the other hand, it is concluded that the spiral lattice exhibits one of the widest complete TM gaps ($\Delta\omega/\omega = 21\%$) reported to date (September 2011) for the low-contrast index value $\Delta\epsilon = 2$. In comparison the Stampfli lattice has $\Delta\omega/\omega = 14\%$ and the hexagonal lattice has $\Delta\omega/\omega = 5.6\%$ for the same $\Delta\epsilon$ value. The sunflower's low-contrast wide PBG stems from long-range interactions allowing for the delocalized optical states to sampling the overall spiral structure, so that the Bragg ring incorporates many reciprocal space contributions to further broaden the gap. In contrast, Bragg reflection from periodic crystals acts on a sparse pure-point Fourier space, thereby restricting the overlap of low-contrast spectral gaps [146].

Evolutionary optimization techniques, such as the particle-swarm optimization algorithm [171], have recently been used in order to design plasmonic silver nanospheres arrays able to achieve broad-band field enhancement spanning

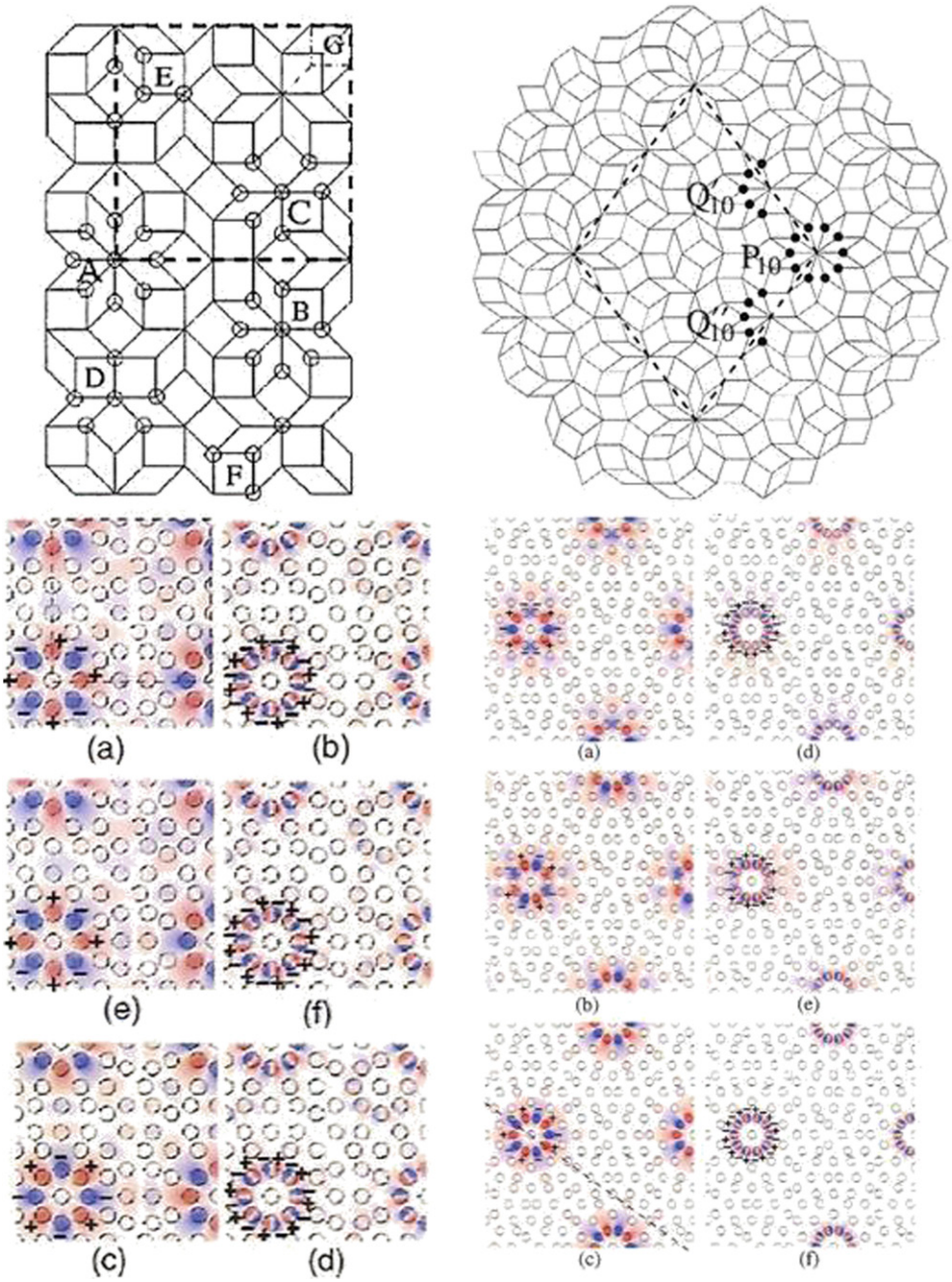

Figure 33. Upper left panel: a portion of the Ammann–Beenker tiling showing the six possible local patterns marked by circles and labeled from A to F according to their (decreasing) index coordination number. Upper right panel: a portion of the decagonal Penrose tiling showing complete (P_{10}) and incomplete (Q_{10}) pentagonal rings. Bottom left panel: electric field patterns at Γ, *X* and *M* points for bands below the two main PBGs at $\omega = 0.24$ (*a*), (*c*), (*e*) and $\omega = 0.45$ (*b*), (*d*), (*f*) ($\omega a/2\pi c$ units) in the 3/2 octagonal approximant of the Ammann–Beenker tiling (figure 30(*b*)). For both bands the electric field is localized on the same octagonal ring of pattern A, which is the most symmetrical local pattern. Bottom right panels: electric field patterns for the localized modes inside the first (*a*)–(*c*) and second (*d*)–(*f*) main PBG of the Penrose decagonal approximant shown with arrows in figure 30(*e*). (Adapted from [151, 155, 156].)

the 400–900 nm spectral range [172]. The resulting optimized structure is aperiodic and features a dense Fourier transform similar to those previously reported for deterministic aperiodic lattices with absolutely continuous Fourier spectra [134, 138].

4. Three-dimensional arrangements

In this section we will address a further extension of aperiodic order in optical devices by considering bulk aperiodic systems in three dimensions (3D). Although currently available nanotechnology offers several ways to construct aperiodic structures in 1D and 2D, fabrication of 3D structures by means of these techniques remains a challenging problem. This situation introduces a mismatch between computer based design capability of 3D aperiodic patterns and their fabrication capability. To overcome this mismatch, two useful methods have recently been introduced, namely laser holographic lithography and direct-laser-writing techniques [173]. In particular, laser holographic lithography relies on

the interference of several coherent laser beams to produce a pattern that is recorded (due to photoinduced polymerization) in a photoresist material template. However, the opening of complete PBGs requires materials with refractive indices higher than 2, a condition which is not generally met by photoresist resins. Accordingly, a second step is introduced in the fabrication process, consisting of the infiltration of a high refraction index material (e.g. silicon) which fills the voids in the photoresist template and is subsequently removed by acidic and calcination treatments, leaving the inverse of the original low-refraction index template [174]. Alternatively, one can dope metal nanoparticles in the photoresist in order to obtain optically active materials with an enhanced refraction index contrast.

A promising approach using a nonlinear photorefractive material (e.g. cerium doped strontium barium niobate) instead of photoresist materials has recently been demonstrated. In this case, the refractive index modulation leading to the photonic quasi-lattice formation is caused by two intertwined processes. Under the influence of an externally applied electric field, the incident laser light induces a charge carrier distribution that results in a macroscopic charge spatial distribution in the photorefractive material. This, in turn, leads to a space-dependent refractive index modulation via the electro-optic nonlinear effect. The main point of this approach is that apart from the possibility of permanently fixing the generated structures in the photorefractive material, the recorded structure is reconfigurable as well. In fact, it can be easily erased by a flush of white light so that new patterns could again be recorded in the supporting material [175].

4.1. Axial photonic quasicrystals

An obvious extension to three dimensions of the 2D aperiodic patterns considered in section 3 consists of simply piling up 2D aperiodic planes along the third, namely z, direction. In this way, one obtains a hybrid order structure which is periodic in the growth direction and aperiodic in the perpendicular planes, which we will refer to as *axial PQCs*. These structures then mimic at a micrometer scale the atomic arrangement observed in the so-called decagonal phase of quasicrystalline alloys. Following this approach, a PQC exhibiting the Penrose structure in the xy plane was fabricated using ten-beam laser (488 nm Ar) holographic lithography in a polymer resin with $n = 1.62$. Normal incidence (along the z-axis) reflection and transmission spectra indicated the presence of band gaps which approximately follow Bragg's diffraction relation $\lambda_{\mathrm{gap}} \simeq 2d_z n_{\mathrm{eff}}$, where d_z is the z-axis periodicity and n_{eff} measures the effective refraction index as a function of the sample's filling factor [176]. On the other hand, making use of the previously mentioned reconfigurable, optically induced, nonlinear photonic lattice approach, several axial PQCs exhibiting 8-fold, 19-fold, 27-fold and 32-fold symmetry axes have been obtained [175].

4.2. Icosahedral photonic quasicrystals

As we have seen in section 3, complete (i.e. for both TE and TM polarizations) PBGs appear due to the overlapping of band gaps in all possible directions. For a 3D periodic distribution of the dielectric function, different directions correspond to different periodicities and, consequently, to different frequency values for the stop band centers. The required overlapping of the different stop bands can only be ensured if these bands are wide enough. Motivated by this basic principle, several theoretical studies concluded that lattices with diamond symmetry have the minimum permittivity modulation contrast necessary for the appearance of a complete PBG among the materials based on periodic order. Such a requirement could be relaxed to some extent if the considered solid exhibits a more isotropic periodicity, so that the Brillouin zone is close to being spherical. To this end, a high degree of symmetry is an advantage as it makes the optical properties more isotropic and the operation less dependent on the angle of the incident light. Now, it is well known that QCs have higher order point group rotational symmetries along with long-range quasiperiodic order, so that photons can be diffracted as efficiently as they are by periodic structures. The existence of a complete band gap in icosahedral PQCs was theoretically inferred from band structure calculations of 3D cubic approximants of a 6D bcc cubic hyperlattice. The approximants of successive 1/0 and 1/1 orders exhibit quite isotropic and relatively large PBGs ($\Delta\omega/\omega = 17.6\%$ and $\Delta\omega/\omega = 10.3\%$, respectively) for a wide range of relative permittivity values with a threshold at $\epsilon \simeq 6$ [177].

A centimeter scale PQC based on a generalized version of Penrose tiling in three dimensions was fabricated by ultraviolet laser photopolymerization stereolithography (figure 34(a)) and microwave transmission measurements within the range 8–42 GHz were performed. The sample exhibited large stop bands in certain directions closely related to the main symmetry axis of the icosahedral group (figures 34(b) and (c)) [178]. Nevertheless, the transmission spectrum is less structured than originally expected on the basis of a dense filling of the reciprocal space in icosahedral QCs, which should give rise to many gaps at different frequencies. This result partially agrees with some theoretical studies showing that the electronic structures of the 3D Penrose lattice are quite smooth and not so spiky as was commonly assumed [179], though it should be also kept in mind that long-range order may be significantly perturbed by the unavoidable presence of structural imperfections in the sample [180]. Icosahedral PQCs were subsequently obtained for the infrared [174], and visible ranges [181]. In the first case, samples of 48 μm in diameter were made by direct laser writing in a photoresist material (SU-8) followed by a subsequent silicon single-inversion procedure. The quasiperiodic structures were generated by the following algorithm: (i) one starts from a 6D simple cubic lattice with all its nearest neighbors lattice points connected by ideal straight lines, (ii) this 6D lattice is rotated around the vertex point (0, 0, 0, 0, 0, 0) by the 6×6 matrix [174]

$$\frac{1}{\sqrt{4+2\tau}}\begin{pmatrix} \tau & \tau & 0 & -1 & 0 & 1 \\ 0 & 0 & 1 & \tau & 1 & \tau \\ 1 & -1 & -\tau & 0 & \tau & 0 \\ \tau & -\tau & 1 & 0 & -1 & 0 \\ -1 & -1 & 0 & -\tau & 0 & \tau \\ 0 & 0 & \tau & -1 & \tau & -1 \end{pmatrix}, \qquad (42)$$

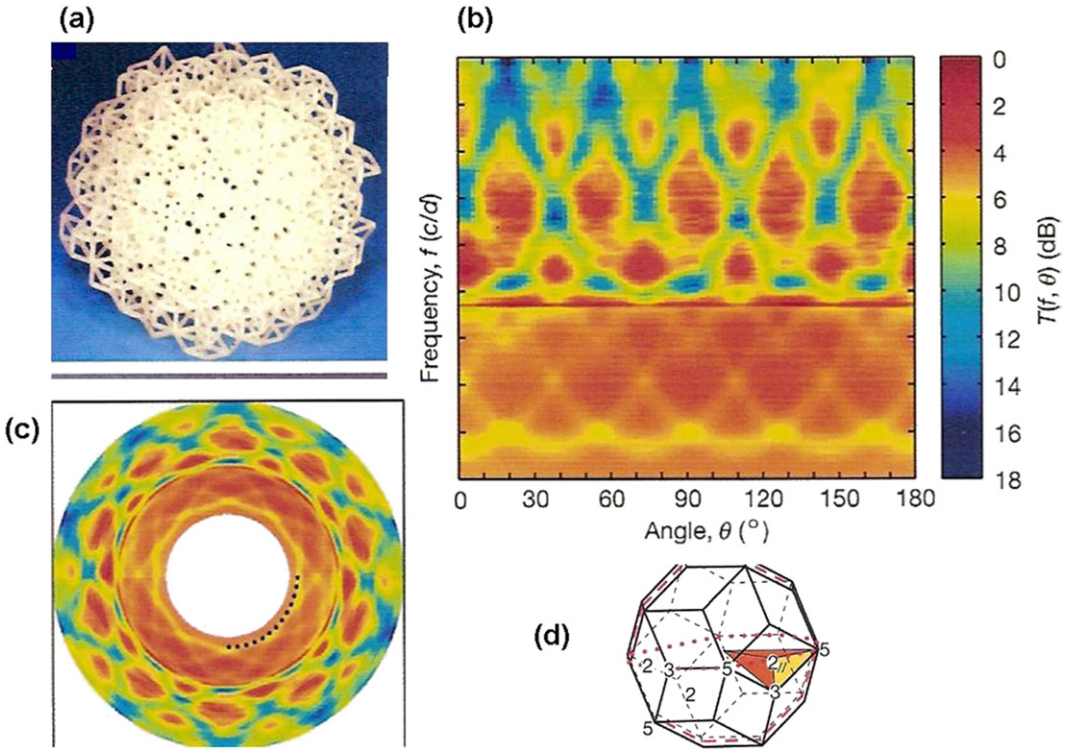

Figure 34. (*a*) Stereolithographically fabricated icosahedral PQC made of 4000 dielectric rods ($n = 1.62$) of length $d = 1$ cm and radius $r = 0.075$ cm. (*b*) Measured transmission as a function of the frequency (measured in c/d units) and the light propagation angle around a five-fold rotation axis. (*c*) Imaging of the Brillouin zone for the icosahedral PQC derived by locating the points in reciprocal space responsible for the gaps. The inner decagon corresponds to the dashed line in the triacontahedral Brillouin zone shown in (*d*). (Adapted from [178].)

where τ is the golden mean, and (iii) the second three coordinates of the resulting 6D vector determine whether or not a lattice point is projected: if they are positive, then the first three coordinates represent the real-space position of this lattice point. The resulting lattice points are separated by a distance $l = 2\,\mu$m and the number of lattice planes is 15.

In the second case, millimeter-sized samples were fabricated using a seven-beam optical interference holography method in both SU-8 photoresist resin ($n = 1.62$) and a dichromate gelatin plate ($n = 1.57$). A 3D microstructure modulation of the refractive index, exhibiting the icosahedral group symmetry elements, was generated at the μm scale. Despite the relative low-dielectric contrast, the PQC displayed nice diffraction patterns and pentagonal-shaped sharp reflections under the white light for normal incidence. Transmission spectra showed angular-dependent band gaps at 560, 500 and 400 nm in the visible range [181]. Subsequently, observation of multidirectional lasing exhibiting icosahedral symmetry at wavelengths in the range 580–600 nm has been reported for Rhodamine dye-doped PQCs fabricated in dichromate gelatin emulsions by the seven-beam optical interference holographic method. Quite interestingly, some of the observed lasing modes are oriented in almost the same direction, so they cannot be resolved by the detecting system, resulting in the appearance of a multimode effect. This lasing feature is unique to 3D PQCs, unlike 2D ones, and can be properly regarded as a *dimensionality* effect of aperiodic systems [182].

4.3. Spherical and cylindrical geometries

Since a sphere has the highest symmetry of all possible structures it is expected that devices based on spherical shells are, in principle, ideal for achieving complete PBGs. In addition, a concentric arrangement of spherical shells can exhibit PBGs in any direction pointing toward the center of the structure, without requiring high dielectric contrast materials to this end. Certainly, to fabricate such an arrangement of concentric shells is not an easy task using common microfabrication techniques, though the holographic lithography methods discussed in the previous paragraphs are a promising approach. In fact, at least in principle, one can obtain a spherical light pattern from a point source located at the center of a spherical mirror which interferes with the own mirror's reflected light. Based on this approach, spherical layered structures with different curvatures (ranging from 1.0 to 9.5 mm) have recently been fabricated in dichromate gelatin emulsions [183]. As expected, the obtained structures behave like curved mirrors and exhibit complete PBGs in the visible, within the 500–600 nm spectral range (depending on the curvature of the sample) and with typical bandwidths of about 50 nm, despite the low-dielectric contrast of the employed material.

The potential use of compound aperiodic structures based on a dielectric microsphere which is coated by a series of alternate materials arranged according to the Fibonacci sequence has been numerically analyzed. The overall structure is made of elemental spherical cells composed of two types

of bilayers, namely a thick shell with two $\lambda/4$ layers of widths d_1 and d_2 and a thinner shell with two layers of width $\{d_2, \gamma d_1\}$, ($\gamma < 1$). A key feature of this system is that the preservation of the energy flux in a solid angle along the radial direction requires the consideration of the external (r_{i+1}) and internal (r_i) boundaries of each layer, so that one must consider the order number of the layer, i, to properly express its thickness $d_i = r_{i+1} - r_i$. This is a direct consequence of the existence of a preferential point in the system (its center) which breaks the homogeneity usually present in the 1D multilayers based on planar slabs considered in section 2 (note that the layer thicknesses of the distorted multilayer described in section 2.2.3 also depend on the sequence label according to (21)).

The mathematical treatment of wave propagation through spherical multilayers is similar to that described in section 1 by expressing the Helmholtz equation (2) in terms of a scalar function, called the Debye potential $\Pi(r)$, as

$$\frac{\mathrm{d}^2\Pi}{\mathrm{d}r^2} + \left[\frac{\omega^2}{c^2}n^2(r) - \frac{l(l+1)}{r^2}\right]\Pi = 0, \tag{43}$$

where l is the angular momentum [184]. This expression can be solved in terms of the spherical Hankel functions and the propagation of the wave can be described in terms of a series of transfer matrices containing these functions. Nevertheless, in the spherical multilayer case these transfer matrices are no longer unimodular, since their determinant is given by the ratio $(r_{i+1}/r_i)^2 > 1$ [185]. Another consequence of the spherical geometry is that the transfer matrix depends not only on the thickness of the layer but also on the distance of the considered block to the center. As a result, in the study of quasiperiodic stacking of shells, simple concatenation rules like $S_{n+1} = S_n S_{n-1}$, giving the Fibonacci stacking sequence in 1D layered systems (see section 2), must be replaced by the following one for the spherical Fibonacci stack [186, 187],

$$\boldsymbol{K}_{n+1}(n+1) = \boldsymbol{K}_n(n)\boldsymbol{K}_{n-1}(F_{n+2}). \tag{44}$$

where $\boldsymbol{K}_i(n)$ denotes the bilayer transfer matrix for the nth Fibonacci generation. Two different realizations of this spherical arrangement have been considered to date, one based in conventional materials and the other including left-handed materials as well. It was found that: (i) as the number of layers increases, the frequency spectrum becomes more and more fragmented, exhibiting extremely narrow transmission peaks (say ~0.04 nm in width for a F_9 Fibonacci generation containing 34 bilayers), and (ii) for the particular choice $\gamma = \tau^{-1}$, the band gap width is considerably wider in spherical structures containing left-handed materials than those composed of conventional materials. In addition, the precise location of the narrow transmission peaks can be changed by properly tuning the structural parameter γ value, allowing for the design of optical filters with extremely narrow passbands [185–187].

On the other hand, cylindrical geometries have been considered in the design of coaxial optical waveguides. In this regard, it has been experimentally shown that light waves with different frequencies in the visible spectral range can be selectively guided and spatially separated along the radial direction in a self-similar dielectric waveguide, where a hollow cylindrical core ($R = 380$ nm) is surrounded by a concentric series of cylindrical layers of two alternating materials ($n_A = 4.6$, $d_A = 33$ nm, and $n_B = 1.6$, $d_B = 67$ nm) radially arranged according to the Thue–Morse sequence [188]. In this way, a 'rainbow' can be trapped, that is, spatially confined but not stopped, in the Thue–Morse waveguide (figure 35). The physical origin of this feature can be traced back to the self-similar nature of the refractive index profile in the radial direction, which allows for the appearance of a progressive multifurcation of PBGs by increasing the generation of the Thue–Morse sequence.

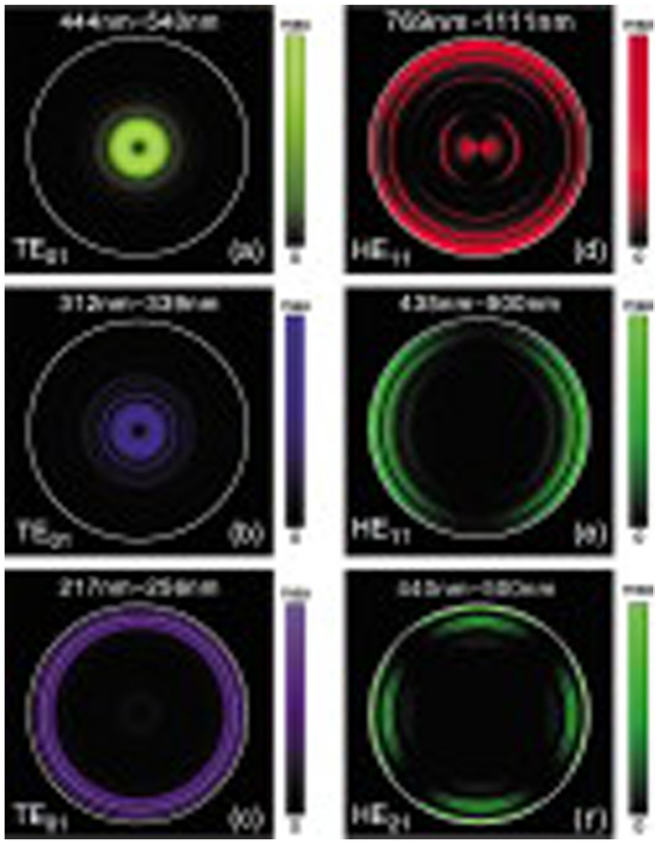

Figure 35. The electric field time-average energy density distribution in a third generation Thue–Morse waveguide for different modes. Reprinted with permission from [188]. Copyright 2008, American Chemical Society. (Courtesy of Rue Wen Peng.)

5. Conclusions

5.1. Aperiodicity versus periodicity

What can be done with aperiodic based photonic devices that cannot be done with periodic based ones? From the results discussed through the preceding sections we conclude that:

(i) at a fundamental level, basic physical processes are essentially the same in both periodic and aperiodic optical systems. Illustrative examples of these processes include (*a*) interference effects leading to the formation of PBGs, (*b*) lasing action due to either coherently extended Bloch or critical states, (*c*) quasi-phase matching condition in

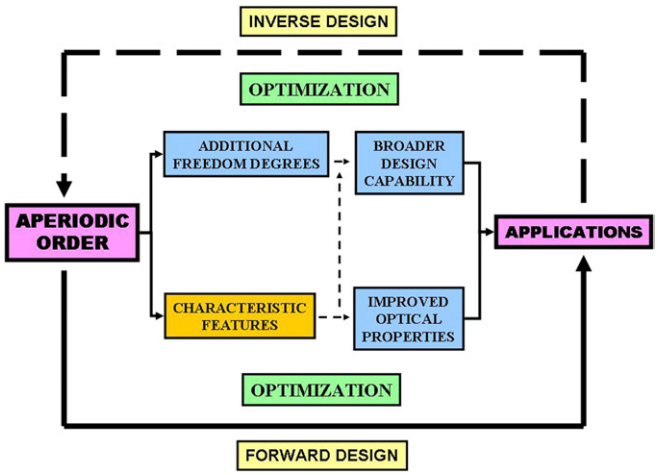

Figure 36. Sketch illustrating the two routes for optical device optimization: forward and inverse designs. The way toward useful applications based on aperiodically arranged structures relies on a suitable explotation of additional degrees of freedom, on the one hand, and a number of characteristic features intrinsic to aperiodic order, on the other.

second harmonic generation or (d) the coupling between the electromagnetic wave and the collective motion of electrons at the dielectric–metal interface governing extraordinary light transmission through a metallic slit array [189, 190],

(ii) aperiodic order, by itself, endows aperiodic optical systems with certain *characteristic properties* (described below) which are not exhibited by periodic systems,

(iii) in most cases these characteristic properties lead to a richer phenomenology, resulting in *improved optical properties* as compared with their periodic counterparts,

(iv) by properly combining these improved optical properties with the *additional degrees of freedom* inherent to the aperiodic arrangements, one can design better performing optical devices for some specific applications. Thus, aperiodic structures offer a broader and more flexible *design capability* than their periodic counterparts,

(v) finally, unlike random media, aperiodic structures are generated by well-defined deterministic algorithms, so that they are amenable to precise *engineering* and *optimization* procedures.

In figure 36 we depict the fundamental relationship between the above emphasized features and the intrinsic capabilities of aperiodic systems to eventually outperform periodic ones in certain applications. In the *forward design* approach one starts from an aperiodic structure with a given aperiodic pattern (namely Fibonacci sequence, Penrose tile or icosahedral quasi-lattice, for instance) and derives its optical response, subsequently comparing it with state-of-the-art results corresponding to periodic orderings in order to identify possible competitive technological domains. In the *inverse design* approach, one is interested in obtaining a device exhibiting, say, a series of reflection peaks at certain wavelengths, or a stop band of a certain width extending over certain spectral range from the very beginning. To this end, one proceeds via optimization procedures which can be generally split into broad categories, namely parameter choice and type-of-order choice optimization. In the former case, one selects a given aperiodic arrangement from the start and determines the best combination of physical parameters (layer thicknesses, rod radii, refractive index contrast, filling ratio) in order to fit in the predetermined optical requirements. On the other hand, type-of-order optimization focuses on which is the most appropriate aperiodic order pattern to be used to accomplish those optical requirements. We will further comment on this interesting issue in section 5.2, but first it is convenient to describe in more detail the most characteristic properties of aperiodic order based designs, namely a *highly fragmented* frequency spectrum, the presence of *critical modes* and the existence of *novel symmetries*, including higher rotational and inflation ones. In table 2 we summarize the main advantages of aperiodic designs over their periodic counterparts.

Due to their *highly fragmented* frequency spectra, aperiodic multilayers offer more full transmission peaks than periodic ones in a given frequency range for a given system length. This feature stems from the richer structural complexity of aperiodic sequences (related to quasiperiodic order and/or self-similarity), naturally leading to the presence of more resonant frequencies due to multiple interference effects throughout the structure. The presence of more frequencies for operation becomes particularly useful for a number of applications such as selective enhancement of thermal emission for some selected frequencies, or an improved frequency selectivity in waveguides.

The existence of *critical modes*, spatially more complex than those related to both extended Bloch or exponentially localized defect modes in periodic photonic crystals, gives rise to the possible existence of either relatively localized or significantly extended electromagnetic intensity patterns depending on the scattering processes involved. The occurrence of highly localized optical modes *in the absence of disorder* (i.e. in defect-free) PQCs is of interest for the fabrication of high quality factor resonators as well as coupled-resonator waveguides. In fact, the presence of critically localized states generally offers a higher degree of design and tuning flexibility [193]. Therefore, compared with periodic arrays, where the resonance of the nanocavity can be achieved for a single frequency with a specific electric field pattern, in aperiodic multilayers a multifrequency nanocavity array can exist, and for each frequency the electric field pattern has a different spatial behavior. Thus in contrast to periodic systems, spatial quasiperiodic order naturally introduces a full set of *non-equivalent sites* in 2D and 3D aperiodic arrangements. In this way, a great diversity of electromagnetic spatial patterns can be obtained for different frequencies. This property paves the way for the design of novel optical devices. For example, the systematic use of critically localized modes has been proposed as a novel approach for implementing label-free optical biosensing in aperiodic structures based on the Rudin–Shapiro lattice [194].

The presence of *inflation symmetries* in both PQCs and aperiodic multilayers gives rise to a denser reciprocal space, providing a superior flexibility in achieving quasi-phase matching conditions for higher harmonics generation

Table 2. Improved optical properties stemming from aperiodic order features along with their related potential applications.

Aperiodic feature	Optical property	Application	Ref
Spectrum fragmentation	Size-dependent transmission	Mirror reflectance tuning	[49, 51]
	Very narrow peaks	Higher spectral resolution	[34]
		Narrowband filters	[52]
	Smaller group velocities	Laser compression	[44]
	Multiple PBGs	Polychromatic cavities	[98, 196]
		Omnidirectional mirrors	[110, 111]
Critical localization	Resonant standing waves	Lasing pulse stretching	[36, 37]
	Faster emission rate	Luminescent devices	[38]
	Light emission enhancement	Non-linear optics	[43]
	Hierarchical EM patterns	Label-free biosensing	[194]
Novel symmetries	Refractive index contrast	Omnidirectional mirrors	[97]
	More isotropic bandgaps	Omnidirectional mirrors	[96]
	Denser reciprocal space	Higher harmonics generation	[41, 40]
Phason defects	λ-selective defects	Guided resonances	[153, 164]

processes in non-linear optics. The importance of an accurate knowledge of the resonance frequencies in the design of useful optical devices has been recently discussed within the context of nonlinear optical materials [191, 192]. As is well known, the narrower a resonance is, the easier it is to achieve bistability or multistability effects. Therefore, it can be expected that aperiodic structures consisting of nonlinear materials will offer richer bistable operations, particularly for switching applications.

The presence of forbidden symmetries in PQCs allows for the existence of *higher order rotational axes* (approaching the 'Bragg-ring' limit in the case of spiral lattices), which leads to more isotropic complete PBGs, generally requiring lower refractive index contrast values than those observed for periodic photonic crystals for their appearance. On the other hand, the possibility of designing flat lenses using quasiperiodic arrays of steel cylinders embedded in an air background has been theoretically discussed, comparing the behavior of superlenses based on a periodic distribution of metamaterials. In this case, the motivation for using the high-symmetry PQC is to maintain an efficient interference of waves (long-range order) while reducing the orientational order of the system (crystallographical restriction theorem is relaxed) to get a more isotropic propagation [195].

Finally, one can also benefit from purely structural features of aperiodic arrangements. For instance, aperiodic multilayers have less interfaces than periodic ones for a given system size, which is convenient in order to reduce losses and dispersion effects. It has also been reported that optical sensors based on Thue–Morse multilayers are more sensitive than those based on a periodic sequence (see section 1.5), since the lower number of interfaces in the former provides a higher filling capability [45]. Although generation order directly correlates with the system size (i.e. $N = F_k$ or $N = 2^k$), one may in principle design multilayers where the layer thickness progressively decreases as the generation order increases (i.e. $d = d(k)$) in order to keep the system size within attainable values. Another structural aspect of interest is the presence of a new sort of defects which are *intrinsic* to aperiodic order, so that no counterpart exists in usual periodic arrangements. These defects are generally referred to as *phasonic defects* and they

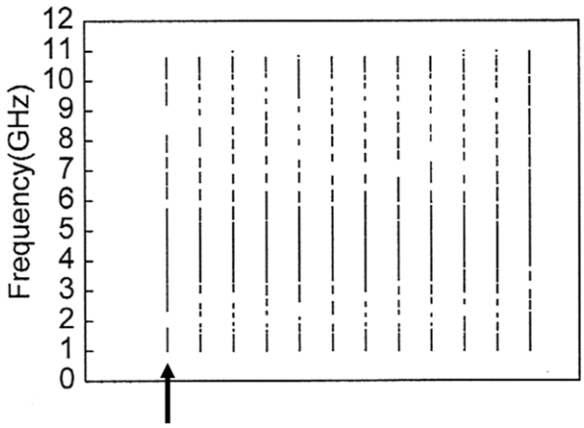

Figure 37. The frequency spectrum of a seventh order Fibonacci multilayer (arrowed) is compared with the spectra corresponding to eleven different realizations containing the same number of layers randomly distributed. Reprinted from [124] with permission from Elsevier. (Courtesy of Zhengyou Liu.)

can be readily visualized as distortions stemming from the projection of aperiodic structures when described in a high-dimensional space [16, 153].

Once we have highlighted the main characteristic properties of aperiodic devices, it is fair to note that aperiodic arrangements are not necessarily the best possible ones for all applications in all circumstances. For instance, the progressive fragmentation of the frequency spectra with increasing system size is a *generic* property of aperiodic systems but it is *not* a *specific* property of them. This is properly illustrated in figure 37 which shows comparable fragmentation degrees in the spectra of Fibonacci and random multilayers of the same size. Accordingly, the fragmentation is a general feature of complex enough systems, i.e. multilayers exhibiting a large number of non-equivalent local optical environments able to guarantee a rich variety of resonant frequencies through the allowed spectral window. Thus, the point is not the existence of a large number of gaps and transmission bands, but the fact that the location of *all* these spectral features can be precisely labeled in the case of aperiodic (i.e. quasiperiodic or fractal) multilayers only, whereas their positions cannot be known beforehand in the case of randomly grown multilayers.

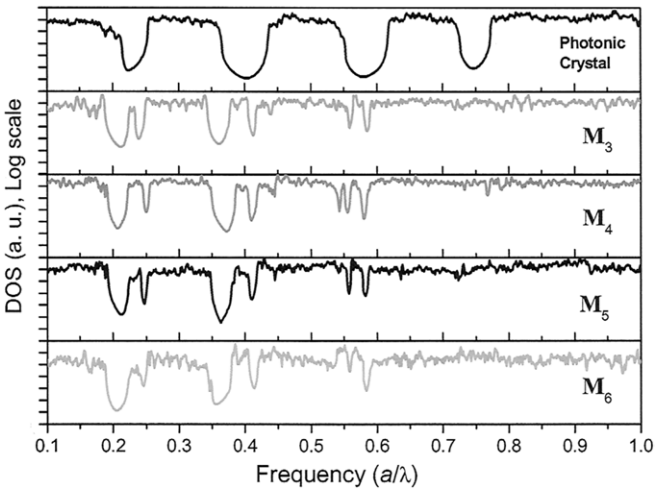

Figure 38. Comparison of the DOS of a 2D periodic photonic crystal (top panel) with that corresponding to a series of 2D Thue–Morse lattices of increasing generating order from M_3 (containing $N = 2^6 = 64$ pillars) up to M_6 (containing $N = 2^{12} = 4096$ pillars) [135]. (Courtesy of Luigi Moretti.)

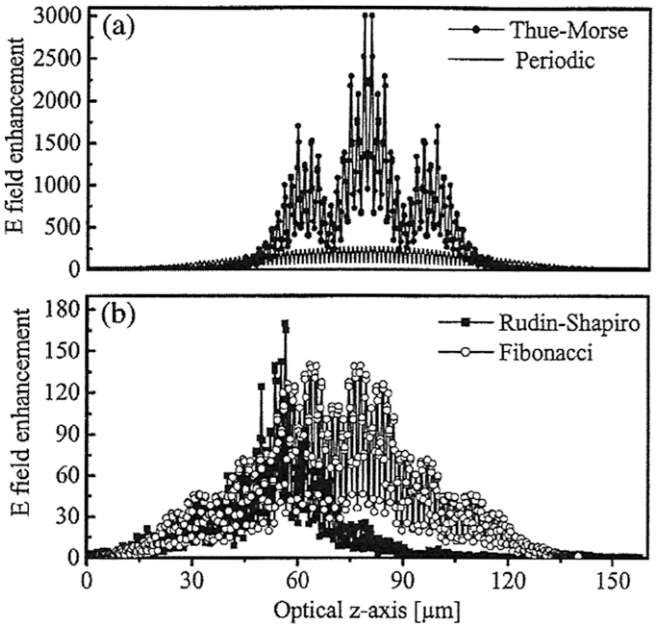

Figure 39. Comparison of localized band-edge mode electric field profiles for (*a*) $N = 128$ periodic and Thue–Morse multilayers at $\lambda = 1511.35$ nm and $\lambda = 1410.085$ nm, respectively. (*b*) Fibonacci ($N = 144$) and Rudin–Shapiro ($N = 128$) multilayers at $\lambda = 1421.53$ nm and $\lambda = 1486.9$ nm, respectively. The electric field values are normalized with respect to the input fields [198]. (Courtesy of Luca Dal Negro.)

On the other hand, it has been reported that, for high enough dielectric contrasts, the PBG of an optimized hexagonal periodic photonic crystal is larger ($\Delta\omega/\omega = 32.5\%$) than that corresponding to an optimized five-fold lattice ($\Delta\omega/\omega = 30.3\%$), in spite of the greater isotropy of the latter [167]. However, we note that though Thue–Morse and periodic binary multilayers are derived from substitution sequences which only differ by a letter permutation, this difference leads to significantly different transmission and localization properties (see sections 2.1 and 2.2). For instance, figure 38 compares the DOS of a M_3 Thue–Morse lattice with that corresponding to a photonic crystal with a periodic square arrangement of dielectric pillars in vacuum (see section 3.1). Since both structures share the same four-fold symmetry in reciprocal space (see figure 25), the PBGs appear in similar frequency regions. Nevertheless, some differences can be appreciated as well, namely (i) each PBG in the photonic crystal splits into the Thue–Morse structure, and (ii) the higher frequency PBGs of photonic crystal completely disappear in the aperiodic one [133, 135]. An additional advantage in the use of Thue–Morse multilayers has been demonstrated in the case of nonlinear materials, in particular for odd generation numbers (exhibiting conjugation rather than mirror symmetry, see section 2.2) where the nonlinearity is capable of making transmission sensitive to the propagation direction. This feature is completely absent in nonlinear periodic structures, where hysteresis curves are the same for the leftward and rightward light incidence [192, 197].

As we have seen, there are many different types of aperiodic structures amenable to their use in optical devices. Accordingly, one may wonder whether some aperiodic arrangements are preferable to others in order to get better performing optical systems for certain applications. Certainly, a definite answer does not yet exist, though a number of recent studies provide interesting clues, deserving closer scrutiny. In figure 39 the electric field enhancement of the band-edge states corresponding to different aperiodic multilayers is compared. It can be clearly appreciated that the periodic multilayer exhibits the lowest field enhancement. Among the aperiodic multilayers, the better performance is obtained for the Thue–Morse arrangement, whereas in the case of Fibonacci and Rudin–Shapiro sequences the electric field enhancements are more than one order of magnitude lower than those obtained for the Thue–Morse sequence [198]. It is likely that the improved efficiency of the Thue–Morse based multilayer may be related to its higher degree of internal symmetry (i.e. mirror and conjugations symmetries, see section 2.2.2) as compared with the other two aperiodic sequences.

In another recent study, the reflectivity spectra of periodic, Cantor-like, Fibonacci and generalized Fibonacci multilayers in the optical communication band centered at $\lambda = 1.55\,\mu$m have been compared, reporting that multilayers based on the generalized Fibonacci sequence are the most appropriate in order to design narrow and dense band filters [199]. As another instance, a comparative study of the confinement properties of different point-defected 2D cavities made of cylindrical dielectric rods arranged according to Penrose, dodecagonal, and periodic (triangular) geometries highlighted the potential advantages offered by PQCs in the design of resonant PBG-based particle accelerators. Specifically, it was reported that dodecagonal cavities outperform the periodic ones for small to moderate structure sizes [200]. A powerful method that enables omnidirectional reflectivity for all polarizations of incident light over a wide *selectable* range of wavelengths has recently been put forward within the context of inverse design engineering [201]. These omnidirectional multilayer reflectors are based on a certain aperiodic sequence which is appropriately determined in order

to satisfy those predetermined requirements. Accordingly, this approach provides a promising example of the aperiodicity by design concept introduced in section 1.6.

5.2. Outlook and perspectives

To conclude, I would like to comment on some recent works reporting on either novel designs or new conceptual approaches that will likely deserve closer attention in the years to come. Regarding novel designs, one may think of fabricating conventional *periodic* devices with complex enough unit cells which are entirely designed on the basis of concepts borrowed from aperiodic order theory. In this case, the system is still far from exhibiting typical long-range quasiperiodic effects, so that rather than exploiting aperiodic order on its own, one is properly working with *aperiodic order-inspired* designs instead. As a suitable example of this approach we can mention a high-channel-count plasmonic filter proposed on the basis of Fibonacci-class (see section 2.1.1) gratings [79].

A key question in any general theory of aperiodic systems concerns the relationship between their structural order and the physical properties stemming from their structure. In the particular case of optical devices, the structural order is determined by the refractive index spatial profile $n(\boldsymbol{r})$, which, for aperiodic systems, can be given in terms of substitution sequences, geometrical tilings, or explicit mathematical functions. Whereas both substitution sequences and geometrical tilings can only define a specific type of aperiodic refractive index pattern, the recourse to analytical functions allows for a more general treatment, so that one can describe different kinds of refractive index distributions within a unified mathematical approach. As an illustrative example in 1D, one can consider a binary multilayer composed of layers whose refraction index values are assigned depending on the sign of the auxiliary function $V_l = \cos(\alpha\pi l^{\nu})$ [202], where l labels the layer sequence, α and ν being real parameters, so that $n_l \to n_A$ if $V_l \leqslant 0$, and $n_l \to n_B$ otherwise. For $\nu = 1$ and rational α one has a periodic refractive index profile, whereas for an irrational α value the multilayer sequence becomes quasiperiodic. In addition, for $\nu < 1$ (alternatively, $\nu > 1$) the refractive index profile is described by an aperiodic modulation whose wavelength progressively increases (decreases) as l increases. Accordingly, by properly adjusting the values of the design parameters α and ν we can obtain a great diversity of aperiodic refractive index profiles, including both periodic and random-like ones ($\nu > 1$, irrational α). Thus, the parameter ν can be regarded as an exponent controlling the *aperiodicity degree* of the considered structure [203].

Numerical transmittance curves as a function of ν have been recently reported for multilayers based on this sequence (with $\alpha = \sqrt{5} - 1)/2$, the reciprocal of the golden mean) in a systematic way. The obtained results show the existence of a characteristic ν value leading to averaged reflectivity values larger than those corresponding to random structures of comparable size [203]. This approach then opens a promising way to optimize the optical performance of aperiodic dielectric mirrors. A similar idea has recently been exploited in order to control lasing characteristics via structural *aperiodicity optimization*. To this end, one properly modulates the size of scatterers in a 2D aperiodic pattern like that shown in figure 24. Varying their size ratio, b, induces a gradual transition from a strictly aperiodic ($b = 0$) to a completely periodic ($b = 1$) pattern. In the particular case of Thue–Morse structures, it has been experimentally demonstrated that maximal light confinement is achieved at the intermediate value $b = 0.75$, where lasing becomes the strongest [204].

Another interesting way of stacking layers in a multilayered aperiodic structure is based on DNA molecules. In this case the layer sequence is determined by assigning the purine (pyrimidine) nucleotides along one of the DNA strands to dielectric layers with refractive index values n_A (n_B), respectively. Therefore, the resulting $n(z)$ function mimics the DNA nucleotide sequence and can be considered a *bio-inspired optical analog* of this macromolecule. The key point is that transmittance spectra obtained from light propagation through this optical analog will display a rich distribution of peaks resulting from the long-range correlations which are known to occur among nucleotide base pairs in intron (codifying) and exon (non-codifying) DNA regions [205]. In fact, computational studies of some DNA-inspired multilayered structures have reported that, for a given multilayer size, the number and height of resonant transmission peaks in the obtained transmittance curves systematically increases as the long-range correlations strength of the underlying base pair sequence is increased [206]. Accordingly, one could, at least in principle, quickly discriminate between codifying and non-codifying genome regions by inspecting different DNA optical analogs transmittance spectra.

As we have discussed in previous sections, the characteristic distribution of nested peaks in reciprocal space, arranged according to a never ending (at least in principle) self-similar pattern, is at the root of a number of intriguing and useful physical properties of aperiodic structures. Accordingly, to shift the attention from the physical space to the reciprocal one seems a convenient procedure when trying to search for novel designs of practical interest. This very promising approach has recently been explored, and a general theory to identify those aperiodic structures having the most useful band properties has been introduced by means of a Fourier-space based inverse optimization algorithm. One can manipulate the Fourier components of an aperiodic system in order to design and engineer any PBG structure at will [207]. In this way, one may think of a new technological research field which focuses on the smaller possible scales a system exhibits in reciprocal space, rather than in physical space. Such a topic of research (which we could tentatively refer to as *nano-reciprocal-space science*) closely follows the sequence of theoretical events which were progressively disclosed as the novel paradigm of order without periodicity attained its present status, and I guess it could profitably guide the next generation of condensed matter physicists and materials science researchers alike, far beyond the still narrow frontiers of knowledge imposed by our current limited understanding about the role of aperiodic order in science and technology.

Acknowledgments

I warmly thank Luca Dal Negro, Sergey V Gaponenko, Gerardo G Naumis and Rue Wen Peng for many useful comments and for sharing different materials of common interest during the last decade. I thank Eudenilson L Albuquerque, Juan Antonio Monsoriu, Michael E Pollard, Xóchitl I Saldaña and Diederik S Wiersma, for kindly providing some of the pictures which illustrate the text. I am indebted to Victoria Hernández for her assistance in preparing the manuscript. This work has been supported by the Universidad Complutense de Madrid and the DGUI of Comunidad de Madrid through project CCG10-UCM/MAT-4628.

References

[1] Maciá E and Domínguez-Adame F 2000 *Electrons, Phonons and Excitons in Low Dimensional Aperiodic Systems* (Madrid: Editorial Complutense)
[2] Albuquerque E L and Cottam M G 2003 *Phys. Rep.* **376** 225–337
[3] Albuquerque E L and Cottam M G 2004 *Polaritons in Periodic and Quasiperiodic Structures* (Amsterdam: Elsevier)
[4] Dubois J M 2005 *Useful Quasicrsytals* (Singapore: World Scientific)
[5] Wiersma D S, Sapienza R, Mujumdar S, Colocci M, Ghulinyan M and Pavesi L 2005 *J. Opt. A: Pure Appl. Opt.* **7** S190–7
[6] García-Moliner F 2005 *Microelectron. J.* **36** 870
[7] Maciá E 2006 *Rep. Prog. Phys.* **69** 397–441
[8] Steurer W and Sutter-Widmer D 2007 *J. Phys. D: Appl. Phys.* **40** R229–47
[9] Poddubny A N and Ivchenko E L 2010 *Physica* E **42** 1871–95
[10] Gaponenko S V 2010 *Introduction to Nanophotonics* (Cambridge: Cambridge University Press)
[11] Dal Negro L and Boriskina S V 2011 *Laser Photon. Rev.* at press (doi:10.1002/lpor.201000046)
[12] Shechtman D, Blech I, Gratias D and Cahn J D 1984 *Phys. Rev. Lett.* **53** 1951–4
[13] Levine D and Steinhardt P J 1984 *Phys. Rev. Lett.* **53** 2477–80
[14] Steurer W and Deloudi S 2009 *Crystallography of Quasicrystals—Concepts, Methods and Structures* (*Springer Series in Materials Science* vol 126) (Berlin: Springer)
[15] Maciá E and de Boissieu M 2011 *Properties of CMAs: Theory and Experiments* in *Complex Metallic Alloys. Fundamentals and Application* ed J M Dubois and E Belin-Ferré (Weinheim: Wiley)
[16] Maciá E 2009 *Aperiodic Structures in Condensed Matter: Fundamentals and Applications* (London: Taylor and Francis)
[17] Levi A F J and Hass S ed 2010 *Optimal Device Design* (Cambridge: Cambridge University Press)
[18] Merlin R, Bajema K, Clarke R, Juang F Y and Bhattacharya P K 1985 *Phys. Rev. Lett.* **55** 1768–72
Merlin R and Clarke R 1990 *US Patent Specification* 4.955.692
[19] Livio M 2002 *The Golden Mean* (New York: Broadway Book)
[20] Maciá E and Domínguez-Adame F 1996 *Semicond. Sci. Technol.* **11** 1041–5
[21] Endo A and Iye Y 2008 *Phys. Rev.* B **78** 085311
[22] Panchadhyayee P, Viswas R, Sinha C and Mahapatra P K 2008 *J. Phys.: Condens. Matter* **20** 445229
[23] Hsueh W J, Chen C H and Lai J A 2010 *Eur. Phys. J.* B **73** 503
[24] Mishra S and Satpathy S 2003 *Phys. Rev.* B **68** 045121
[25] Yablonovitch E 1987 *Phys. Rev. Lett.* **58** 2059–62
[26] Joannopoulos J D, Meade R D and Winn J N 1995 *Photonic Crystals: Molding the Flow of Light* (Princeton, NJ: Princeton University Press)
[27] Sibilia C, Tropea F and Bertolotti M 1998 *J. Mod. Opt.* **45** 2255
[28] Järrendahl K, Dulea M, Birch J and Sundgren J E 1995 *Phys. Rev.* B **51** 7621–31
[29] Zhukovsky S V, Lavrinenko A V and Gaponenko S V 2004 *Europhys. Lett.* **66** 455
[30] Gaponenko S V, Zhukovsky S V, Lavrinenko A V and Sandomirskii K S 2002 *Opt. Commun.* **205** 49
[31] Chigrin D N, Lavrinenko A V, Yarotsky D A and Gaponenko S V 1999 *Appl. Phys.* A **68** 25
[32] Lavrinenko A V, Zhukovsky S V, Sandomirski K S and Gaponenko S V 2002 *Phys. Rev.* E **65** 036621
[33] Domínguez-Adame F and Maciá E 1995 *Phys. Lett.* A **200** 69–72
[34] Pan F M, Jin G J, Wu X L, Feng J W, Hu A and Jiang S S 1996 *J. Appl. Phys.* **80** 4063–6
[35] Gardner M 1977 *Sci. Am.* **236** 110
[36] Dal Negro L, Oton C J, Gaburro Z, Pavesi L, Johnson P, Lagendijk A, Righini R, Colocci M and Wiersma D S 2003 *Phys. Rev. Lett.* **90** 055501
[37] Ghulinyan M, Oton C J, Dal Negro L, Pavesi L, Sapienza R, Colocci M and Wiersma D S 2005 *Phys. Rev.* B **71** 094204
[38] Passias V, Valappil N V, Shi Z, Deych L, Lisyanky A A and Menon V M 2009 *Opt. Express* **17** 6636–42
[39] Zhu S N, Zhu Y Y, Qin Y Q, Wang H F, Ge C Z and Ming N B 1997 *Phys. Rev. Lett.* **78** 2752–5
[40] Sheng Y, Koynov K, Dou J, Ma B, Li J and Zhang D 2008 *Appl. Phys. Lett.* **92** 201113
[41] Zhu S N, Zhu Y Y and Ming N B 1997 *Science* **278** 843
[42] Chen Y B, Zhang C, Zhu Y Y, Wang H T and Ming N B 2001 *Appl. Phys. Lett.* **78** 577
[43] Dal Negro L, Yi J H, Nguyen V, Yi Y, Michel J and Kimerling L C 2005 *Appl Phys. Lett.* **86** 261905
[44] Makarava L N, Nazarov M M, Ozheredov I A, Shkurinov A P, Smirnov A G and Zhukovsky S V 2007 *Phys. Rev.* E **75** 036609
[45] Moretti L, Rea I, De Stefano L and Rendina I 2007 *Appl. Phys. Lett.* **90** 191112
[46] Fradkin-Kashi K and Arie A 1999 *IEEE J. Quantum Electron* **35** 1649
[47] Fradkin-Kashi K, Arie A, Urenski P and Rosenman G 2002 *Phys. Rev. Lett.* **88** 023903
[48] Lifshitz R, Arie A and Bahabad A 2005 *Phys. Rev. Lett.* **95** 133901
[49] Levashov V E, Mednikov K N, Pirozhkov A S and Ragozin E N 2006 *Radiat. Phys. Chem.* **75** 1819
[50] Wang H *et al* 2006 *Thin Solid Films* **515** 2523
[51] Champeaux J Ph, Troussel Ph, Villier B, Vidal V, Khachroum T, Vidal B and Krumrey M 2007 *Nucl. Instrum. Methods Phys. Res.* A **581** 687
[52] Gu X, Chen X, Chen Y, Zeng X, Xia Y and Chan Y 2004 *Opt. Commun.* **237** 53
[53] Agrawal M, Sun Y, Forrest S R and Peumans P 2007 *Appl. Phys. Lett.* **90** 241112
[54] Capmany J, Pereda J A, Bermúdez V, Callejo D and Dié guez E 2001 *Appl. Phys. Lett.* **79** 1751
[55] Ganany-Padowicz A, Juwiler J, Gayer O, Bahabad A and Arie A 2009 *Appl. Phys. Lett.* **94** 091108
[56] Holland J 1975 *Adaptation in Natural and Artificial Systems* (Ann Arbor, MI: University of Michigan Press)
[57] Jiang L, Zheng G, Shi L, Yuan J and Li X 2008 *Opt. Commun.* **281** 4882
[58] Kohmoto M, Sutherland B and Iguchi K 1987 *Phys. Rev. Lett.* **58** 2436–9
[59] Schwartz C 1988 *Appl. Opt* **27** 1232–4

[60] Dulea M, Severin M and Riklund R 1990 *Phys. Rev.* B **42** 3680-3689
[61] Latgé A and Claro F 1992 *Opt. Commun.* **94** 389-96
[62] Gellermann W, Kohmoto M, Sutherland B and Taylor P C 1994 *Phys. Rev. Lett.* **72** 633–6
[63] Hattori T, Tsurumachi N, Kawato S and Nakatsuka H 1994 *Phys. Rev.* B **50** 4220–3
[64] Hu A, Tien C, Li X J, Wang Y H and Feng D 1986 *Phys. Lett.* A **119** 313–14
[65] Cohn J L, Lin J J, Lamelas F J, He H, Clarke R and Uher C 1988 *Phys. Rev.* B **38** 2326–32
[66] Zhu Y Y, Ming N B and Jiang W H 1989 *Phys. Rev.* B **40** 8536–40
[67] Birch J, Severin M, Wahlström U, Yamamoto Y, Radnoczi G, Riklund R, Sundgren J E and Wallenberg L R 1990 *Phys. Rev.* B **41** 10398–407
[68] Peng R W, Hu A, Jiang S S, Zhang C S and Feng D 1992 *Phys. Rev.* B **46** 7816–20
[69] Musikhin S F, Il'in V I, Rabizo O V, Bakueva L G and Yudintseva T V 1997 *Semiconductors* **31** 46–50
[70] Dal Negro L, Stolfi M, Yi Y, Michel J, Duan X, Kimerling L C, LeBlanc J and Haavisto J 2004 *Appl. Phys. Lett.* **84** 5186–8
[71] Agarwal A, Mora-Ramos M E and Alvarado-Tenorio B 2009 *Photon. Nanostruct.* **7** 63–8
[72] Vasconcelos M S, Albuquerque E L and Mariz A M 1998 *J. Phys.: Condens. Matter* **10** 5839
[73] Liu N H 1997 *Phys. Rev.* B **55** 3543–7
[74] Vasconcelos M S and Albuquerque E L 1999 *Phys. Rev.* B **59** 11128–31
[75] Huang X Q, Jiang S S, Peng R W and Hu A 2001 *Phys. Rev.* B **63** 245104
[76] Thiem S and Schreiber M 2010 *Eur. Phys. J.* B **76** 339
[77] Fu X, Liu Y, Zhou P and Sritrakool W 1997 *Phys. Rev.* B **55** 2882–9
[78] Yang X, Liu Y and Fu X 1999 *Phys. Rev.* B **59** 4545–8
[79] Gong Y, Liu X and Wang L 2010 *Opt. Lett.* **35** 285
[80] Golmohammadi S, Moravvej-Farshi M K, Rostami A and Zarifzar A 2008 *Appl. Opt.* **47** 6477–87
[81] Wang X, Grimm U and Schreiber M 2000 *Phys. Rev.* B **62** 14020–31
[82] Monsoriu J A, Depine R A, Martínez-Ricci M I, Silvestre E and Andrés P 2009 *Opt. Lett.* **34** 3172–4
[83] Barriuso A G, Monzón J J, Sánchez-Soto L L and Costa A F 2009 *J. Phys. A: Math. Theor.* **42** 192002
[84] Ryu C S, Kim I M, Oh G Y and Lee M H 1994 *Phys. Rev.* B **49** 14991–5
[85] Phillips P W and Wu H L 1991 *Science* **252** 1805
[86] Sánchez A, Maciá E and Domínguez-Adame F 1994 *Phys. Rev.* B **49** 147–57
[87] Li Y and Yang X 2010 *Opt. Commun.* **283** 2160
[88] Barriuso A G, Monzón J J, Sánchez-Soto L L and Felipe A 2005 *Opt. Express* **13** 3013
[89] Chilwell J and Hodgkinson 1984 *J. Opt. Soc. Am.* A **1** 742
[90] Riklund R and Severin M 1988 *J. Phys. C: Solid State Phys.* **21** 3217
[91] Gantmacher F R 1974 *The Theory of Matrices* vol 2 (New York: Chelsea)
[92] Maciá E 1998 *Appl. Phys. Lett.* **73** 3330–2
[93] Maciá E 2001 *Phys. Rev.* B **63** 205421
[94] Lei X Y, Li H, Ding F, Zhang W and Ming N B 1997 *Appl. Phys. Lett.* **71** 2889–91
[95] Ben Ali N and Kanzari M 2010 *J. Mod. Opt.* **57** 287–94
[96] Kumar Singh S, Thapa K B and Ojha S P 2007 *Optoelectron. Adv. Mater.* **1** 49
[97] Dong J W, Han P and Wang H Z 2003 *Chin. Phys. Lett.* **20** 1963
[98] Kanzari M and Rezig B 2001 *J. Opt. A: Pure Appl. Opt.* **3** S201
[99] Bouazzi Y and Kanzari M 2009 *Opt. Appl.* **34** 489–98
[100] Ben Ali N and Kanzari M 2011 *Phys. Status Solidi* a **208** 161–71
[101] Kolar M, Ali M K and Nori F 1991 *Phys. Rev.* B **43** 1034
[102] Escorcia-García J and Mora-Ramos M E 2009 *PIERS: Progress in Electromagnetics Research Symp. (Beijing)* p 1059
[103] Nava R, Tagüeña-Martínez J, del Río J A and Naumis G G 2009 *J. Phys.: Condens. Matter* **21** 155901
[104] Coelho I P, Vasconcelos M S and Bezerra C G 2010 *Phys. Lett.* A **374** 1574–8
[105] Peng R W, Huang X Q, Qiu F, Wang M, Hu A, Jiang S S and Mazzer M 2002 *Appl. Phys. Lett.* **80** 3063–5
[106] Peng R W, Liu Y M, Huang X Q, Qiu F, Wang M, Hu A, Jiang S S, Feng D, Ouyamg L Z and Zou J 2004 *Phys. Rev.* B **69** 165109
[107] Ben Abdelaziz K, Zaghdoudi J, Kanzari M and Rezig B 2005 *J. Opt. A: Pure Appl. Opt.* **7** 544
[108] Aziz Z, Bentata S, Djelti R and Sefir Y 2010 *Solid State Commun.* **150** 865–9
[109] Fink Y, Winn J N, Fan S, Chen C, Michel J, Joannopoulos J D and Thomas E L 1998 *Science* **282** 1679–82
[110] Qiu F, Peng R W, Huang X Q, Hu X F, Wang M, Hu A, Jiang S S and Feng D 2004 *Europhys. Lett.* **68** 658–63
[111] Nguyen D T, Norwood R A and Peyghambarian N 2010 *Opt. Commun.* **283** 4199
[112] Saldaña X I, López-Cruz E and Contreras-Solorio D A 2009 *J. Phys.: Condens. Matter* **21** 155403
[113] Zhukovsky S V and Galynsky V M 2006 *J. Opt. A: Pure Appl. Opt.* **8** 489–500
[114] Tuz V K 2009 *J. Opt. Soc. Am.* B **26** 627–32
[115] John S and Wang J 1990 *Phys. Rev .Lett.* **64** 2418–21
John S and Wang J 1991 *Phys. Rev.* B **43** 12772–89
[116] Cornelius C M and Dowling J P 1999 *Phys. Rev.* A **59** 4736–46
[117] de Medeiros F F, Albuquerque E L, Vasconcelos M S and Mauriz P W 2007 *J. Phys.: Condens. Matter* **19** 496212
[118] Smith D, Pendry J and Wiltshire M 2004 *Science* **305** 788
[119] Li J, Zhou L, Chan C T and Sheng P 2003 *Phys. Rev. Lett.* **90** 083901
[120] Jiang H, Chen H, Li H and Zhang Y 2003 *Appl. Phys. Lett.* **83** 5386-5388
[121] Zhang L, Fang K, Du G, Jiang H and Zhao J 2011 *Opt. Commun.* **284** 703–6
[122] Depine A, Martínez-Ricci M L, Monsoriu J A, Silvestre E and Andrés P 2007 *Phys. Lett.* A **364** 352
[123] Monsoriu J A, Depine R A, Martínez-Ricci M L and Silvestre E 2006 *Opt. Express* **14** 12958
[124] Li J, Zhao D and Liu Z 2004 *Phys. Lett.* A **332** 461-468
[125] Monsoriu J A, Depine R A and Silvestre E 2007 *J. Eur. Opt. Soc.* **2** 07002
[126] Vasconcelos M S, Mauriz P W, de Medeiros F F and Albuquerque E L 2007 *Phys. Rev.* B **76** 165117
[127] Hsueh W J, Chen C T and Chen C H 2008 *Phys. Rev.* A **78** 013836
[128] Deng X H, Liu J T, Huang J H, Zou L and Liu N H 2010 *J. Phys.: Condens. Matter* **22** 055403
[129] Maksimović M and Jakšić Z 2006 *J. Opt. A: Pure Appl. Opt.* **8** 355
[130] Bassiri S, Papas C H and Engheta N 1998 *J. Opt. Soc. Am.* A **15** 1450–9
[131] Tuz V R 2009 *J. Opt. Soc. Am.* B **26** 627–32
Tuz V R 2009 *J. Opt. A: Pure Appl. Opt.* **11** 125103
[132] Tuz V R and Batrakov O D 2010 *J. Mod. Opt.* **57** 2117–22
[133] Moretti L and Mocella V 2008 *Phil. Mag.* **88** 2275
[134] Boriskina S V, Gopinath A and Dal Negro L 2008 *Opt. Express* **16** 18813–26
[135] Moretti L and Mocella V 2007 *Opt. Express* **15** 15314–23

[136] Wang K, David S, Chelnokov A and Lourtioz J M 2003 *J. Mod. Opt.* **50** 2095
[137] Della Villa A, Enoch S, Tayeb G, Pierro V, Galdi V and Capolino F 2005 *Phys. Rev. Lett.* **94** 183903
[138] Dal Negro L, Feng N N and Gopinath A 2008 *J. Opt. A: Pure Appl. Opt.* **10** 064013
[139] Dallapiccola R, Gopinath A, Stellacci F and Dal Negro L 2008 *Opt. Express* **16** 5544
[140] Kroon L, Lennholm E and Riklund R 2002 *Phys. Rev.* B **66** 094204
[141] Zito G, Piccirillo B, Santamato E, Marino A, Tkachenko V and Abbate G 2008 *Opt. Express* **16** 5164
[142] Gopinath A, Boriskina S V, Feng N N, Reinhard B M and Dal Negro L 2008 *Nano Lett.* **8** 2423–31
[143] Matarazzo V, De Nicola S, Zito G, Morlile P, Rippa P, Abbate G, Zhou J and Petti L 2011 *J. Opt.* **13** 015602
[144] Bursill L A, Lin P J and Xudong F 1987 *Mod. Phys. Lett.* B **1** 195
[145] Xudong F, Bursill L A and Lin P J 1988 *Int. J. Mod. Phys.* B **2** 131
[146] Pollard M E and Parker G J 2009 *Opt. Lett.* **34** 2805–7
[147] Trevino J, Cao H and Dal Negro L 2011 *Nano Lett.* **11** 2008–16
[148] Penrose R 1974 *Bull. Inst. Math. Appl* **10** 266
[149] Mackay A L 1982 *Physica* A **114** 609
[150] Stampfli P 1986 *Helv. Phys. Acta* **159** 1260
[151] Wang K 2007 *Phys. Rev.* B **76** 085107
[152] Oxborrow N and Henley C L 1993 *Phys. Rev.* B **48** 6966–98
[153] Ricciardi A, Gallina I, Campopiano S, Castaldi G, Pisco M, Galdi V and Cusano A 2009 *Opt. Express* **17** 6335–46
[154] Zoorob M E, Charlton M D B, Parker G J, Vaumberg J J and Netti M C 2000 *Nature* **404** 740
[155] Wang K 2006 *Phys. Rev.* B **73** 235122
[156] Wang K 2010 *Phys. Rev.* B **82** 045119
[157] Ueda K, Dotera T and Gemma T 2007 *Phys. Rev.* B **75** 195122
[158] Rattier M, Benisty H, Schwoob E, Weisbuch C, Krauss T F, Smith C J M, Houdré R and Oesterle U 2003 *Appl. Phys. Lett.* **83** 1283–5
[159] Bayindir M, Cubukcu E, Bulu I and Ozbay E 2001 *Phys. Rev.* B **63** 161104(R)
[160] Zhou G and Gu M 2007 *Appl. Phys. Lett.* **90** 201111
[161] Notomi M et al 2004 *Phys. Rev. Lett.* **92** 123906
[162] Notomi M 2010 *Rep. Prog. Phys.* **73** 096501
[163] Lai Y, Zhang Z Q, Chan C H and Tsang L 2007 *Phys. Rev.* B **76** 165132
[164] Kim S K, Lee J H, Kim S H, Hwang I K and Lee Y H 2005 *Appl. Phys. Lett.* **86** 031101
[165] Wang Y, Liu J, Zhang B, Feng S and Li Z Y 2006 *Phys. Rev.* B **73** 155107
[166] Ricciardi A, Pisco M, Cutolo A, Cusano A, O'Faolin L, Krauss T F, Castaldi G and Galdi V 2011 *Phys. Rev.* B **84** 085135
[167] Rechtsman M C, Jeong H C, Chaikin P M, Torquato S and Steinhardt P J 2008 *Phys. Rev. Lett.* **101** 073902
[168] Florescu M, Torquato S and Steinhardt P J 2009 *Phys. Rev.* B **80** 155112
[169] Lee T D M, Parker G J, Zoorob M J, Cox S J and Charlton M D B 2005 *Nanotechnology* **16** 2703
[170] Matsui T, Agrawal A, Nahata A and Vardeny Z V 2007 *Nature* **446** 517
[171] Kennedy J, Eberhart R C and Shi Y 2001 *Swarm Intelligence* (San Mateo, CA: Morgan Kaufmann)
[172] Forestierre C, Donelli M, Walsh G F, Zeni E, Miano G and Dal Negro L 2010 *Opt. Lett.* **35** 133
[173] Zhai T R, Liu D H and Zhang X D 2010 *Front. Phys. China* **5** 266–76
[174] Ledermann A, Cademartiri L, Hermatschweiler M, Toninello C, Czin G A, Wiersma D S, Wegener M and von Freymann G 2006 *Nature Mater.* **5** 942
[175] Xavier J, Boguslawski M, Rose P, Joseph J and Denz C 2010 *Adv. Mater.* **22** 356
[176] Wang X, Xu J, Lee J C W, Pang Y K and Tam W Y 2006 *Appl. Phys. Lett.* **88** 051901
[177] Dyachenko P N, Miklayev Yu. V and Dmitrienko V E 2007 *JETP Lett.* **86** 240
[178] Man W, Megens M, Steinhardt P J and Chaikin P M 2005 *Nature* **436** 993–6
[179] Zijlstra E S and Janssen T 2000 *Europhys. Lett.* **52** 578
[180] Bin Ren X and Ren K 2011 *Solid State Commun.* **151** 42–6
[181] Xu J, Ma X, Wang X and Tam W Y 2007 *Opt. Express* **15** 4287
Tam W Y 2006 *Appl. Phys. Lett.* **89** 251111
[182] Kok M H, Lu W, Tam W Y and Wong G K L 2009 *Opt. Express* **17** 7275
[183] Hung J, Kok M H and Tam W Y 2009 *Appl. Phys. Lett.* **94** 014102
[184] Chew W 1996 *Waves and Fields in Inhomogeneous Media* (New York: IEEE Press)
[185] Burlak G, Koshevaya S and Sánchez-Mondragón J 2000 *Opt. Commun.* **180** 49
[186] Burlak G and Díaz-de-Anda A 2008 *Opt. Commun.* **281** 181
[187] Burlak G, Díaz-de-Anda A, Santaolaya Salgado R and Pérez Ortega J 2010 *Opt. Commun.* **283** 3569–77
[188] Hu Q, Zhao J Z, Peng R W, Gao F, Zhang R L and Wang M 2010 *Appl. Phys. Lett.* **96** 161101
[189] Bravo-Abad J, Fernández-Domínguez A I, García-Vidal F J and Martínez-Moreno L 2007 *Phys. Rev. Lett.* **99** 203905
[190] Li J, Liu S, Huang C, Li T, Wang Q and Zhu Y 2008 *J. Opt. A: Pure Appl. Opt.* **10** 075202
[191] Xu G, Pan T, Zabg T and Sun J 2008 *Phys. Lett.* A **372** 4958
[192] Grigoriev V V and Biancalana F 2010 *Photon. Nanostruct.* **8** 285–90
[193] Maciá E 1999 *Phys. Rev.* B **60** 10032–6
[194] Boriskina S V and Dal Negro L 2008 *Opt. Express* **16** 12511–22
[195] Zhang X 2007 *Phys. Rev.* B **75** 024209
[196] Thon S M, Irvine W T M, Kleckner D and Bouwmeester D 2010 *Phys. Rev. Lett.* **104** 243901
[197] Biancalana F 2008 *J. Appl. Phys.* **104** 093113
[198] Hiltunen M, Dal Negro L, Feng N N, Kimerling L C and Michel J 2007 *J. Ligthwave Technol.* **25** 1841–7
[199] Golmohammadi S and Rostami A 2010 *Fiber Integr. Opt.* **29** 209–24
[200] Di Gennaro E, Zannini C, Savo S, Andreone A, Masullo M R, Castaldi G, Gallina I and Galdi V 2009 *New J. Phys.* **11** 113022
Di Gennaro E, Savo S, Andreone A, Galdi V, Castaldi G, Pierro V and Masullo M R 2008 *Appl. Phys. Lett.* **93** 164102
[201] Axel F and Peyrière J 2011 *J. Phys. A: Math. Theor.* **44** 035005
[202] Griniasty M and Fishman S 1988 *Phys. Rev. Lett.* **60** 1334–8
[203] Nascimento E M, de Moura F A B F and Lyra M L 2009 *Photon. Nanostruct.* **7** 101–7
[204] Noh H, Yang J K, Boriskina S V, Rooks M J, Salomon G S, Dal Negro L and Cao H 2011 *Appl. Phys. Lett.* **98** 201109
[205] Roche S, Bicout D, Maciá E and Kats E 2003 *Phys. Rev. Lett.* **91** 228101
Roche S, Bicout D, Maciá E and Kats E 2004 *Phys. Rev. Lett.* **92** 109901
[206] Ramchurn S K and Makhan M 2010 *Comput. Mater. Sci.* **49** S99–103
[207] Chakraborty S, Hasko D G and Mears R J 2004 *Microelec. Eng.* **73/74** 392
Chakraborty S, Parker M C and Mears R J 2005 *Photon. Nanostruct.* **3** 139